Three case studies in spectroscopic mode identification of non-radially pulsating stars

Florian Maisonneuve

Department of Physics and Astronomy

University of Canterbury

A thesis submitted for the degree of

Doctor of Philosophy (PhD)

2011

Abstract

Gravity modes present in γ Doradus stars probe the deep stellar interiors and are thus of particular interest in asteroseismology. Mode identification will improve the knowledge of these stars considerably and allow an understanding of the issues with current pulsational models. The methods used in this thesis are also applied to a low degree pressure mode pulsator as a check for their validity.

A frequency analysis followed by a mode identification were done based on the high resolution spectroscopic data of one β Cephei star, PT Puppis, and two γ Doradus stars, HD 189631 and AC Lepus. Extensive spectroscopic data sets are obtained by three instruments: HARPS, FEROS and HERCULES. We obtained 161 spectra for PT Puppis, 422 spectra for HD 189631 and 248 spectra for AC Lepus.

The pulsational frequencies were determined by four methods: analysis of the variations in equivalent width, radial velocity, asymmetry of the line profile and by using the pixel-by-pixel frequency analysis. The mode identification was done using the recently developed Fourier Parameter Fit method.

Without achieving the same degree of confidence for all results, we report the identification of two pulsational modes in PT Puppis: ($\ell = 0$; $m = 0$) at $f_1 = 6.07$ d^{-1} and (2 ; 0) or (1 ; +1) at $f_2 = 5.99$ d^{-1}, four modes in HD 189631: (1 ; +1) at $f_1 = 1.67$ d^{-1}, (3 ; -2) at $f_2 = 1.42$ d^{-1}, (2 ; -2) at $f_3 = 0.07$ d^{-1} and (4 ; +1) at $f_4 = 1.82$ d^{-1} and two modes in AC Lepus: (2 ; -1) at $f_1 = 0.75$ d^{-1} and (3 ; -3) at $f_2 = 1.09$ d^{-1}. This study provides the first pulsational analysis based on spectroscopy of PT Puppis, HD 189631 and AC Lepus. We discuss the performance of current methods of analysis, outline the difficulties presented by γ Doradus stars, and compare our results with other published pulsational mode identifications.

Statement of originality

I hereby certify that I am the sole author of this thesis. The material in this thesis has not been previously submitted for another degree by anyone in any university. It contains no material published or written by another person except where acknowledged.

Supervision team

Main supervisor:

Dr. Karen Pollard
(karen.pollard@canterbury.ac.nz)

Secondary supervisors:

Prof. Peter Cottrell,

Prof. John Hearnshaw.

Acknowledgements

I would like to thank my family for their support, and in particular my partner Marie-Eve whose love and energy kept me going everyday.

I thank my fellow astronomers from rooms 801 and later room 805, especially Jeff for not complaining each time I bothered him by kicking in our common wall, and Emily for insightful conversations on asteroseismology and good cookies. I thank Duncan Wright who is the one who put me on track with many matlab scripts and a PhD thesis which was the starting point of this one.

I want to thank Prof. John Hearnshaw for convincing me to do my PhD in Christchurch, welcoming me and teaching me everything I needed to know about the telescope at MJUO. I thank the Department of Physics and Astronomy for giving me as many observing runs as I needed, and Orlon Petterson for solving all my computer issues with kindness.

I would like to thank my collaborators for giving me access to a large data set of excellent quality from Chile: Luciano Mantegazza, Ennio Poretti, Monica Rainer and especially Peter de Cat. I also thank Pam Kilmartin for covering many nights of observation at MJUO.

Finally, I thank my supervisors, Dr. Karen Pollard and Prof. Peter Cottrell, who never let a meeting go by without answering all questions in depth. Their help and their enthusiasm towards this research have been tremendous.

Contents

List of Figures

LIST OF FIGURES

List of Tables

Chapter 1

Introduction

1.1 Asteroseismology

For centuries stars with varying brightness have been recorded. However only within the last hundred years has it been understood that these variations are due to intrinsic pulsations of the stars themselves. This was the first step of asteroseismology. It studies the internal structure of stars through the analysis and interpretation of their oscillations. Stars are opaque, their interiors are not directly observable; probing these stellar interiors can only be done by observing the star's pulsations. These oscillations are dependent on the properties of the overall stellar structure. The frequency, amplitude and type of these pulsations give valuable information to asteroseismologists (Aerts et al., 2008). In theory, more information is obtained with each new pulsation observed for a star. In this way, the principles of asteroseismology are, to a certain extent, similar to those of earth seismologists.

Asteroseismology is a field of study which relies on the most advanced telescopes and instruments, modern techniques and methods of analysis of the data to identify the mode of pulsations, advanced mathematical descriptions of oscillations in a three dimensional body and accurate numerical modelling of stellar structures. It is a prominent example of interdisciplinary science. A successful modelling of a star's pulsation provide information on its internal temperature, pressure, chemical composition and mass distribution as a function of the radius. These properties then help to constrain the star's age, mass and radius (Briquet et al., 2007; Casas et al., 2006; Handler et al., 2003; Lenz et al., 2008; Mazumdar et al., 2006; Rodríguez et al., 2006b). A good ex-

ample of success in asteroseismology is its application to white dwarfs to deduce their core composition and crystalline structure (Kanaan et al., 2005). The ultimate goal of asteroseismology is to improve our understanding of stellar structure and evolution.

Many types of variable stars are known and each type can be localized in a specific region on a colour-magnitude diagram (or an HR diagram), as seen in Figure 1.1. Variable stars can have very different conditions of temperature, density, metallicity, and therefore the physics involved in one type of pulsation can differ greatly to another type. Different causes induce different types of pulsations. Two types of variable stars will be studied in this work: β Cephei and γ Doradus. Each is representative of larger groups of pulsating stars, respectively the pressure mode (p-mode, where the restoring force is pressure) and the gravity mode (g-mode, restoring force is gravity) pulsators.

The stellar pulsations can be either radial, where the entire surface of the star has the same radius which increases and decreases throughout the pulsation, or non-radial, where travelling waves propagate along the stellar surface. In most cases radial pulsation waves can only provide information on the mean density of the star, whereas non-radial pulsational (NRP) waves propagate only in certain regions of the stellar interior, so they can yield specific information about the layers in which they propagate (Aerts et al., 2007).

1.2 Non-radial pulsations

Non-radial pulsational modes are typically described by three wavenumbers: n, ℓ and m. The n represents the number of nodes, i.e. shells, between the centre and the surface of the star. It is not directly detectable with observations. The analysis of the pulsational modes will only give information about ℓ and m. The latter numbers correspond to the degree and azimuthal order of the spherical harmonic $Y_l^m(\theta, \phi)$ that represents the dependence of the mode on the angular variables θ and ϕ for a star assumed to be in spherically symmetric equilibrium. When observing pulsations on a two dimensional surface the lines which remain at rest while the other parts of the star are oscillating are called nodal lines. They are the two dimensional equivalent of the one dimensional nodes. As seen in Figure 1.2, the value of ℓ gives us the total number of nodal lines, whereas the value of m will tell how many of these lines pass through the poles of the rotational axis. Note that $\ell = 0$, $m = 0$, corresponds to a radial pulsation.

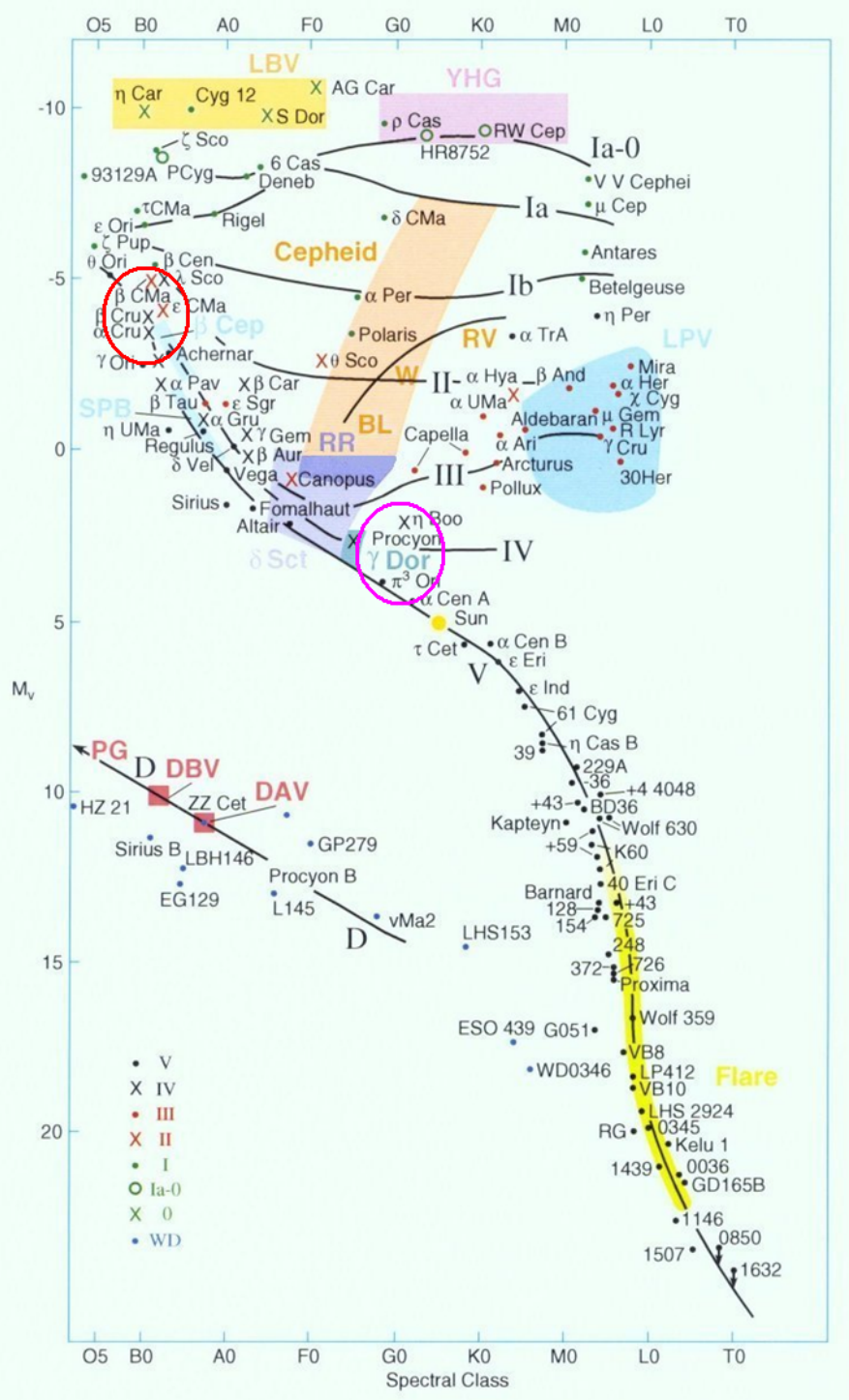

Figure 1.1: Colour-magnitude diagram of variable stars from Kaler (2006). The main sequence is represented by a solid black line from bottom right to top left, the γ Doradus region is circled by a thick pink line and the β Cephei region is circled by a thick red line.

In Figure 1.2, the dark purple sections are moving inward while the bright yellow ones are moving outward. They cause, respectively, a redshift and a blueshift in the observed stellar spectrum. Half an oscillation cycle later, the purple parts are moving outwards, whilst the yellow parts are moving inwards. The surface elements situated exactly on the nodal lines do not move during the oscillation cycle. In reality a star with NRPs will most likely have more than one pulsation, thus every surface element moves from the superposition of the pulsation modes in a very complicated manner.

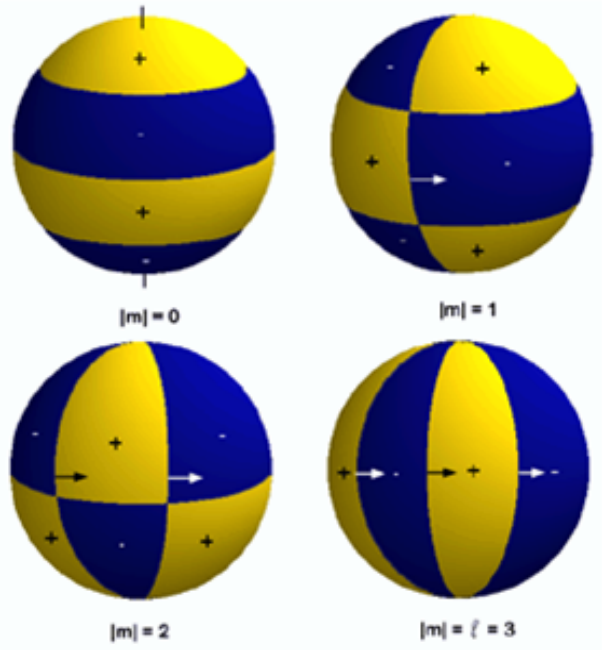

Figure 1.2: Non-radial pulsations. Representations of different non-radial pulsation modes, each with ℓ, the total number of nodal lines, equal to three. The four images differ by their value of m, the number of nodal lines through the vertical (rotation) axis, from $m = 0$ to $|m| = 3$ (Zima, 2006)

The modes with $m = 0$ are standing waves, called axisymmetric or zonal modes. Non-zonal modes are running waves. In this work we use the convention whereby negative m values denote modes moving opposite to the rotation (retrograde modes), while positive m values are associated with modes moving in the direction of rotation (prograde modes). The modes with $\ell = |m|$ are called sectoral, and those with $0 \neq |m| < \ell$ are tesseral.

A radial pulsation is generally directly observable by a change in the star's lumi-

nosity, which is due mostly to a photospheric temperature change. The size variation of the star only plays a small role in comparison. Photometry is therefore very effective in analyzing radial pulsations. In the case of NRPs the brightness variations are not as strong because of cancellation effects between parts of the star being out of phase in the pulsation cycle. These cancellation effects are greater as the degree ℓ of the pulsation is higher (Cunha et al., 2007). One exception is for $\ell = 1$ where the observable amplitude is greater than for the radial mode (Aerts et al., 2007). Thus photometry is still effective at detecting low degree NRPs.

The various movements of a star can be seen to some extent in spectroscopic observations. First, the relative velocity of the target star with respect to the sun causes a constant Doppler shifting of the whole spectrum. This does not affect the profile of individual spectral lines. The second effect is the rotation of the star. At all times, half of the star is moving towards the earth while the other half is moving away. The resulting Doppler shift is equally split between a red shift and a blue shift. This widens the spectral line proportionally to the stellar rotation. Since rotation is constant the line profile does not vary with time due to this effect. Finally, the movements of the surface elements caused by pulsations add to the general movement. Through a pulsation cycle, the velocity of surface elements varies with time and causes line profile variation. For a radial pulsation the line will uniformly be red shifted during half of the pulsation cycle, then blue shifted during the other half. For NRPs the surface elements are not all affected in the same way at the same time, so temporary "bumps" will appear and disappear on, or travel across, the line profile (Figure 1.3). This is observed by spectroscopy (Cunha et al., 2007). High precision, high resolution, spectroscopic observations are therefore critical in order to analyze NRPs. Four examples of line profile variations are shown on Figure 1.4. They have been produced synthetically by Wright (2008) using the FAMIAS software (Zima, 2008).

1.3 Types of non-radial pulsations and their mechanisms

There are several different types on non-radial pulsators. The Sun itself oscillates, but these oscillations are of extremely low amplitude, typically of the order of $2 \text{ X } 10^{-4}$ km.s^{-1}. These are called *stochastically excited* modes of pulsation, are not self-sustained, and

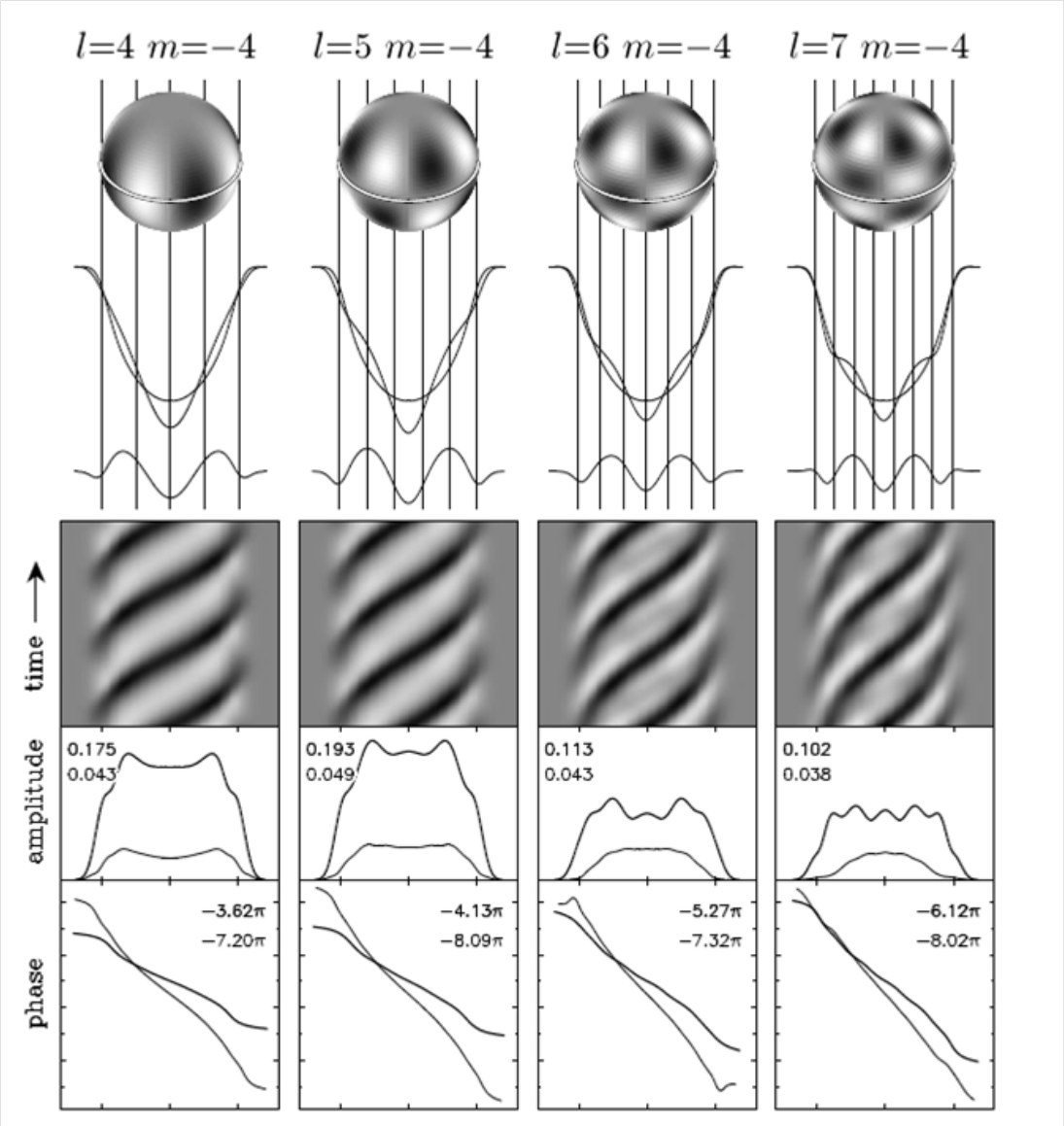

Figure 1.3: Examples of synthetic line profile variations caused by non-radial pulsations (Telting and Schrijvers, 1997a). Four different NRPs are represented. From top to bottom: Images of the star showing how surface elements are affected by the pulsation; superposed line profiles of pulsating and non-pulsating cases; difference of line profiles of pulsating and non-pulsating case; grey scale representation of residual spectra (mean subtracted) of 3 pulsation cycles; amplitude and phase diagrams of the pixel variation in the corresponding spectral line.

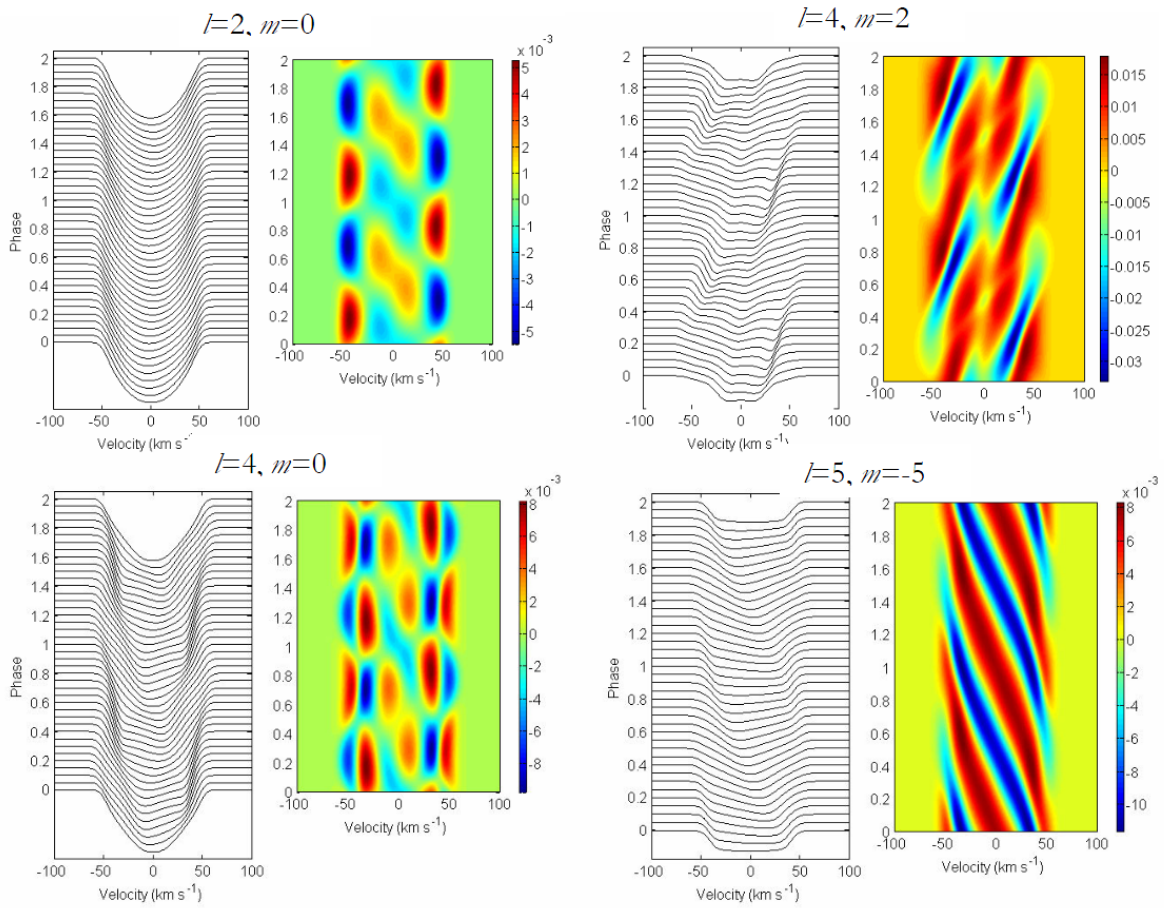

Figure 1.4: Examples of synthetic line profile variations caused by non-radial pulsations (Wright, 2008). In each case the line profiles are shown in a stacked plot and the difference from the mean is plotted as a 2-D colour-mapped surface. The modes are: $\ell = 2$, $m = 0$ (top left); $\ell = 4$, $m = 2$ (top right); $\ell = 4$, $m = 0$ (bottom left); $\ell = 5$, $m = -5$ (bottom right).

are expected in all stars having an outer convective layer. In the case of binary systems, oscillations can be forced by tidal effects. These are found with a large range of amplitudes.

In this thesis we concentrate on self-excited oscillations of large amplitudes, which can therefore be observed in distant stars. They belong to two distinct types of pulsations, either p-mode, where the restoring force is pressure, or g-mode, where the restoring force is gravity. The latter involves departure from spherical symmetry and hence are non-radial modes.

Pressure mode pulsations are observable because of a vertical displacement of the stellar surface, but they propagate through most of the star, especially low degree ℓ modes. In particular, radial p-modes extend essentially to the center of the star (Cunha et al., 2007). They have high frequencies when compared to g-modes and are found in β Cephei and δ Scuti stars. β Cephei stars have masses between 8 and 18 $M_{\odot}$ and effective temperatures around 25,000 K. Their observational characteristics have been reviewed by Stankov and Handler (2005). The δ Scuti stars are the less massive analogous of β Cephei along the main sequence, with masses ranging from 1.5 to 2.5 $M_{\odot}$. In the case of p-modes, both radial and non-radial modes can be found (Handler et al., 2004). A β Cephei star PT Puppis, is studied in this thesis.

The gravity modes are internal gravity waves originating from the deep regions of the star at low frequencies (Cunha et al., 2007). They have a larger horizontal component to their displacement than p-modes (Christensen-Dalsgaard, 2003), and are found in slowly pulsating B (SPB) stars and γ Doradus stars (Cunha et al., 2007). This thesis presents the analysis of two γ Doradus stars, HD 189631 and AC Lepus.

It should be noted that, in evolved objects, the basic description above is no longer valid as the two frequency domains can overlap and modes of a mixed nature can occur, i.e. g-mode characteristics in the deep layers and p-mode characteristics in the outer layers (Handler et al., 2004, 2006).

In the case of β Cephei stars, the p-mode pulsations are thought to be caused by the κ mechanism, caused by the opacity of the star's envelope, and described by Moskalik and Dziembowski (1992) and Dziembowski and Pamiatnykh (1993). This mechanism can be succinctly described like this: as energy radiates from the core it is stored into successive layers of the star, one after another. In the envelope, if a layer has specific conditions of temperature, luminosity and chemical composition it can trap the energy

longer than the other layers. Thermostatic equilibrium is then broken as the above layers are not receiving enough energy and thus start to contract. When the stored energy reaches a critical value, the "trapping" layer expands and releases it. The upper layers recover the energy and expand as well, the star reacquires its original size. The whole process can freely start over and millions of cycles can occur in this way. This can produce a very stable pulsation. The source of opacity responsible for β Cephei pulsations is thought to be the ionization of the iron group elements. The same process causes excitation of the high-order g-mode oscillations, with periods of a day or more, in the Slowly Pulsating B stars (Cunha et al., 2007).

In γ Doradus stars however, the mechanism is thought to be very different. Guzik et al. (2000) proposed a convective flux blocking mechanism. In γ Doradus stars, the convective zone is sufficiently deep for the convective timescale to be substantially longer than the pulsation period, thus convection cannot adjust rapidly enough during the pulsation cycle to transport the emerging luminosity. Hence the luminosity perturbations are blocked by convection at the base of the convective envelope, leading to heating in phase with compression (Warner et al., 2003). This was further investigated by Dupret et al. (2005), using the convection formulation of Gabriel (1996), which is a time dependent treatment of convection. This essentially confirmed that convective blocking dominates the driving of these oscillations. Dupret et al. (2005) then predicted an instability strip on the HR diagram from this theory matching the observations.

1.4 Mode identification of non-radial pulsations

Recent work in asteroseismology has provided the scientific community with powerful tools to determine the modes of oscillations of a variable star.

Initial works on photometric mode identification were done by Dziembowski (1977) and Balona and Stobie (1979). They pointed the fact that the amplitude and phase of the pulsations observed in the light curves depend on, among other things, the geometrical configuration of the nodal lines with respect to the observer, *i. e.* on the values of the wavenumbers ℓ and m, and of the inclination angle i. It was then realised by Watson (1988) that the dependence on m and i can be grouped under a single term independent of wavelength. Therefore multi-colour photometric time-series observations, which depend on wavelength, can uniquely identify the degree ℓ of a

pulsation mode. This is done using a method defined by Heynderickx et al. (1994) and later improved by Dupret et al. (2003) who included a non-adiabatic treatment of the oscillations in the atmosphere of their models. Dupret et al. (2003) illustrated the applicability of their method to β Cephei stars, SPB stars, δ Scuti stars and γ Doradus stars. In some cases multi-colour photometry can determine the ratio of the bolometric flux variation to the radial displacement, which is sensitive to stellar convection and can help in the selection of the convective model (Daszyńska-Daszkiewicz et al., 2003).

In a spectral line profile, the velocity field displacement due to the oscillations leads to line profile variations observable through high-resolution time-series spectroscopy. Various spectroscopic techniques have been developed and applied to γ Doradus and other types of variable stars. Most methods propose an identification of m but often lack the confidence of photometric techniques for the identification of l (Aerts et al., 2007). This is thus complementary to photometric data. The most common methods are

- a direct comparison of synthetic and observed line profiles (Balona, 2003; Mantegazza, 2000);
- the moment method (Aerts, 1996; Balona, 1986; Briquet and Aerts, 2003) applicable to low-degree modes ($\ell \leq 3$);
- Doppler imaging of the stellar surface (Berdyugina et al., 2003; Schrijvers et al., 1997; Telting and Schrijvers, 1997b);
- an analysis of the phase and amplitude across the line profile (Schrijvers and Telting, 1999; Zima, 2006)

In this thesis another technique, the Fourier Parameter Fit method (FPF) developed by Wolfgang Zima, is used. It relies on a direct fit to the observed Fourier parameters zero-point, amplitude and phase across the line profile, with theoretical values. It has produced excellent results on large spectroscopic data sets for some β Cephei and δ Scuti stars (Zima, 2006). It has the advantage over other mode identification methods to provide a statistical criterion to quantify the significance of the observed solutions. However difficulties have been encountered when applying the method to g-mode pulsating stars (Zima et al., 2007). The large horizontal velocities of g-mode pulsations make the identification of the azimuthal number m very difficult. The determination of

the inclination angle i is very uncertain and thus reliable frequency values in the stellar rotation frame of reference could not be derived. These frequencies are important for further theoretical modelling.

1.5 Pulsations in β Cephei stars

Photometric mode identification has been done on the β Cephei stars HD 29248 (ν Eridani) by De Ridder et al. (2004) and HD 214993 (12 Lacertae) by Handler et al. (2006), both based on extensive data sets. They show that both stars have low degree modes ($\ell < 4$), including at least one radial mode. Since photometry is biased to detect low degree ℓ pulsation modes only, a complementary work using high-resolution spectroscopic observations is necessary. Aerts et al. (2003) on HD 216916 (16 Lacertae), Briquet et al. (2009) on HD 180642, and Desmet et al. (2009) who also worked on HD 214993, all found, using spectroscopic observations, that their β Cephei targets pulsate in low degree ℓ modes, with at least one radial mode. This confirms the results obtained from photometry suggesting that all β Cephei stars pulsate in low degree modes, although the low number of stars analyzed does not allow for a generalization yet. It could be a selection effect as these targets were deliberately chosen for their high amplitudes and low projected rotational velocities. Thus if there are β Cephei stars without a radial mode, these targets had a higher probability to have radial modes excited to observable amplitudes.

Wright (2008) used the FPF method to analyze the pulsations of HD 163472, identifying one radial mode and one $\ell = 3$ or $\ell = 4$ mode, which confirms the result of Neiner et al. (2003). However this star is a particular case because Neiner et al. (2003) believe that the pulsation axis does not coincide with the rotational axis. This is incompatible with the assumptions made by all methods of mode identification.

1.6 Pulsations in γ Doradus stars

The γ Doradus and SPB stars are of particular interest in terms of asteroseismology, since they pulsate in high order, low-degree modes with co-rotating frequencies generally from 0.3 to 3 d^{-1} which probe the deep interiors of these stars (Kaye et al., 1999). Observationally these objects are challenging. The theoretical frequency spectra are

dense and the pulsation periods of around a day can give rise to severe aliasing problems. Beat periods up to years can occur. Hence long time sequences of observations are required in order to acquire enough data so that identification of the pulsation modes can be undertaken unambiguously. Large observing efforts are being undertaken by several research teams, including long-term multicolour photometric monitoring (Handler, 2009) or high resolution spectroscopic campaigns (De Cat et al., 2006) or both (Uytterhoeven et al., 2008b).

This thesis describes research that is part of a project to improve the spectroscopic mode identification of main-sequence non-radially pulsating stars such as γ Doradus stars and SPB stars and to examine the cause of mode identification difficulties in these stars (De Cat et al., 2009). We are undertaking an extensive observational campaign to look at a number of these variable stars (Maisonneuve et al., 2010). This includes obtaining high-resolution spectroscopic observations at a number of observatories worldwide as part of a coordinated campaign (Wright et al., 2009).

Two γ Doradus stars are being studied in this work and no SPBs. This is why the following theoretical background is only focusing on that type of variable stars. For recent reviews of γ Doradus stars we refer to Handler (2005) and Pollard (2009). It has been just over a decade since they have been classified as a class of pulsating stars (Kaye et al., 1999), although the class prototype, γ Doradus itself, has been identified as a variable star long ago by Cousins and Warren (1963). Further discoveries of stars sharing the same seismic characteristics led Mantegazza et al. (1994), Krisciunas (1994) and Hall (1995) to suggest that they constitute a new class of variable stars. Their variability has been interpreted in terms of multiperiodic high-order non-radial g-modes. The observational and calculated properties of the class members were summarized by Kaye et al. (1999): They belong to early F spectral types and are seen in all sorts of projected rotational velocities $v \sin i$. They have masses between 1.5 and 1.8 $M_{\odot}$, radii between 1.4 and 2.2 $R_{\odot}$, and effective temperatures ranging from 6900 K to 7400 K. Their metallicity is close to the sun's metallicity.

Although they are very challenging to study, it seems worthwile to do so because they have the potential to undergo at the same time g-modes solar-like pulsations because of their outer convection zone. Indeed, they are situated near the zone in the HR diagram where stochastically excited pulsations are predicted to happen (Christensen-Dalsgaard, 1982; Houdek et al., 1999). Moreover, from recent CoRoT (Baglin et al.,

2006) and Kepler observations (Gilliland et al., 2010), γ Doradus and δ Scuti (which have p-mode pulsations) pulsations can be found in the same star. This has recently been observed simultaneously by Uytterhoeven et al. (2008a), Hareter et al. (2010), and Grigahcène et al. (2010), in the so-called "hybrid stars". These stars can in theory provide more information than any other variable stars because both the outer layers, through the δ Scuti pulsations, and the inner layers, through the γ Doradus pulsations, can be probed (Handler et al., 2002). Uytterhoeven et al. (2008a) found that the star HD 49434 is one of these hybrid stars. They suggest that this would be the case for many γ Doradus stars and that it could be confirmed by spectroscopic observations.

In the recent years there has been significant progress in the understanding of γ Doradus stars. For instance, Miglio et al. (2008) have studied the properties of convective cores in slowly pulsating B (SPB) and γ Doradus stars by modelling high-order g-modes. On the other hand, the new Frequency Ratio Method (FRM) described in Moya et al. (2005) and Suárez et al. (2005) provides information on γ Doradus pulsating stars showing at least three pulsation frequencies identified with very high precision. The method provides an identification of the radial order n and degree ℓ of observed frequencies (under the assumption that all modes are the same degree) and an estimate of the integral of the buoyancy frequency (Bruntt-Väisälä) weighted over the stellar radius along the radiative zone (Rodríguez et al., 2006a,b).

Finally, the treatment of some of the theoretical aspects, such as stellar rotation and in particular the effects of the Coriolis and centrifugal forces, may become important in these stars. Rotation can, for instance, shift the κ-mechanism instability strip towards higher luminosities and effective temperatures, as it has been shown for SPB stars (Townsend, 2005). Also, as a star rotates faster, the pulsation is found with a greater amplitude towards the equator than near the poles (Townsend, 2003). Coupled with the effects of the inclination angle i, this can severely affect the way in which pulsations are seen from earth.

Previous attempts to identify the modes of pulsations in γ Doradus stars have been made. Some used only photometry (Breger et al., 1997; Rodríguez et al., 2006b; Zerbi et al., 1997, 1999), others used spectroscopy and worked with the moment method (Aerts and Kaye, 2001; Aerts and Krisciunas, 1996; Aerts et al., 2004a; Balona et al., 1996) or the intensity-period search (IPS) method based on Doppler imaging (Handler

et al., 2002; Hatzes, 1998; Jankov et al., 2006) or even both methods (Uytterhoeven et al., 2008a).

Wright (2008) performed the only two previous mode identifications on γ Doradus stars using the Fourier Parameter Fit (FPF) method, on QW Puppis (HD 55892) and HD 139095. QW Puppis is a relatively bright (V=4.5 mag) star which was observed from two sites, MJUO and SAAO (2008). Duncan Wright's conclusion is that four frequencies were found for QW Puppis which all appeared NRP-like: 2.1220 d^{-1}, 2.038 d^{-1}, 6.229 d^{-1} and 5.108 d^{-1}. From the FPF results the best fitting modes were $\ell = 5 \pm 3$, $m = 4 \pm 2$; $\ell = 6 \pm 2$, $m = 4 \pm 2$; $\ell = 4 \pm 2$, $m = 4 \pm 2$; $\ell > 0$, $m = 3 \pm 2$; for the four frequencies respectively (Wright, 2008).

The analysis of HD 139095 (V=7.9 mag) suffered from a low number of observations and a low signal (Wright, 2008). It was observed from a single site, MJUO. Four frequencies were identified: 2.353 d^{-1}, 9.560 d^{-1}, 8.638 d^{-1} and 10.14 d^{-1}. The attempts to determine the modes of pulsation lack the confidence of the analysis of QW Puppis. Only one result is given for the fourth frequency (10.14 d^{-1}) with $\ell = 7 \pm 1$; $m = 5 \pm 2$ (Pollard et al., 2008).

Table 1.1 lists the results of nine published articles about spectroscopic mode identification in γ Doradus stars. The amplitudes listed were obtained using different techniques of photometry and spectroscopy, they are therefore not comparable from one publication to another. They are only listed here to compare between frequencies identified in a single publication.

1.7 Thesis outline

This thesis describes the complete analysis of one β Cephei star, PT Puppis, and two γ Doradus stars, HD 189631 and AC Lepus, from the observations to the mode identification.

Chapter 2 describes how the data was acquired, reduced and treated. The star selection process is explained, the observing sites, telescopes and instruments are described. An observing log is available. Details about the data reduction process and continuum fitting are given.

Chapter 3 explains the methods used for the analysis of the data. The cross-correlation technique, which allows an important increase of the signal-to-noise ratio of

Table 1.1: Results of spectroscopic mode identification on γ Doradus stars from the literature. The amplitudes listed can only be compared between frequencies identified in the same publication.

Name #	Frequency	Amplitude	ℓ	$\lvert m\rvert$	Method	Ref.
γ Dor	1.32 d^{-1}	25 mmag	3	3	Moment method	Balona et al. (1996)
	1.36 d^{-1}	24 mmag	1	1		
	1.47 d^{-1}	7.4 mmag	1	1		
V398 Aur	0.79 d^{-1}	$A_1 = 4 \cdot A_2$	3	1	Moment method	Aerts (1996)
	0.35 d^{-1}		3	1	Moment method	
V2118 Oph	1.23 d^{-1}	18 mmag	2	2	Doppler imaging	Hatzes (1998)
V372 Peg	0.37 d^{-1}	2.3 km.s^{-1}	2	2	Moment method	Aerts and Kaye (2001)
CK Ind	1.13 d^{-1}	38 mmag	1	1	Doppler imaging	Handler et al. (2002)
	2.30 d^{-1}	28 mmag	1	1		
V2121 Cyg	1.61 d^{-1}	1.5 km.s^{-1}	5 ± 1	4 ± 1	Doppler imaging	Jankov
	1.27 d^{-1}	3.0 km.s^{-1}	4 ± 1	3 ± 1		et al. (2006)
HR 2514	1.27 d^{-1}	16 km.s^{-1}	6 ± 1		Moment method &	Uytterhoeven
	1.48 d^{-1}	12 km.s^{-1}	5 ± 1	1 ± 1	Doppler imaging	et al. (2008)
QW Pup	2.12 d^{-1}	2.3 km.s^{-1}	5 ± 3	4 ± 2	FPF method	Wright (2008)
	2.04 d^{-1}	1.0 km.s^{-1}	6 ± 2	4 ± 2		
	6.23 d^{-1}	0.6 km.s^{-1}	4 ± 2	4 ± 2		
	5.11 d^{-1}	0.5 km.s^{-1}	> 0	3 ± 2		
NX Lup	2.35 d^{-1}	1.4 km.s^{-1}	2	1	FPF method	Wright (2008)
HD 189631	1.67 d^{-1}	1.6 km.s^{-1}	1	1	FPF method	Maisonneuve
	1.42 d^{-1}	1.4 km.s^{-1}	3	2		et al. (2010)
	0.07 d^{-1}	1.2 km.s^{-1}	2	2		
	1.82 d^{-1}	1.0 km.s^{-1}	4	1		
AC Lep	0.75 d^{-1}	1.2 km.s^{-1}	2	1	FPF method	Maisonneuve
	1.09 d^{-1}	1.2 km.s^{-1}	3	3		et al. (2010)

the data is described. Also included are descriptions of methods to determine $v \sin i$ and the radial velocity of our targets. Four data sets are used for the frequency determination: the variations in equivalent width and radial velocity measurements (corresponding to the 0^{th} and 1^{st} moments), the pixel-by-pixel frequency analysis (Mantegazza, 2000) and finally the variations of the asymmetry of the line profile (related to the 2^{nd} moment). For the mode identification, the Fourier Parameter Fit (FPF) method of Zima (2006) is described and used.

The analysis of the 161 observations of the β Cephei star, PT Pup, obtained at Mount John University Observatory (MJUO) is outlined in Chapter 4. A careful comparison of cross-correlated and non cross-correlated data is done and the justification of cross-correlation is addressed in the case of β Cephei stars.

Chapter 5 presents the complete analysis of the 422 multi-site observations of the γ Doradus star HD 189631, and Chapter 6 presents the analysis of 248 observations of the γ Doradus star AC Lep, all obtained from MJUO. Chapters 5 and 6 have recently appeared in a slightly different form as Maisonneuve et al. (2010).

Chapter 7 is a discussion of the results on these three stars and comments on the mode identification method. It also compares the results with other similar analysis found in the literature. Chapter 8 concludes the thesis and gives some direction for future work in the challenging and exciting area of asteroseismology.

Chapter 2

Observations and data reduction

This chapter outlines the key elements of the strategy for the observational programme and the data reduction techniques used.

2.1 Star selection

The stars to be studied must meet a certain number of requirements. First, they must be bright enough in order to obtain good signal-to-noise spectra using the 1.0m telescope and HERCULES spectrograph. An 8th magnitude star is a reasonable faint limit considering the facilities available at the Mt John University Observatory (MJUO). This rules out variable stars such as ZZ Ceti and sdB stars which at ∼13th magnitude are too faint. Our targets should also be in the southern sky (declination $<$ -10^o) to allow extended (6 to 8 hours) observations from our site, situated at a latitude of -43.9^o S.

Line profile variations (LPVs) are hard to detect if the target has a very low rotational velocity, because then the spectral lines are not broad enough and the spectral line profile cannot be sampled well enough. LPVs are also hard to detect if the target has a very high rotational velocity. In this case the LPVs are smeared out in the very broad lines. We thus restrict ourselves to targets with projected rotational velocities (v sin i, where i is the inclination angle of the rotational axis of the star with respect to our line of sight) of 20 to 75 km.s^{-1}.

Other factors were looked at in star selection, such as the binarity of the targets. A single star allows for an easier and quicker analysis of its data, since the orbital

motion needs to be removed from the data of a binary star. Also the pulsation period can be a problem if it is too close to 24 hours, as different parts of the pulsational cycle need to be observed, and this can be problematic for pulsation periods close to 24 hours. Finally, as a requirement for this work, the exposure time for one observation cannot be longer than 5% of the pulsation cycle of the target star. If it is longer then the observation is smearing through a non-negligible part of the cycle and cannot be considered a "snapshot" of the pulsation. Since a signal-to-noise ratio over 100 is also required, if a target has pulsation cycles over a short period then it must be bright to allow for short exposures and still meet the signal-to-noise requirement. However the pulsational period is not always accurately known before we perform our observations.

Only two types of variable stars have been considered for this work: β Cephei and γ Doradus. About ten of each category fall in the above restrictions and only the brightest have been observed. One γ Doradus star, AC Lepus, exhibits clear LPV and has therefore been chosen as our main target. One β Cephei star, PT Pup, has been chosen as our main β Cephei target, due to its brightness and its clear LPV. Five other stars, four γ Doradus and one β Cephei, were observed sporadically as part of this programme (see Table 2.1).

2.2 Observation sites and telescopes

MJUO - 1.0m McLellan Many observations for this thesis have been done using the 1.0m McLellan telescope at Mount John University Observatory (MJUO) at Tekapo, New Zealand. The coordinates of MJUO are 43^o 59' S; 170^o 28' E, at an altitude of 1029 metres above sea level.

The optical design is a Dall-Kirkham Cassegrain and the telescope is on a traditional asymmetric single-pier equatorial mounting (Hearnshaw, 2006).

La Silla - 3.6m and 2.2m Two telescopes were used in La Silla, Chile: the 3.6m telescope equipped with the High Accuracy Radial velocity Planet Searcher (HARPS) and the 2.2m Max Planck Gesellschaft ESO telescope equipped with the Fibre-fed Extended Range Optical Spectrograph (FEROS). The site is at an altitude of 2400 metres above sea level. Its geographical location is: -29^o 15' S ; 70^o 44' W.

The ESO 3.6m telescope was commissioned in 1977 and completely upgraded in 1999. In 2004 a new secondary mirror cell was manufactured, improving considerably the image quality of the telescope, which is now better than 0.2 arcsec at zenith. The telescope has a horseshoe/fork mounting. Since April 2008 HARPS, using the f/8 Cassegrain focus, is the only instrument available on the 3.6m.

The 2.2m telescope at La Silla is on indefinite loan to the European Southern Observatory (ESO) from the Max Planck Gesellschaft. The telescope time is shared between the Max Planck Institue and ESO observers. The telescope, a fork mounted Ritchey-Chretien, was built by Zeiss and has been in operation at La Silla since 1984.

2.3 Spectroscopic instrumentation

HERCULES The High Efficiency and Resolution Canterbury University Large Echelle Spectrograph (HERCULES) is the spectrograph of MJUO, built by Hearnshaw et al. (2002) and in operation since April 2001. It allows stable, high-resolution, high-precision spectroscopy for reasonably bright ($V < 8$) stars (Pollard et al., 2007). HERCULES receives light from the f/13.5 Cassegrain focus of the 1.0m McLellan telescope via an optical fibre feed module.

The spectrograph is installed inside a vacuum tank in a thermally isolated environment. Radial velocities measurements have a precision of 10 m.s^{-1} (Hearnshaw et al., 2003). Observations were made using the 100 μm fibre which allows for a resolving power of 32,000. Other fibres giving different resolutions are also available.

HERCULES is equipped with a 600 Series Spectral Instruments CCD camera which incorporates a Grade 2 Fairchild Imaging CCD486 chip with 4096 X 4096 pixels. Each pixel is 15 μm^2 in size and has a maximum ADU readout of 65,535. The full spectral range for this spectrograph is from 3800 Å to 8800 Å spread over 105 échelle orders.

HARPS HARPS is the ESO spectrograph for the measurement of radial velocities with the highest accuracy currently available. It is fibre-fed at the Cassegrain focus of the 3.6m telescope in La Silla.

The instrument is built to obtain very high long term radial velocity accuracy, on the order of 1 m.s^{-1} (Mayor et al., 2003). To achieve this goal, HARPS is designed as an échelle spectrograph fed by a pair of fibres and optimised for mechanical stability.

Table 2.1: Observing log from MJUO. List of all observations done for this project from the MJUO site. After a period of selection of targets, efforts were concentrated on AC Lep and PT Pup.

Star name	Number of spectra	Time span	Variable type	V_{mag}	Coordinates (RA/DEC)
Primary	targets				epoch 2000.0
AC Lep	258	432 days	γ Doradus	6.21	06:00:18 / -12:54:00
PT Pup	161	430 days	β Cephei	5.69	07:36:41 / -19:42:08
HD 189631	43	382 days	γ Doradus	7.54	20:02:40 / -41:25:03
Additional	targets				
HD 14940	11	22 days	γ Doradus	6.67	02:24:09 / -16:15:15
HD 64365	16	102 days	β Cephei	6.03	07:51:40 / -42:53:17
HD 65526	13	423 days	γ Doradus	6.98	07:59:04 / -04:19:56
HD 135825	2	326 days	γ Doradus	7.30	15:17:32 / -10:30:02
HD 139095	37	326 days	γ Doradus	7.91	15:37:16 / -32:03:26

It is contained in a vacuum vessel to avoid spectral drift due to temperature and air pressure variations. The temperature of the spectrograph is kept stable to better than 0.01 K over a year.

One of the two fibres collects the star light, while the second is used to either record simultaneously a thorium-argon reference spectrum or the background sky. The two HARPS fibres (object + sky or thorium-argon) have an aperture on the sky of 1.0 arcsec; this produces a resolving power of 115,000 for the spectrograph. Both fibres are equipped with an image scrambler to provide a uniform spectrograph pupil illumination. The spectral range covered is 3780 Å to 6910 Å, distributed over the échelle orders 89 to 161. As the detector consists of a mosaic of 2 CCDs (altogether 4k X 4k, 15 μm^2 pixels), one spectral order (order 115, from 5300 Å to 5330 Å) is lost in the gap between the two chips.

FEROS FEROS is a bench-mounted fiber-linked échelle spectrograph. It is designed to have a high resolution ($R = 48,000$), high efficiency (20%), to be stable and versatile. It provides in a single spectrogram almost complete spectral coverage from 3500 Å to 9200 Å. The mechanical and thermal stability of FEROS allow for a precise wavelength calibration based on daytime calibrations and for most purposes additional calibrations during the night are not necessary, thus ensuring a high productivity in terms of the

Table 2.2: Observing log from La Silla, Chile. In this thesis, all the data from La Silla is for the γ Doradus star HD 189631, either with HARPS or FEROS.

Number of spectra	Time span	Instrument	Observer
273	7 days	HARPS	Peter De Cat
56	8 days	FEROS	Luciano Mantegazza
23	10 days	HARPS	Ennio Poretti
25	4 days	HARPS	Juan-Carlos Suárez

scientific data produced. Although not intended as a "radial velocity machine", precise radial velocity work is also possible, especially via the object-calibration mode. Accuracies of 25 m.s^{-1} or better are obtainable (Kaufer et al., 2000).

Like HARPS, FEROS is fed by two fibres providing simultaneous spectra of the target star and a calibration (either a celestial background, a wavelength calibration lamp or a flat-field lamp). The fibres are illuminated via 2.0 arcsec apertures on the sky separated by 2.9 arcmins. The spectral coverage is split over 39 échelle orders on the detector. This detector is an EEV 2k X 4k, 15 μm^2, pixel CCD.

2.4 List of observations

Several nights of observation were required to select the best targets for study and to accumulate enough data for their analysis. Observations at Mt John took place over two years. After an initial period of star selection, efforts were focused on the primary targets: AC Lep and PT Pup. The observers were Florian Maisonneuve, Pam Kilmartin and Karen Pollard. Table 2.1 is a summary of all observations done from the MJUO site.

In the case of HD 189631, data from Chile was obtained under the Normal Program 081.D-0610 (HARPS) and the Large Programs 178.D-0361 (FEROS) and 182.D-0356 (HARPS). Access to this data was made possible by an international collaboration with Peter De Cat at the Royal Observatory of Belgium (ROB) in Brussels, Belgium, and Ennio Poretti at the Osservatorio Astronomico di Brera in Merate, Italy. The observation list from La Silla, Chile, is presented in Table 2.2.

The julian date of each observation used for the analysis of PT Pup, AC Lep and HD 189631 are listed in Appendix A.

2.5 Observing procedure

Observing procedures were defined in order to obtain consistent data sets. To ensure that the instruments remained stable from night to night, a few spectra of a radial velocity standard star were taken per night. These standards were β Lep, β Aqr and α Tra which have spectral types of, respectively, G5II, G0I and K2II. Very small variability was observed in the radial velocity measurement from the spectra of these stars.

For wavelength calibration, a thorium-argon image was taken at least every hour or at each new position of the telescope. For the flat-field correction of the images and for the order tracing, several (five to ten) flat fields were taken each night for HARPS and FEROS, but not for HERCULES for which a standard, very high signal, flat field image was produced. This unique image was used for the reduction of most observations taken with HERCULES.

At MJUO, a fixed exposure time of ten minutes was chosen for AC Lep as this approximately corresponds to a signal-to-noise ratio of 120. The data is considered to be of good quality when the signal-to-noise ratio is over 100. HD 189631, being fainter, was observed with an exposure time of twenty minutes. For PT Pup, which is much brighter, exposures of five minutes were initially done. After the main frequency was identified, exposures of ten minutes were done to benefit from a great signal-to-noise ratio. Therefore a typical night at MJUO was designed as

- Position the telescope on β Lep (as a RV standard).
- Take one thorium-argon image.
- Take two observations of β Lep.
- Take one thorium-argon image.
- Position the telescope on the target star AC Lep.
- Take one thorium-argon image.
- Take two observations of AC Lep, ten minutes each.
- Position the telescope on the target star PT Pup.

- Take one thorium-argon image.
- Take two observations of PT Pup, ten minutes each.
- Repeat steps 5 to 10 until dusk or until the stars are no longer visible.
- Take one thorium-argon image.

Using HARPS, observations of HD 189631 were done with an exposure time varying from eight to twelve minutes depending on the seeing. All observations of HD 189631 using FEROS were done with an exposure time of ten minutes.

2.6 Data reduction

The data from MJUO was reduced using the computer program HRSP (Skuljan, 2004). It consists of a set of standard reduction procedures configured specifically for the HERCULES spectrograph. It begins by identifying the precise absolute position of the observed images by comparing a thorium-argon calibration image to a reference image. Then the bias, computed from an overscan strip on the image, is subtracted from all frames. Next it locates the order positions using a flat field image, extracts the flat field and normalizes it for calibrating the stellar image. Each spectral order is extracted from the image and is divided by the flat field. Details on how the flat field images were obtained for HERCULES are given in Appendix B. The thorium-argon images taken before and after the stellar spectrum are compared to calculate any shift in pixel position and the result is linearly interpolated to correspond with the time of the stellar image's observation. Wavelength calibration is computed from a two dimensional polynomial fit to a large number of calibration lines taken from the two thorium-argon images. Then the observational stellar data orders are extracted and rebinned to a linear wavelength scale. Finally the heliocentric correction is applied using the telescope coordinates and a flux-weighted mid-exposure time. It determines the radial velocity shift due to earth's movement around the sun and converts it in a wavelength shift which is applied to the data.

For both HARPS and FEROS the data reduction was performed using two semi-automated pipelines written by Monica Rainer (Rainer, 2003). Observations taken in the framework of the ESO LP 178.D-0361 and LP 182.D-035 were aimed to extend the

knowledge on the spectroscopic behaviour of γ Doradus stars, targets of the asteroseismic programme of the photometric CoRoT mission.

2.7 Further treatment of the data

Removing cosmic rays In this work, to achieve a good signal to noise ratio, the exposure time of observations can be as long as ten minutes (sometimes even more). During this time, the CCD chip is being bombarded by many cosmic rays. The image is therefore polluted with random spikes of photon counts. Many pixels of the CCD chip do not belong to spectral orders, thus cosmic rays hitting these regions are ignored. But they need to be removed from the observations when they hit a spectral order.

Although the data reduction takes this into account and removes the effect of cosmic rays on the data, a few cosmic rays remain undetected by these routines, either because they were too weak or located at an unfortunate position on the chip. For each data set an additional cosmic ray filter was applied in the form of a median filter. The median filter routine compares each pixel's intensity with the mean of a range of pixels on each of its sides. If this pixel intensity is above the mean by a multiple of standard deviations of that set of pixel intensities, it is replaced by the median of the set. This technique depends on two parameters:

- N, the number of pixels taken into account on each side of the considered pixel. The default value of N is 20; and
- s, the number of standard deviations above the mean for which a pixel intensity is considered to be a cosmic ray. The default value of s is 5.

Because the technique of median filtering can strongly alter the data, extreme care was taken when choosing the parameters, N and s, of this median filter. A careful visual comparison of the data was done before and after this process. The parameters were optimized to preserve the true variations of the data and thus differ for each data set.

Continuum fitting After reduction, the data is not ready yet for analysis. One important step is to perform a continuum fitting or continuum normalization of the

spectrum. It is the process of fitting the data in each échelle order so that the continuum level in the stellar spectrum is always equal to unity.

Any process in which the data is altered manually can introduce uncertain results. It is easy for the observer to makes changes to the data to reflect their expectations. For our three target stars, where many observations are available, an inspection of the mean spectrum after continuum fitting can be indicative of whether the continuum was fitted well. The easiest way of removing any possibility of forcing the data to match preconceptions is to remove the observer's input and automate the continuum fitting routine.

For HARPS and FEROS data, the continuum fitting was performed by Monica Rainer using an automated routine. For HERCULES data the automated routine was developed and tested by Wright (2008). It deals with each spectral order individually, using a succession of 5^{th} order least-squares polynomial fits. Between each successive fit, outliers in the residuals are removed. In specific cases when the continuum fitting of some orders is not satisfactory, a manual fitting must be performed.

Manual continuum fitting requires the observer to define, for a minimum of six points, where the continuum level is for each order being fitted. Using cubic spline interpolation, a line is fitted through the chosen points and this is taken as the continuum fit. The spectral order is then divided by the fitted line. About thirty points were chosen on average for this manual fit.

An example of continuum fitting is shown in Figure 2.1. It shows in green the raw data prior to a division by the flat field, which is an intermediate step in the data reduction process. After reduction is complete one can see, from the blue curve, that continuum fitting is required. The continuum-fitted data, in red, has its continuum equal to unity. Note that, as expected, the noise level is higher on the edges of the échelle order where there is less signal.

Combining orders to form the complete spectrum Assuming that the continuum fitting was successful on each order separately, the next task is to combine these orders to form a complete spectrum. A single wavelength axis is defined, for instance from 4000 Å to 8500 Å with a step size of 0.01 Å in the case of HERCULES data. Each échelle order is rebinned to fit this unique axis.

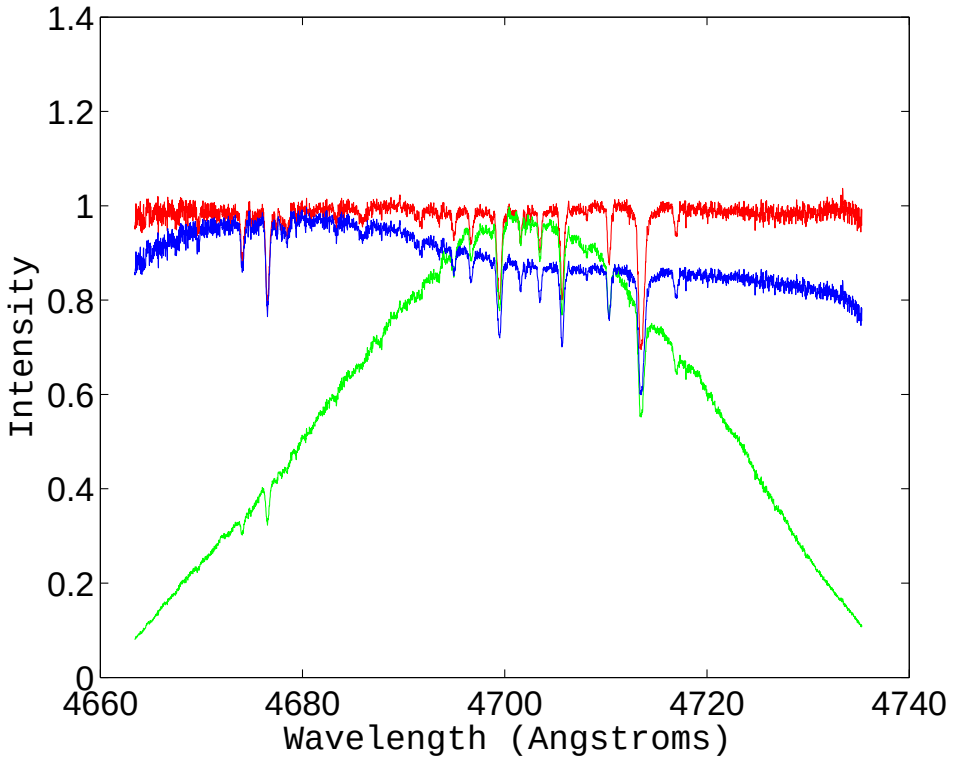

Figure 2.1: Continuum fitting. Example of a HERCULES observation of PT Pup, order number 121, continuum fitted by an automated routine. Data prior to a division by the flat field is shown in green. The data after flat-fielding but before continuum fitting is in blue while the continuum fitted data is in red.

The central part of a given spectral order covers a wavelength range which can only be found in this order, whereas the data found in the wings is also present in the adjacent order (either the previous or the next one). Thus the central parts are simply copied over to the complete spectrum array, leaving gaps between each order. To fill the gaps, data which is found in both adjacent orders is combined by a weighted function determined by the number of photon counts in the flat-field. Priority is therefore given to the order which has the best signal-to-noise ratio at a specific wavelength. For instance, the intensity in a range between λ_{min} and λ_{max}, which is found both in orders n and $n+1$, is defined by

$$Intensity(\lambda) = Int_n(\lambda) \cdot Wnorm_n(\lambda) + Int_{n+1}(\lambda) \cdot Wnorm_{n+1}(\lambda) \tag{2.1}$$

where $Int_n(\lambda)$ is the intensity of the order n at wavelength λ and $Wnorm_n$ and $Wnorm_{n+1}$ are the normalized weights corresponding to orders n and $n+1$ respectively. They are defined as

$$Wnorm_n(\lambda) = \frac{W_n(\lambda)}{max(W_n)} \tag{2.2}$$

$$Wnorm_{n+1}(\lambda) = \frac{W_{n+1}(\lambda)}{max(W_{n+1})} \tag{2.3}$$

where

$$W_n(\lambda) = \frac{FFint_n(\lambda)}{FFint_n(\lambda) + FFint_{n+1}(\lambda)} - \frac{FFint_n(\lambda_{max})}{FFint_n(\lambda_{max}) + FFint_{n+1}(\lambda_{max})} \tag{2.4}$$

$$W_{n+1}(\lambda) = \frac{FFint_{n+1}(\lambda)}{FFint_n(\lambda) + FFint_{n+1}(\lambda)} - \frac{FFint_{n+1}(\lambda_{min})}{FFint_n(\lambda_{min}) + FFint_{n+1}(\lambda_{min})} \tag{2.5}$$

where $FFint_n(\lambda)$ is the intensity of the flat field of order n at wavelength λ.

The previous set of equations ensures that the following conditions are satisfied

$$W_n(\lambda_{min}) = 1 \qquad\qquad W_{n+1}(\lambda_{min}) = 0$$

$$W_n(\lambda_{max}) = 0 \qquad\qquad W_{n+1}(\lambda_{max}) = 1$$

and

$$W_n(\lambda) + W_{n+1}(\lambda) = 1 \qquad \forall\ \lambda$$

In this way the transition between two orders is as smooth as possible in the resulting complete spectrum of the star. An inevitable increase in noise is found at regular intervals corresponding to these transition regions between two orders, but these noise peaks are kept to a minimum. The continuum fit is not affected by the combining of échelle orders.

Combining data from different instruments Because the analysis of our data is based on variations of a line profile (i.e. deviations from an average), the instrumental profile inherent in the data can be ignored if the data is obtained from a single instrument. This is the case for PT Pup and AC Lep. However, for HD 189631, data from different instruments is combined. In this case it is necessary that the three average spectra calculated independently for each instrument from all observations are equivalent.

Out of 422 observations of HD 189631, 321 were obtained from HARPS, 56 from FEROS and 45 from HERCULES. Assuming that enough observations were obtained from each site, we consider that their averages must be equal and we rescaled the average of observations from FEROS and HERCULES according to the average of the observations from HARPS. This removes the instrumental profile of FEROS and HERCULES and replaces it by the instrumental profile of HARPS.

The final step in the preparation of the HD 189631 data is to remove spectral regions which are not covered by every spectrograph. We already know that the three instruments cover different spectral ranges and an order is missing from the HARPS data. Thus small parts of the data are lost in every set to define a single spectral coverage common to all data sets. Only then can all observations of HD 189631 be considered to form a single data set.

Chapter 3

Methods of analysis

In this chapter the chosen methods of analysis are explained. These include cross correlation, which is a way of increasing line profiles' signal-to-noise ratios, and the methods of analysis of the spectral line profile in order to derive their projected rotational velocity, radial velocity, frequency of pulsations and the identification of the modes of these pulsations.

3.1 Cross correlation

Successful spectroscopic mode identification relies on high signal-to-noise ratio data which is well sampled in time. The analysis requires only a single line profile, but this profile must be of high signal-to-noise and not blended with other stellar spectral lines. In a stellar spectrum covering a large wavelength range, such as the spectra obtained for this thesis, it is possible to combine data from different spectral lines to get a single line profile with a much higher signal-to-noise ratio. This assumes that all spectral lines are affected in the same manner by the pulsations of the star. This is done using a cross-correlation technique explained in detail by Wright (2008) which we summarize here. A synthetic spectrum is produced with the characteristics of the target star (effective temperature, log g, metallicity), shifted by the radial velocity measured on the mean spectrum of all observations. It can then be fitted to this mean spectrum, allowing the depth of each individual line to vary. The rest wavelength and equivalent width of each line in this modified synthetic spectrum are used to produce a delta function at the position of the rest wavelength and with a height proportional to the equivalent

width. This template of delta functions is then cross correlated with every observation, producing a single line profile representative of the star at time of the observation. This greatly increases the signal-to-noise ratio of the spectral line profile, as seen on Figure 3.1.

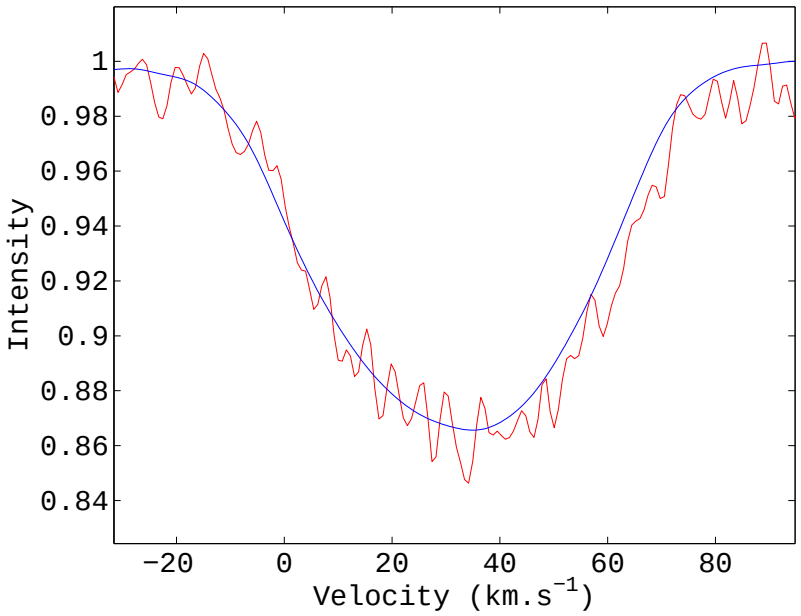

Figure 3.1: Example of cross-correlation. The curves correspond to a single observation of AC Lep. The red curve is the spectral line Ca I (6122 Å) while the cross-correlated profile is in blue. The signal-to-noise ratio is greatly improved by a cross-correlation.

Independent cross-correlations were performed on the HD 189631 data using either all strong lines in the spectrum, or lines from specific species: Fe I, Fe II, Na I and Ca I. For each of these five data sets, the mean profile and the standard deviation of each pixel across the profile were computed. They are displayed on Figures 3.2 and 3.3. It can be seen that the line profile variations observed in each species are very similar to the line profile variations observed on the global cross-correlation. They are observed in the same parts of the lines and with similar amplitudes: three bumps, one in each wing and a central one. The lines represent a large range of species of different ionization and excitation potentials which are forming at different depths within the star's atmosphere.

Figure 3.4 shows the radial velocity variations in several individual spectral lines

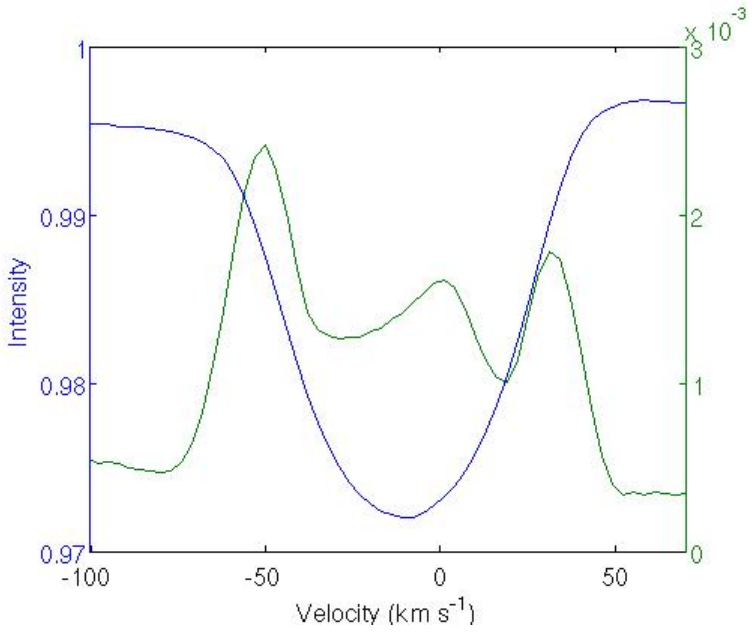

Figure 3.2: Cross-correlated profile of HD 189631. The mean and the standard deviation of the cross-correlated line profiles of all observations are shown. The cross-correlation was performed using all strong lines in the spectrum.

for AC Lep. It can be seen that the noise level can be high if a single line is used for the analysis. In most cases the pulsations affect all lines in the same way, confirming that the lines vary in phase. The exceptions are often due to a wrong determination of the radial velocity due to a poor signal-to-noise observation.

These observations show that for our targets the pulsations affect all spectral lines in the same way. This is the condition which allows us to use this technique. Works on several γ Doradus stars could confirm whether this condition is fulfilled for every member of the class.

3.2 Line profile variation (LPV)

The three target stars were investigated for LPV by examining the variations in their spectral line profile, either a single strong and isolated line for PT Pup, or a cross-correlated profile for HD 189631 and AC Lep. The following statistical tool was used to determine the presence or not of LPVs: For a data set the standard deviation of each pixel in the line profile is computed. Then the mean of these standard deviations

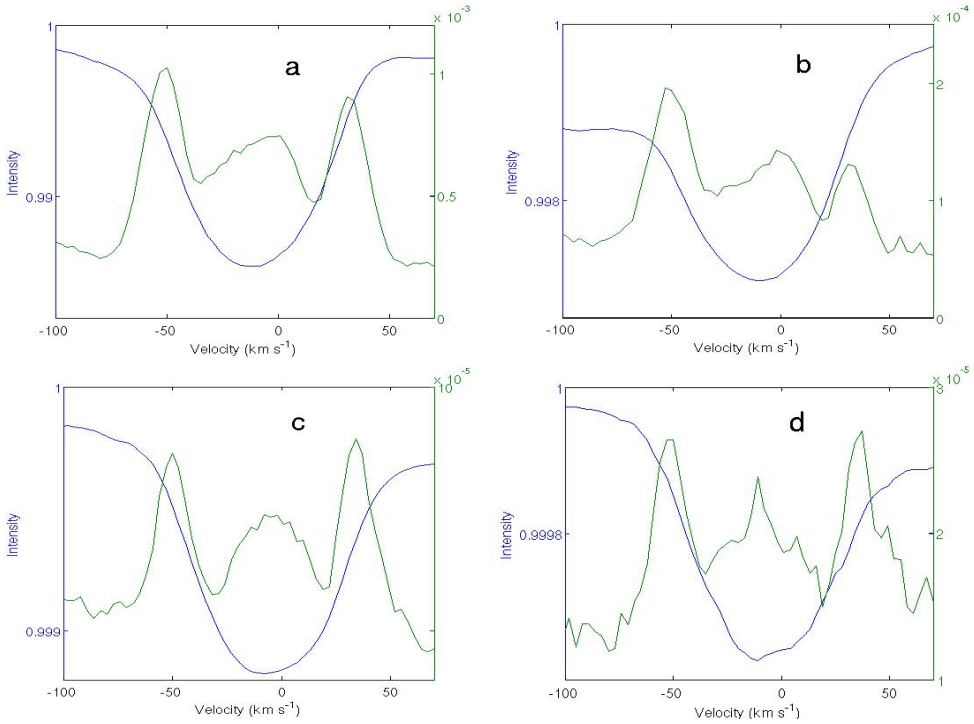

Figure 3.3: Comparing the pulsational effects on different chemical species for HD 189631. Mean cross-correlated line profiles and their standard deviations for Fe I (a), Fe II (b), Ca I (c), Na I (d).

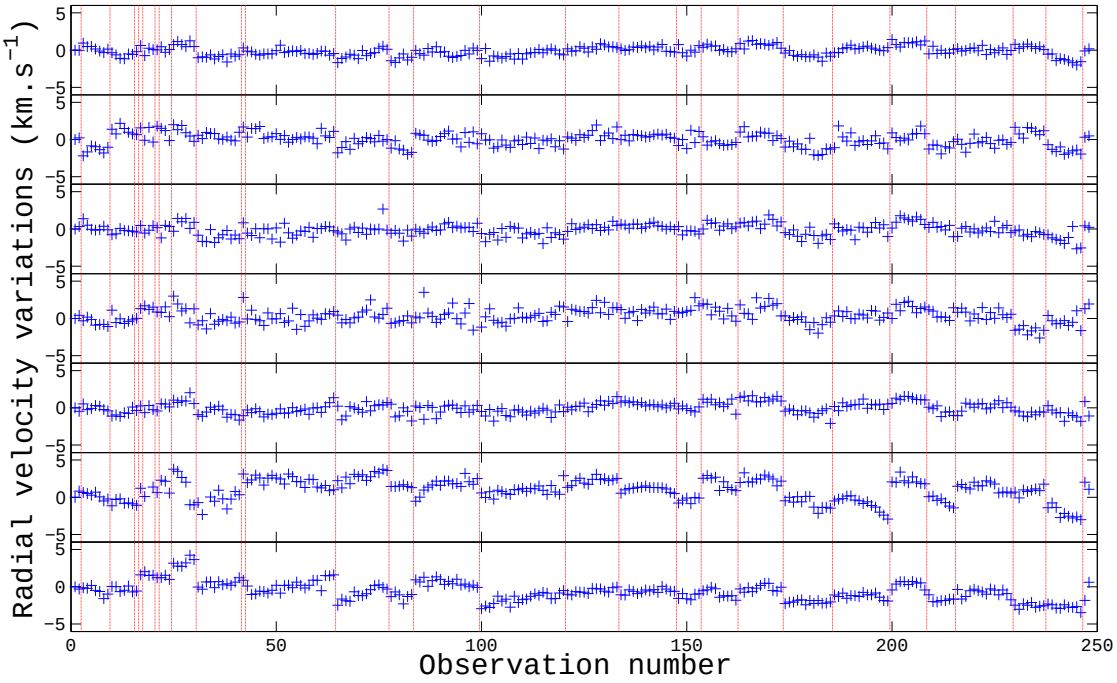

Figure 3.4: Comparing the pulsational effects on different chemical species for AC Lep. Radial velocity variations in km.s^{-1} are plotted for seven different spectral lines, from top to bottom: Ca I (6122 Å), Fe I (5302 Å), Fe I (5367 Å), Ca I (5582 Å), Ca I (5857 Å), Si II (6347 Å), Fe II (6456 Å). Vertical lines delimit the nights of observation. Variations are plotted versus observation number.

is taken across the profile. This is equal to 0.0285 for PT Pup, 0.0098 for HD 189631 and 0.0076 for AC Lep. By further examining the mean standard deviation across the profile for small subsets of the observations of HD 189631 and AC Lep, a conservative threshold of 0.0050 was chosen as the lower limit for the presence of LPVs.

For each of them, five to ten observations are enough to show without a doubt that there is LPV. Figures of LPV for our three targets are in their associated chapters. We also observed LPV in our alternative targets HD 64365 and HD 65526.

3.3 v sin i

The value of v sin i for each target was determined by two methods: The Fourier first minima method and the rotationally-broadened Gaussian method, both described by Gray (2005) and used by Wright (2008). In the following subsections, these methods, and their applications, are described in more detail.

3.3.1 Fourier minima method

This method compares the Fourier transform of a line profile with the Fourier transform of an artificial Gaussian broadened by the rotational velocity. Wright (2008) showed that the measurement of v sin i by this method is independent of the chosen full width at half maximum (FWHM) for the Gaussian profile. However the value of the v sin i chosen to broaden the synthetic Gaussian profile has a small effect if its value is extremely low or high. It is set to be equal to 20 km.s^{-1}, which Wright (2008) shows to be leading to good results.

Figure 3.5 shows the Fourier transforms of a synthetically broadened Gaussian and of a real cross-correlated spectral line profile, in this case HD 189631. A broader spectral line will lower the frequency of the first minima on the abscissa, which is the only measurement necessary to make. To determine the value of v sin i, the ratio of the positions of the first minimum on the abscissa between the observed and the theoretical profile is examined. By multiplying this ratio by the v sin i of the theoretical profile, the v sin i of the observed line is obtained. This can be written as

$$v \sin i = \frac{\text{Minimum}_{\text{theo}}}{\text{Minimum}_{\text{obs}}} \cdot v \sin i_{\text{theo}} \tag{3.1}$$

where $\text{Minimum}_{\text{theo}}$ and $\text{Minimum}_{\text{obs}}$ are the positions of the first minima along the abscissa for the theoretical and the observed lines respectively. In the example of Figure 3.5, v sin i for HD 189631 is measured to be 43.5 km.s^{-1}.

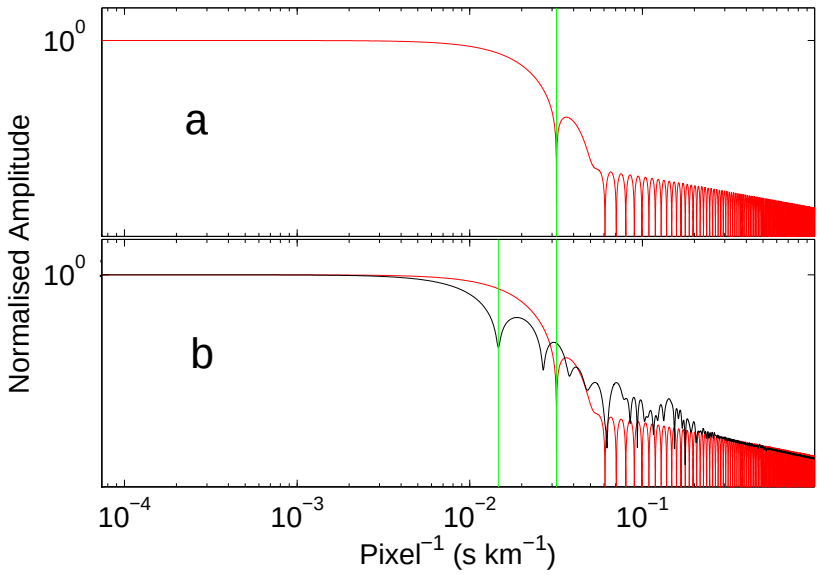

Figure 3.5: Measurement of v sin i using the Fourier minima method. (a) A log-log plot of the Fourier transform of a synthetic line with v sin $i = 20$ km.s^{-1}. The position of the first minimum is indicated by a green vertical line. (b) The Fourier transform of a real cross-correlated profile, in black, is superimposed and the position of its first minimum is indicated.

Since the noise in the Fourier domain is limited to higher frequencies, broad profiles, and hence high values of v sin i, can be more easily measured because the noise is not present in the area of measurement. For this reason, this method is effective only for lines with v sin $i \geq 15$ km.s^{-1}.

3.3.2 Broadened Gaussian method

This method is a direct least-squares fitting of the convolution of a Gaussian profile with the broadening function of Gray (2005). This is implemented as

$$G = \frac{2(1-\epsilon)\sqrt{1-(\lambda \cdot c/(\lambda_0 \cdot v \sin i))^2} + \frac{\Pi \cdot \epsilon}{2}[1-(\lambda \cdot c/(\lambda_0 \cdot v \sin i))^2]}{\frac{\Pi \cdot \lambda \cdot v}{c} \sin i (1-\frac{\epsilon}{3})} \tag{3.2}$$

and the full profile is represented by

$$e^{(\frac{\lambda}{w})^2} * G \quad \text{for } G > 0. \tag{3.3}$$

In these equations G is the broadening curve, ϵ is the limb-darkening coefficient, λ is the linear vector of wavelengths that describe the line profile, c is the speed of light, λ_0 is the rest wavelength of the line, $v \sin i$ is the projected rotational velocity, w is the width parameter of the Gaussian and * represents convolution. A graphical example of this method is shown on Figure 3.6.

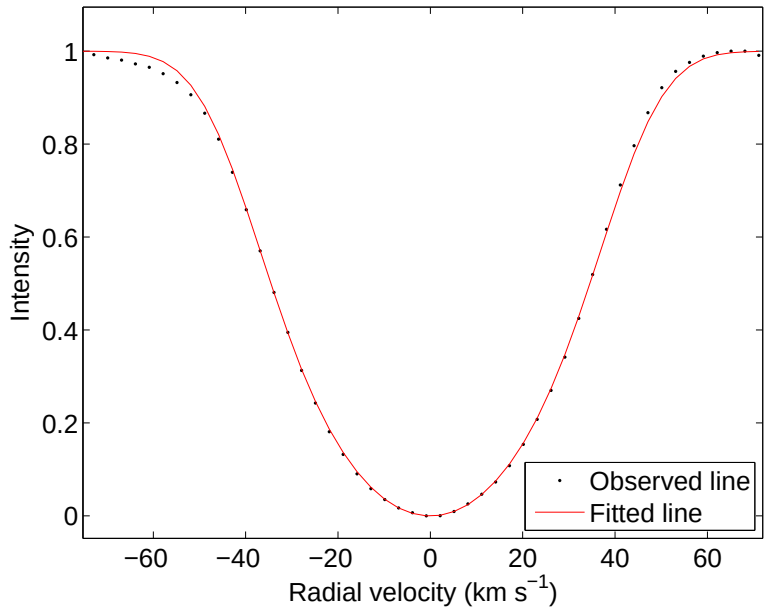

Figure 3.6: $v \sin i$ determination using the broadened Gaussian method. In this example the broadened Gaussian fits very well the data of HD 189631.

The resulting broadened line profile is fixed to the same depth as the input line profile to be fitted. The broadening function requires a wavelength as input. For an

isolated spectral line the rest wavelength is used. For a cross-correlated profile we take the centre of the region used to create it. The free parameters fitted are the width of the Gaussian and the $v \sin i$ of the broadening function. In this way the Gaussian can represent the spectrograph's response function and the broadening of the star's line profile by various broadening mechanisms. If the instrumental profile has been removed it will only represent the line broadening mechanisms. Because there is no optimization of any vertical shift the continuum fitting is critical. For this reason a continuum fitting to our cross-correlated profiles was sometimes performed to correct small imperfections before using this method. Only the core of the line profile is used for the fit because the true line broadening is better represented by a Voigt profile than a Gaussian. They differ in their shape mostly in the line wings. The core of a given line profile is defined here by the deeper part of the profile up to 80 % of its depth. This method is appropriate for almost every possible value of $v \sin i$. It only fails in the case of hot stars with extremely low rotational velocity where the star's lines (mostly H, He) are broadened by other mechanisms than rotation.

3.4 Radial velocity

We used the bisector method to determine the radial velocity at different depths in the cross-correlated spectral line. Gray (1988) describes this method as the best way to describe the asymmetry. The line bisector consists of the midpoints of horizontal line segments extending across the line profile.

The average line profile for a given star can be asymmetric; thus looking at different depths in the spectral line will yield different results. We used the value measured at 50% of the line depth to define the radial velocity. Figure 3.7 is an example of radial velocity determination using the bisector method. The line bisector values at 50% and 90% were used to compute a slope which we denote as the line profile asymmetry parameter (LPAP), representing the asymmetry in the line. In the next section, variations in the LPAP data set are used to investigate pulsation frequencies.

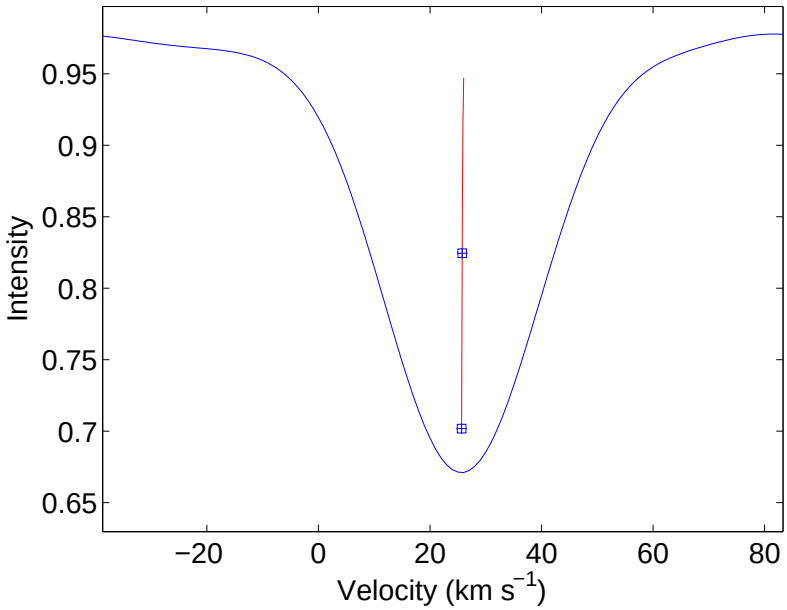

Figure 3.7: Radial velocity determination by the bisector method. The vertical line is the bisector of the spectral line of Si III (4552 Å) for PT Pup. The symbols are situated at 50 % and 90 % of the line depth.

3.5 Frequency analysis

The FAMIAS software (Frequency Analysis and Mode Identification for Asteroseismology) was developed by Zima (2008). It is a package of several tools for the analysis of photometric and spectroscopic time-series data.

Within the FAMIAS package a discrete Fourier transform is computed to search for periodicities in data sets. This can be done for a time series of a single variable, for instance moments, equivalent widths, radial velocities, photometric magnitudes or other variables, or for a time-series of spectra (in this case, two-dimensional data) for which we use a pixel-by-pixel frequency search averaged over the whole line profile.

SigSpec (Reegen, 2007) was also adopted for the frequency analysis. SigSpec identifies the most significant frequency based on its "spectral significance", then searches for further frequencies after prewhitening the data. This is repeated until a "spectral significance" threshold is reached. The evaluation of the "spectral significance" is based on an analytical solution of the probability that a discrete Fourier transform peak of a given amplitude does not arise from white noise. The underlying probability density function of the amplitude spectrum generated by white noise is evaluated. From this, a false-alarm probability can be calculated for each frequency. The spectral significance is the inverse of the false-alarm probability scaled logarithmically. In this way, a peak identified with a significance of 10 means that it has a probability of 10^{-10} of being produced by white noise. SigSpec is only used to identify frequencies in the equivalent width, radial velocity and LPAP data because it can only treat mono-dimensional data.

The default value for the spectral significance threshold is 5.46 but more conservative thresholds were adopted because a great degree of confidence is required in the frequency determination to perform a mode identification. For instance, thresholds of 15 and 10 were used respectively for HD 189631 and AC Lep.

For each method the frequency content was determined by following a typical prewhitening procedure:

1. Examine the highest peaks in the Fourier transform of the data.
2. Select the highest peak.
3. Remove the frequency by subtracting a least-squares fit to the data.

4. Examine highest peaks in the Fourier transform of the residual data.

5. Select the highest peak that is not caused by aliasing patterns.

6. Remove all the selected frequencies simultaneously by subtracting a multi-frequency least-squares fit to the original data (the data before removal of any frequencies).

7. Repeat steps 4 to 6 until no more significant frequencies remain.

The significance of frequencies is determined by the spectral significance criterion defined in SigSpec. It can vary depending on which star is being analyzed.

3.5.1 Uncertainties in frequency determination

We evaluate uncertainties in our frequency determinations by using the technique of Kallinger et al. (2008). Based on extensive simulations, those authors find that the frequency errors are overestimated when using the classical Fourier criterion, which uses the Rayleigh frequency resolution (T^{-1}), defined by the total time base of the data set. They propose instead a formula already proposed by Montgomery and Odonoghue (1999):

$$\sigma(f) = \frac{1}{T * \sqrt{sig(a)}} \tag{3.4}$$

where $\sigma(f)$ is the error in frequency; T is the time base of the observations in days and $sig(a)$ denotes the spectral significance of an individual frequency with amplitude a. This last quantity, described in the previous page, is calculated by the SigSpec software.

3.5.2 Moment variations

As described by Balona (1986), the n^{th} moment of a continuous frequency distribution $f(x)$ with respect to the origin is defined as

$$M_n = \int_{-\infty}^{\infty} x^n f(x) dx \tag{3.5}$$

In the case of a line profile, x represents the wavelength λ and

$$f(\lambda) = 1 - I(\lambda) \tag{3.6}$$

where $I(\lambda)$ is the normalized flux value. A simplification of Equation 3.5 can be done for the 0^{th} and the 1^{st} moments which correspond respectively to the equivalent width (EW) and the radial velocity (RV) of the line profile,

$$M_0 = EW = \sum_{i=1}^{n}(1 - I_i)\Delta x_i \tag{3.7}$$

and

$$M_1 = RV = \frac{\sum_{i=1}^{n}(1 - I_i)(x_i - x_0)\Delta x_i}{\sum_{i=1}^{n}(1 - I_i)\Delta x_i}. \tag{3.8}$$

In the above equations, I_i is the normalized flux measured at wavelength pixel λ_i, $\Delta x_i = x_i - x_{i-1}$ and x_i is the velocity corresponding to λ_i with respect to the laboratory wavelength λ_0. This defines the radial velocity as the line centroid, as stated by Aerts et al. (2004b). The variations of both of these parameters are investigated in this thesis.

For non-radial pulsations, equivalent width variations are indicative of temperature and brightness changes occurring in the stellar atmosphere. In such cases the variations should occur at the pulsation frequencies present in that star. Therefore the variation of equivalent width in the line profile for each target star is analyzed and the resulting frequencies and their associated amplitudes discussed.

For low to moderate degree ($\ell < 5$) modes, the LPVs can be detected as velocity variations. Because this measurement is made over the whole spectral line it is integrating across the entire stellar surface. For this reason it is similar to photometry which can only detect lower degree modes due to the geometrical cancellation effects present in higher degree modes.

For both the EW and RV determination, a fixed range of velocities, centred on the line profile, was considered. It needs to be sufficiently large to encompass the whole line profile through all of its variations. A poor continuum fit can affect both the EW and RV determination so it is important that the continuum fitting is done very carefully.

3.5.3 Pixel-by-pixel variations

The pixel-by-pixel method is a two-dimensional method described by Mantegazza (2000). The normalized intensity variation of every single pixel in the line profile is analyzed as a time series and a Fourier spectrum produced for each. An average of these Fourier spectra is then taken.

Figure 3.8 shows an example of this method applied to the first frequency of PT Pup. Looking for frequencies in each pixel allows one to observe in which part of the line profile a pulsation frequency is occurring. In this case it can clearly be seen that the pulsation is much stronger in the wings than in the centre of the line, as shown by the fact that the standard deviation of each pixel across the profile (green), representing the amplitude variations from the mean line profile (blue) is largest in the wings.

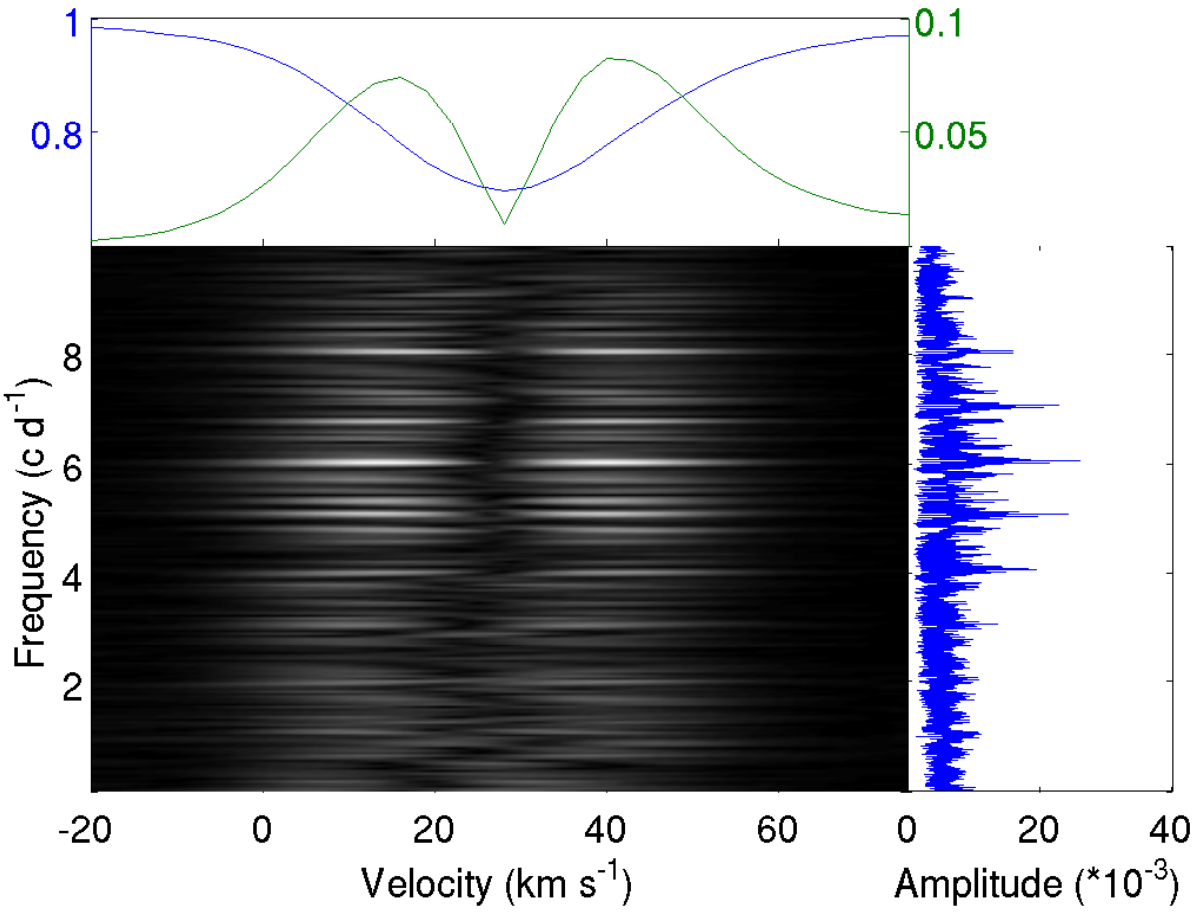

Figure 3.8: Frequency determination using the pixel-by-pixel method. The top panel shows the mean line profile and its amplitude variations. The central panel is showing all of the Fourier transforms computed for the variations of intensity in each pixel. Clear areas correspond to peaks while black zones are close to zero. An average of all these Fourier transforms is taken and displayed on the right panel.

To prewhiten the data by the identified frequencies, the phase and amplitude of the least-squares fit across the profile were determined. These phase and amplitude variations are later used by the Fourier Parameter Fit (FPF) method for the mode identification. The errors for the phase and amplitude across the profile are based on the residual of the final multi-frequency fit to the data.

The pixel-by-pixel frequency analysis method is appropriate for lines of moderate to high $v \sin i$ where the variation in the line profile is spread over a relatively large wavelength range and therefore a large number of pixels. The method is more sensitive to higher degree ℓ modes than are frequencies extracted from the velocity measurements of a line profile (Mantegazza, 2000).

3.5.4 Asymmetry of the line profile

As stated in section 3.4 when investigating the radial velocity by the bisector method, the slope of the bisector was calculated to represent the asymmetry in the line profile. This is referred to as the line profile asymmetry parameter (LPAP). It is the slope of a straight line between two points on the bisector of the line, at 50% and 90% of line depth, given by:

$$LPAP = \frac{v_{90} - v_{50}}{0.9 - 0.5} \tag{3.9}$$

where v_{90} and v_{50} are the radial velocities of the bisector measured at 90% and 50% of the line depth respectively. The LPAP computed for each observation forms a new data set which we can analyze.

The LPAP is a new diagnostic tool invented in this thesis. This method is independent of the wavelength, the velocity shift and the flux of the line considered and, contrary to previous methods, does not require a preselected wavelength range. The amplitude of the variations are proportional to the $v \sin i$ of the star, but amplitudes of pulsations vary greatly from star to star so we cannot use this as an estimation of $v \sin i$.

As for mode identification, this method cannot detect axisymmetric ($m = 0$) modes. This, of course, includes the radial mode. Because of the symmetric nature of axisymmetric ($m = 0$) modes, the asymmetry of the line profile is not affected. Observing strong variations in the LPAP is therefore an indication of a pulsation where $\ell > 0$ and $m > 0$.

3.6 Mode identification

To find the pulsational modes of the targeted stars, we use the Fourier Parameter Fit (FPF) method developed by Zima (2006), within the FAMIAS software package. It relies on a direct fit to the three Fourier parameters: zero point, amplitude and phase across the line profile. These are displayed in Figure 3.9 for the particular case of the primary pulsation in AC Lep. The uncertainties in the derived parameters are determined from the residual variations in the prewhitened data.

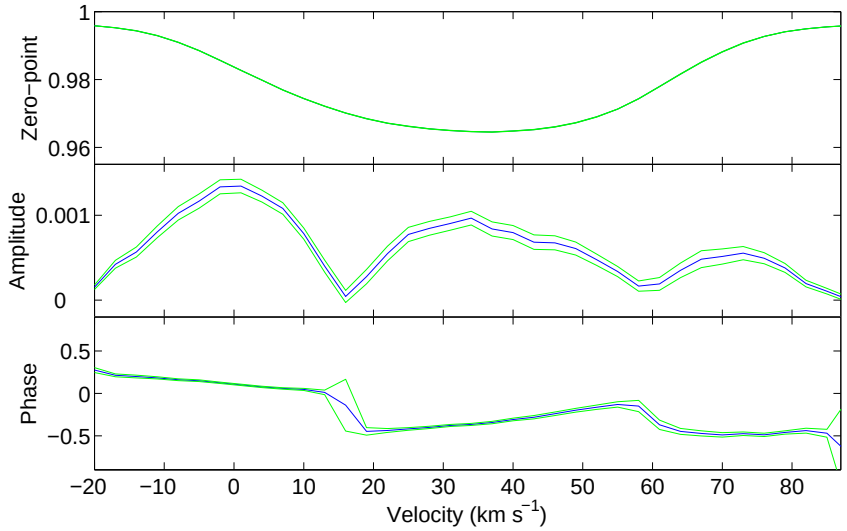

Figure 3.9: Fourier parameters for the primary pulsation of AC Lep. From top to bottom: the zero-point profile, the amplitude (both in normalized intensity) and the phase across the profile (dimensionless). The data is in blue, surrounded by its uncertainty ranges in green.

The various fits attempted are models which differ by their non-radial wavenumbers, ℓ and m, but also by the amplitude and phase of the variations. In order to improve the fit, other parameters are allowed to vary, such as stellar characteristics (stellar mass and radius, effective temperature, inclination angle, $v \sin i$, $[Fe/H]$) and spectral line characteristics (equivalent width, intrinsic width, radial velocity shift). The goodness of the fit is determined by a reduced χ^2 value calculated from the three fits combined. However, the zero-point fit dominates the other two in the evaluation of the χ^2. Since our data can show an asymmetry in the line profile, and because the program only fits

symmetric lines, the zero-point fit is never excellent. For that reason we ignore this fit to concentrate on the amplitude and phase fits.

The radius, the effective temperature and metallicity of the star have negligible effects on our mode identification. The equivalent width of the spectral line is evaluated from the cross-correlated spectral line and thus has the units of km.s^{-1}. Its determination is very precise and so it is not allowed to vary in order to identify the mode of pulsation. However the v sin i, radial velocity and intrinsic width (σ) are allowed to vary. The stellar mass and the gravity at the surface affect the vertical-to-horizontal ratio of the pulsations, thus producing g-mode behaviour (horizontal movement, i.e. parallel to the surface) or p-mode behaviour (vertical movement, i.e. perpendicular to the surface).

In summary, this chapter has described the tools that we need to carry out the analysis of our three target stars. The β Cephei star, PT Pup, is analyzed first in Chapter 4, and the two γ Doradus stars, HD 189631 (Chapter 5) and AC Lep (Chapter 6), are then analyzed in that order.

Chapter 4

PT Puppis

PT Puppis is also named HR 2928, HIP 37036 or HD 61068. With its coordinates (RA: 07 36 41; DEC: -19 42 08; epoch = 2000) it can be seen in summer in the southern hemisphere. Shobbrook (1981) observed it and classified it as a β Cephei star, detecting two pulsations. Several other studies have been made on this star, of which Stankov and Handler (2005) summarizes all previous studies and Hubrig et al. (2009) provides a list of basic properties.

4.1 Observations

A total of 161 spectra were obtained for this star, all taken from MJUO by Florian Maisonneuve and Pam Kilmartin. Figure 4.1 is a histogram showing a complete overview of the observing sessions of PT Pup. An initial set of observations in 2007/8 (17 spectra) collected a few spectra of various potential targets. After selecting this star as a main target, a dedicated observing campaign was designed for the following year (2008/9) where most of the data (144 spectra) were taken.

4.2 Properties

Lefèvre et al. (2009) report a spectral type of B 2 II for PT Pup. It has a visual magnitude of 5.69 *mag*. Estimates of the effective temperature, mass, radius and log g can be found in the literature and are listed by Hubrig et al. (2009):

- $T_{eff} = 23800 \pm 1100$ K (Napiwotzki et al., 1993)

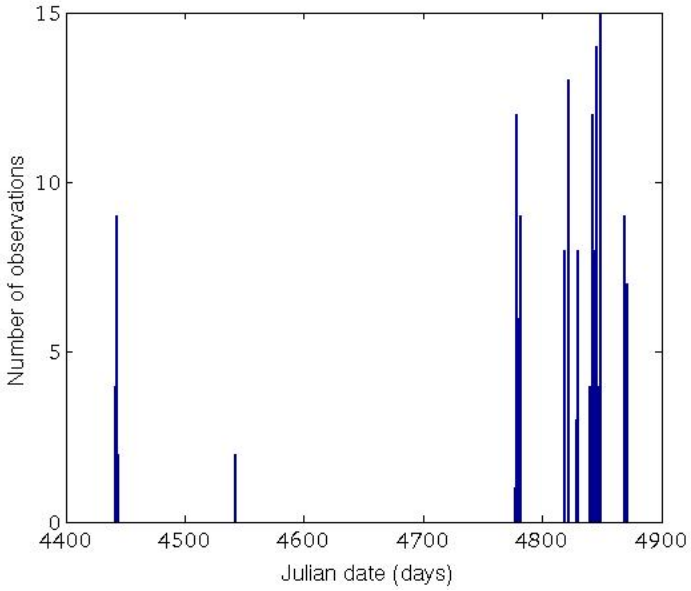

Figure 4.1: Full data sampling for PT Pup. The complete data set of PT Pup is represented on this histogram. The dates shown are JD-2450000.

- $M = 10.1 \pm 0.8\ M_{\odot}$
- $R = 5.4 \pm 0.9\ R_{\odot}$
- $\log\ g = 4.0 \pm 0.2$

4.2.1 Overview of spectrum

In Figure 4.2 the complete spectrum of PT Pup is shown, obtained by taking the mean of all 161 observations. The most important spectral lines are identified and listed in Table 4.1.

When working on hot stars like β Cephei variables, previous studies done by Aerts et al. (2003), Aerts et al. (2004b), Telting et al. (2006) or Wright (2008) usually use strong isolated lines for their analysis. These objects are bright and in general very good signal to noise data are obtained, thus cross-correlation is not needed. Furthermore, Wright (2008) found that lines produced by different species can vary out of phase, but with the same frequency.

The identification of all strong lines in the spectrum of PT Pup shows the possibilities for any subsequent analysis. Note that many O II and N II lines are present. The

cross-correlation of these were undertaken separately, isolating the species in case they do not pulsate in phase. Table 4.1 lists the ionization and excitation potentials for each spectral line, giving some indication of the relative depth at which they are forming.

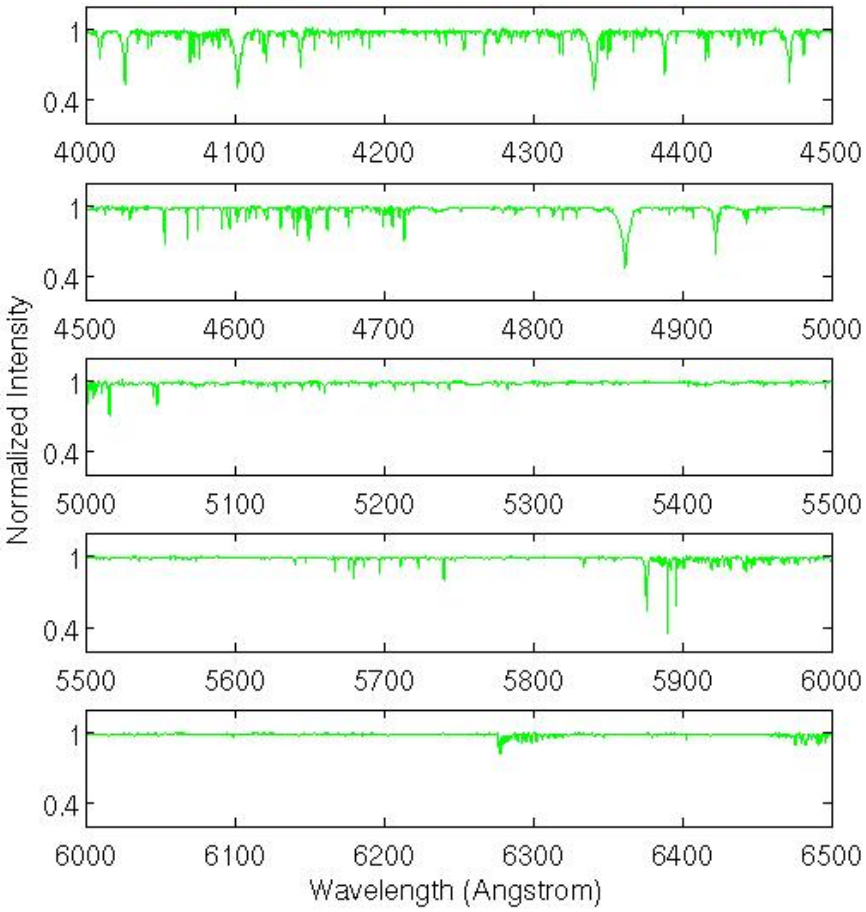

Figure 4.2: Average spectrum of PT Pup. The full spectrum is divided into five sections of 500 Å each, starting at 4000 Å and finishing at 6500 Å.

4.2.2 Line profile variation

After just a few spectroscopic observations of PT Pup the line profile variation (LPV) was very prominent. Figure 4.3 shows the Si III line at 4552 Å extracted from all of our 161 observations, together with the mean of all observations. The shape of the line doesn't seem to be much affected by the pulsation while its radial velocity is changing

Table 4.1: Spectrum of PT Pup - List of strong spectral lines in PT Pup

Species	IP (eV)	λ (Å)	EP (eV)	λ (Å)	EP (eV)	λ (Å)	EP (eV)	λ (Å)	EP (eV)
H I	13.6	4102	10.15	4340	10.15	4861	10.15	6563	10.15
He I		4009	21.13	4026	20.87	4121	20.87	4144	21.13
		4169	21.13	4388	21.13	4438	21.13	4471	20.87
		4713	20.87	4922	21.13	5016	20.53	5048	21.13
		5876	20.87	6678	21.13				
C II	11.26	4267	17.97	5890	17.97	5892	17.97	6578	14.39
		6583	14.39						
C III	24.38	4647	29.39						
N II	14.53	4237	23.14	4242	23.14	4530	23.37	4601	18.39
		4607	18.38	4614	18.39	4621	18.39	4631	18.40
		4643	18.40	5001	20.56	5005	20.58	5045	18.40
		5667	18.39	5676	18.38	5680	18.40	5711	18.40
		5932	21.06	5942	21.07	6482	18.42		
O II	13.62	4070	25.53	4072	25.54	4076	25.55	4089	28.58
		4119	25.74	4153	25.73	4185	28.24	4190	28.24
		4317	23.32	4320	22.88	4346	22.88	4347	25.55
		4349	22.90	4351	25.55	4367	22.90	4415	23.34
		4417	23.32	4591	25.55	4596	25.55	4610	28.94
		4639	22.87	4642	22.88	4649	22.90	4651	22.87
		4662	22.88	4676	22.90	4699	26.11	4705	26.14
		4925	26.19	4943	26.45				
Ne I		6402	16.55						
Mg II	7.65	4481	8.83						
Al III	18.83	4529	17.74	5696	15.57	5723	15.57		
Si III	16.35	4553	18.92	4568	18.92	4575	18.92	4820	25.86
		4829	25.86	5740	19.64				
S II	10.36	4254	14.01						
S III	23.33	4254	18.17						
Fe III	16.18	4165	20.54	5834	18.43				

with a large (≈ 25 km.s^{-1}) amplitude. This is indicative of a low degree pulsation.

The line profile variations are represented in a colour plot on Figure 4.4 where the mean of all observations has been subtracted from each individual spectral observation of this line.

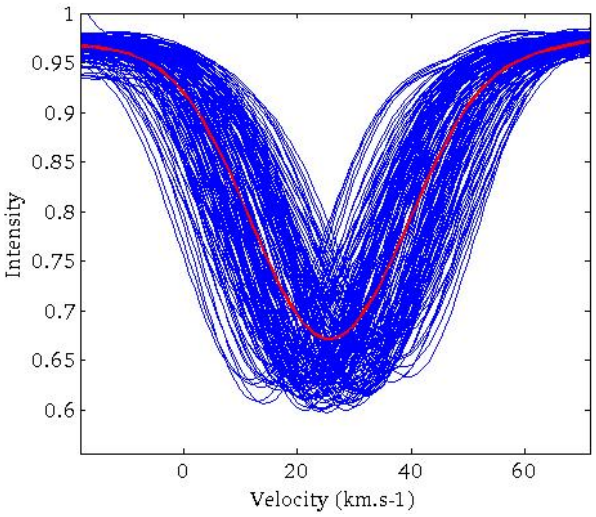

Figure 4.3: Variation of the spectral line of PT Pup. The Si III line at 4552 Å taken from 161 observations of PT Pup is found strongly varying. The mean of all observations is shown in red.

4.2.3 v sin i

This star has a very low rotational velocity which makes its exact determination difficult. Abt et al. (2002) measured v sin $i = 10 \pm 9$ km.s^{-1} using an averaged value between the He I line at 4471 Å and the Mg II line at 4481 Å from a single spectrum.

Both our methods to determine v sin i failed on this star. The velocity is too low to have a big impact of the broadening of the spectral line, which is necessary for its measurement. The line is therefore broadened mostly by thermal broadening effects.

4.2.4 Radial velocity

In his compilation of radial velocity for 35495 stars, Gontcharov (2006) reports a radial velocity of 22.0 ± 4.3 km.s^{-1} for this object. We use the bisector method and measure the radial velocity at 50% of the line depth to find a value of 25.8 ± 0.3 km.s^{-1}. Our

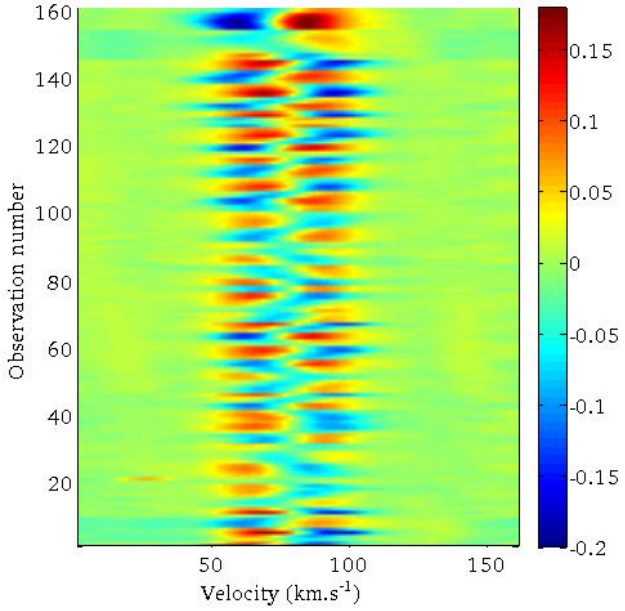

Figure 4.4: Line profile variation of PT Pup. This colour plot shows the residuals of the Si III spectral line from all observations after subtraction of the mean.

measurement was done on the Si III line at 4552 Å as it is strong and well isolated. Figure 4.5 shows the Si III spectral line averaged over our 161 observations. The radial velocity measured at different depths of the spectral line are listed in Table 4.2. From these data we can note a very small asymmetry with the lower part of the line being skewed towards lower velocities, i.e. towards the blue. The line profile asymmetry parameter (LPAP) representing this asymmetry from 50% to 90% depth is -0.25 km.s^{-1}. This is expected as only a perfect sampling of all the pulsations would give a value of 0 km.s^{-1}.

4.3 Frequency analysis

In order to analyze the Fourier frequency graphs the spectral window was calculated (Figure 4.6). A spectral window shows which aliasing peaks will be enhanced due to the data sampling. Since all of our observations for this star were taken from a single site (MJUO), it is expected to see strong aliasing patterns at $\pm$ 1, $\pm$ 2 days around the true frequency(ies).

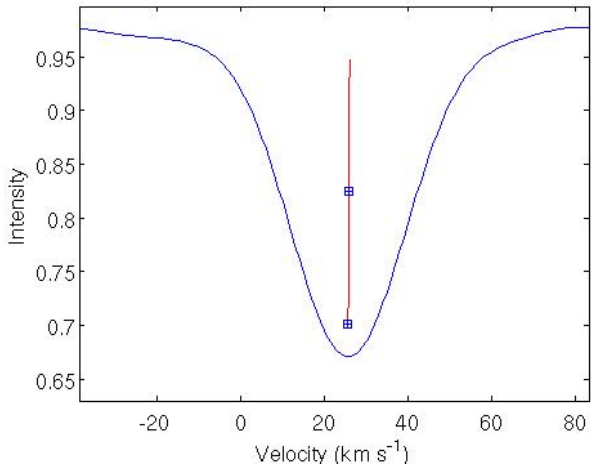

Figure 4.5: The mean of 161 observations of the Si III line at 4552 Åin PT Pup. The central line is its bisector. The two symbols are situated at 50% and 90% of the line depth.

Table 4.2: Radial velocity measured at different depths of the mean Si III spectral line for PT Pup.

Line depth (in %)	Velocity (km.s^{-1})
20	25.90
30	25.85
40	25.80
50	25.77
60	25.74
70	25.72
80	25.70
90	25.67

The other strong peaks seen in the spectral window are very close to the true frequency. Figure 4.7 shows the spectral window within ± 0.2 d^{-1} centered around zero.

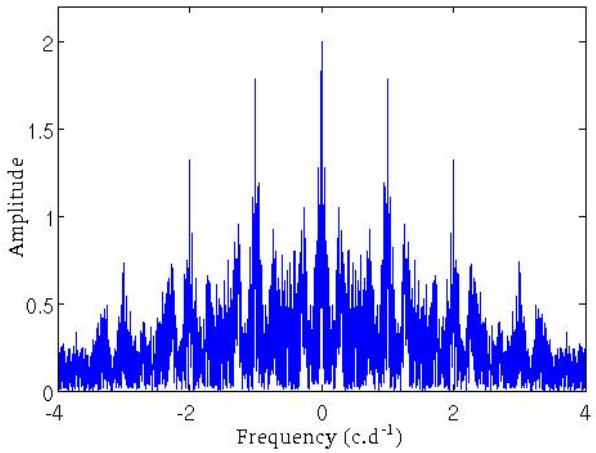

Figure 4.6: Spectral window for PT Pup. It is showing the expected aliasing pattern due to our data sampling.

4.3.1 Photometric frequency analysis

Heynderickx (1992) reports two pulsation frequencies : $f_1 = 6.01016 \pm 0.00001$ d^{-1} and $f_2 = 6.06352 \pm 0.00002$ d^{-1} while noting aliasing problems in his frequency determinations. We also encountered aliasing problems when analyzing the first group of our spectroscopic data (about 60 observations).

The Hipparcos data for this star was analyzed by Koen and Eyer (2002) and by Lefèvre et al. (2009). They do not confirm the periodicities listed by Heynderickx (1992). Using 138 photometric observations, Koen and Eyer (2002) identify a primary frequency at $f = 5.51115$ d^{-1}, while Lefèvre et al. (2009) identify the primary frequency at $f = 0.9515$ d^{-1}.

4.3.2 SiIII at 4552 Å

This line was chosen for our analysis because it is a strong, single and well isolated line.

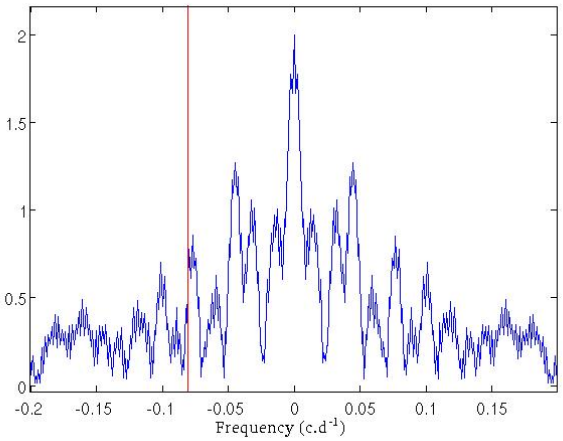

Figure 4.7: Enlarged version of the spectral window for PT Pup. Secondary peaks will be found near the true frequency. The vertical red line corresponds to the location of the possible secondary frequency.

4.3.2.1 Equivalent width frequency analysis

The equivalent width analysis shows no significant periodic variations (Figure 4.8). Although the primary frequency is very strong, it has no significant effect on the equivalent width. Higher peaks near zero in the amplitude spectrum suggest a slow drift in the measured equivalent width over time. To investigate this further we show the complete data set of equivalent widths on Figure 4.9. Some variations are present but the Fourier analysis fails to determine any periodicities in this data. A long slow drift is arguably present, but it has a low amplitude which is well below the other variations in the data. Our method of measuring the equivalent width is not precise enough to draw any conclusions on this hypothetical long drift.

4.3.2.2 Radial velocity frequency analysis

Analyzing the variations of the radial velocity measured in Si III gives the primary frequency $f_1 = 6.07432$ d^{-1} (Figure 4.10), with an amplitude of 4.38 km.s^{-1}. This frequency is very strong and corresponds to the secondary frequency of Heynderickx (1992). It is dominating other frequencies to such an extent that the top panel of Figure 4.10 is comparable to the spectral window seen in Figure 4.6. After prewhitening the radial velocity data with the first frequency, a second frequency at $f_2 = 5.99375$ d^{-1} is

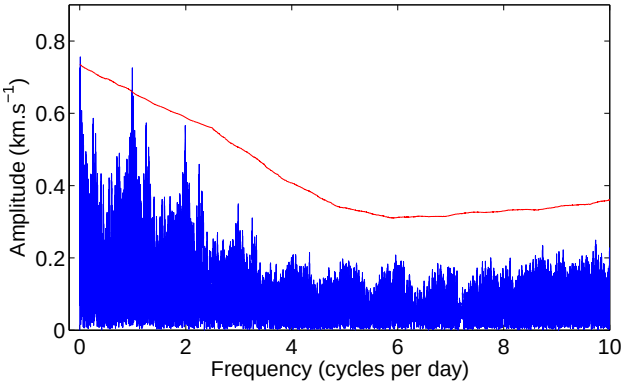

Figure 4.8: Fourier analysis of the variation in equivalent width of the spectral line Si III at 4552 Åin PT Pup. No frequencies can be identified from this analysis. The peak at one cycle per day is expected. It is due to our data being from a single site.

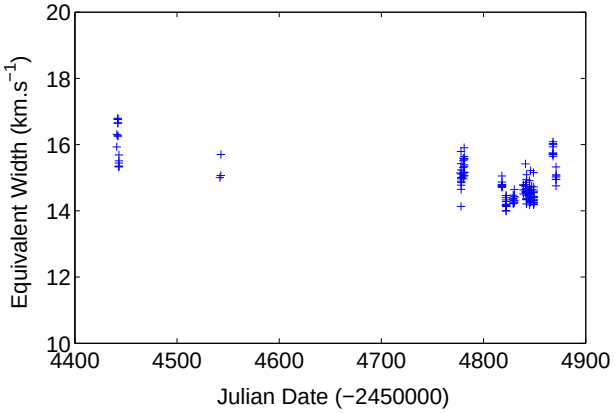

Figure 4.9: Variation of the equivalent width of the spectral line Si III at 4552 Åin PT Pup. The complete data set is represented.

identified. It has a much lower amplitude (1.88 km.s^{-1}) and is found at the detection limit. It could correspond to the primary frequency found by Heynderickx (1992). It is interesting to note that this author suggests some amplitude variability in the data. After removing f_2, no other frequencies can be found.

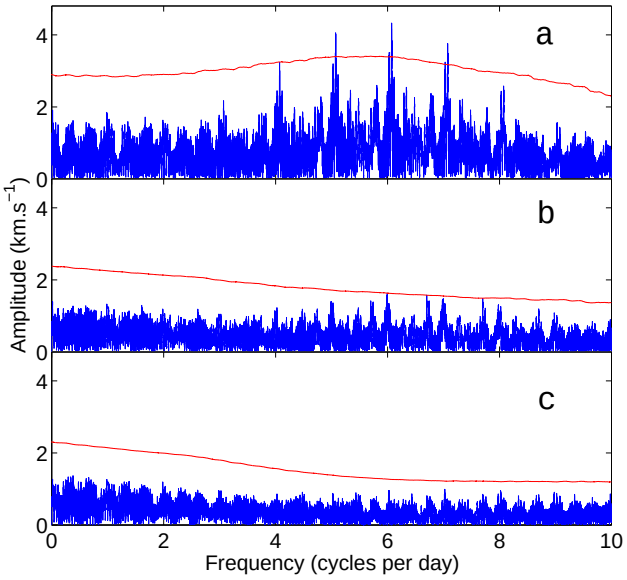

Figure 4.10: Fourier analysis of the variation in radial velocity of the spectral line Si III at 4552 Åin PT Pup. (a) The primary frequency is clearly identified at $f_1 = 6.0743$ d^{-1}. (b) After prewhitening with f_1 a secondary frequency at $f_2 = 5.9937$ d^{-1} is identified. (c) Shows the noise floor. The red line represents our limit of detection.

Figure 4.11 shows the data phased on f_1 and f_2 with their respective fits. The fit to the primary pulsation explains 63% of the variations. After prewhitening the data and phasing it on the secondary frequency the amplitude of the variation is much lower than for the primary. Fitting both frequencies to our data set accounts for 69% of the radial velocity variations.

4.3.2.3 Pixel-by-pixel frequency analysis

The pixel-by-pixel frequency analysis confirms the frequencies found previously, namely $f_1 = 6.07432$ d^{-1} and $f_2 = 5.9938$ d^{-1} (Figure 4.12). Once again the amplitude of the variation is much higher for the primary than for the secondary pulsation.

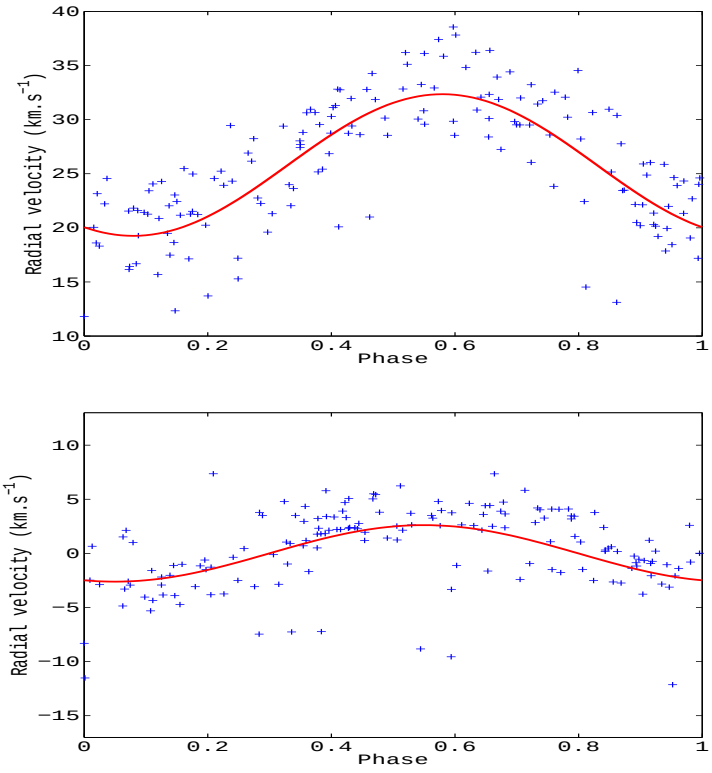

Figure 4.11: Radial velocity variations of PT Pup phased on f_1 and f_2. (top) Radial velocity variations observed in Si III at 4552 Å phased on $f_1 = 6.0743$ d^{-1}. The fit is shown by the red line. (bottom) After prewhitening with f_1 the data is rephased on $f_2 = 5.9937$. The amplitude of pulsation is significantly lower than for the primary frequency.

The pixel-by-pixel method is fitting a different pulsational amplitude to each pixel independently. It also recognizes that all pixels are not pulsating in phase. Therefore computing a phase across the profile represents the phase shift between different parts of the line profile. In Figure 4.13 the line profile variations are shown after removing the mean of all observations phased on the primary frequency. A strong beat pattern is visible, indicative of a low degree mode. The amplitude and phase across the profile derived from the data can be used to produce a fit shown on the top right panel of Figure 4.13. This fit accounts for 54% of the variations observed in our data set.

Prewhitening the data with the first frequency is equivalent to subtracting the top right panel (b) of Figure 4.13 from its top left panel (a). Re-phasing this prewhitened data on the secondary frequency produces the lower part of Figure 4.13, on which one can see another beat pattern, but not as clear as for the first pulsation. The amplitude of variation is also smaller by a factor of 2.5 compared to the first pulsation. This can be seen on the right hand side of the figures where the scale of the amplitudes are displayed on the colour bars. Once again a fit can be produced using the amplitude and phase across the profile which is displayed on the bottom right panel of Figure 4.13. Using the fits to both frequencies explains 56% of the observed variations, which underlines some uncertainty in the detection of f_2, since f_1 alone could explain 54% of the variations.

4.3.2.4 Investigating the asymmetry in the line profile

The LPAP was computed for each observation and its variations were analyzed. The LPAP is a representation of the asymmetry of the spectral line. It seems that the pulsations do not affect the asymmetry of the line as much as they affect the radial velocity, since the amplitudes of variations observed are quite low. This is indicative of a low degree mode, possibly an axisymmetric mode.

Figure 4.14 shows the frequency spectrum, in which the primary frequency is at $f_1 = 6.0274$ d^{-1}. After prewhitening, a peak may be detectable at the location of the identified secondary frequency (observed in the radial velocity data and found with the pixel-by-pixel frequency determination) but it is under our detection threshold.

In Figure 4.15 each observations has been phased on $f_1 = 6.0274$ d^{-1} and fitted to the data. This fit accounts for 21% of the variations of the LPAP in the data set.

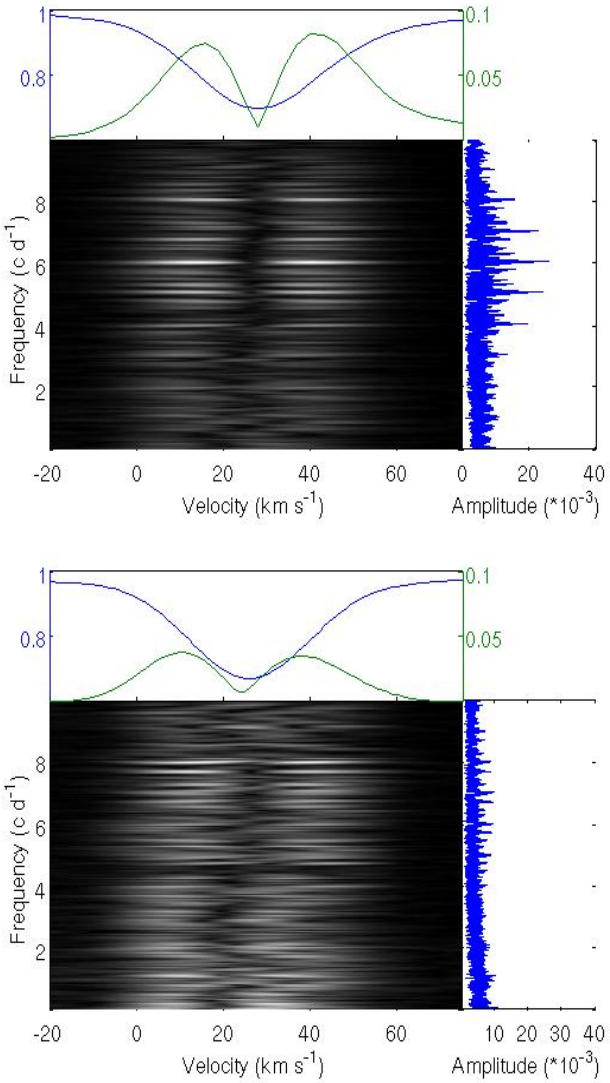

Figure 4.12: Fourier analysis for PT Pup using the pixel-by-pixel method. (top) The primary frequency is again clearly identified. The top panel shows the mean Si III line and its amplitude variation, the central panel shows the two dimensional Fourier analysis and the right panel is an average of this two dimensional data, showing the strong peak of the primary frequency $f_1 = 6.0743$ d^{-1}.. (bottom) After prewhitening the data for the primary frequency we detect a secondary frequency at $f_2 = 5.9938$ d^{-1}.

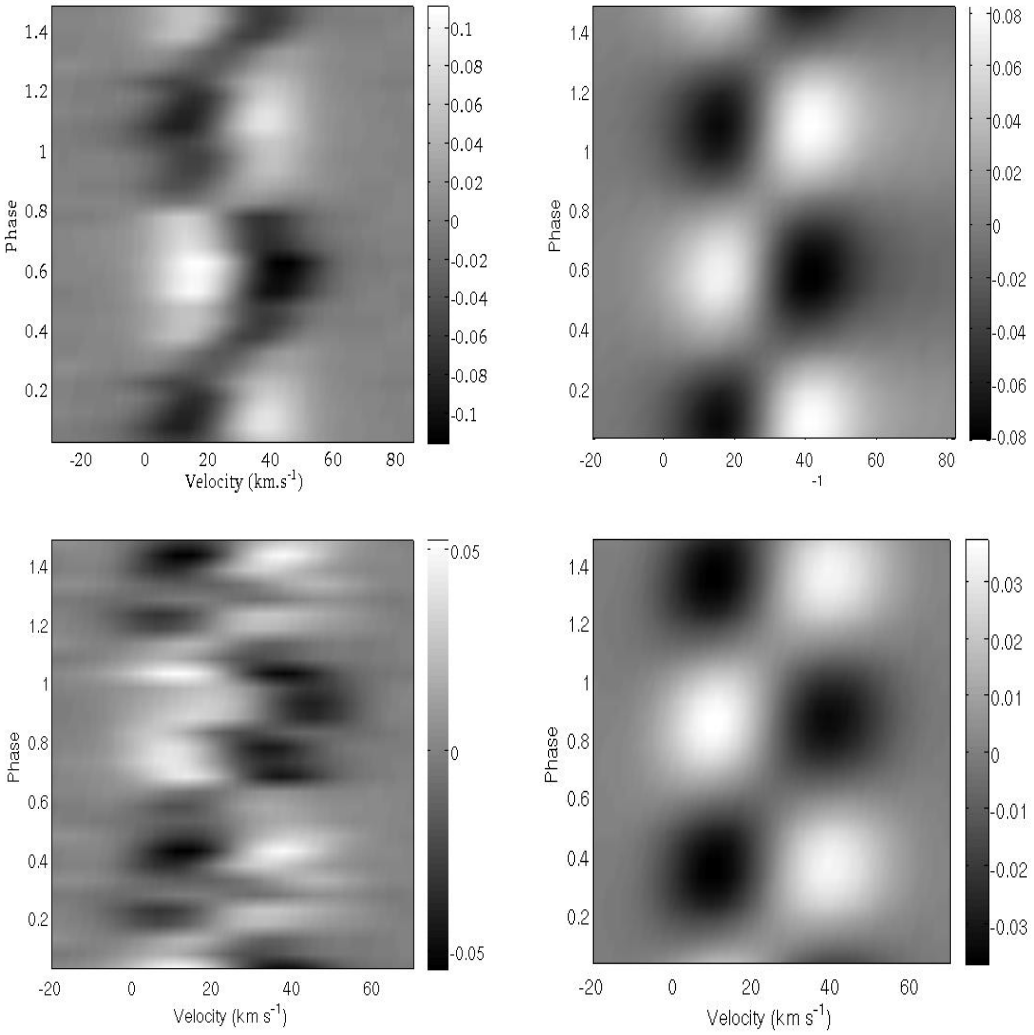

Figure 4.13: Phased line profile variation (LPV) data for PT Pup. (a) Line profile variations observed in Si III at 4552 Å phased on $f_1 = 6.0743$ d^{-1}. A clear beating pattern is visible, indicative of a strong pulsation. (b) A least-squares fit to the data with the amplitudes and phases across the profile derived for f_1 for each pixel in the line profile. The average line profile has been subtracted from all observations. (c) Line profile variation observed in PT Pup after prewhitening with f_1 and phased on $f_2 = 5.9938$ d^{-1}. (d) A least-squares fit to the data with the amplitudes and phases across the profile derived for f_2. The average line profile has been subtracted from all observations.

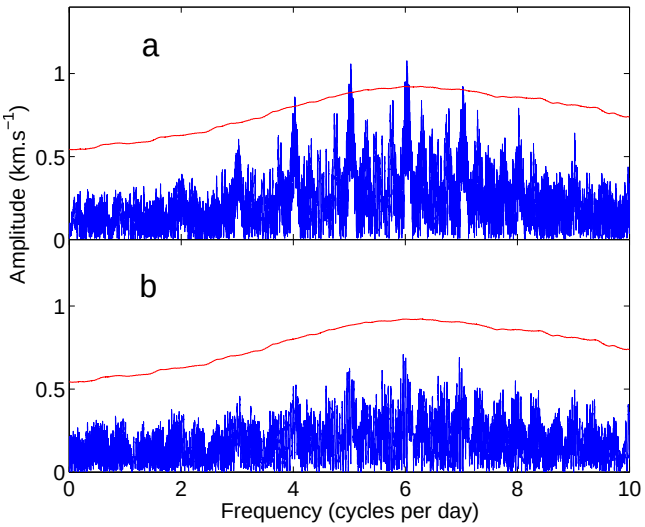

Figure 4.14: Fourier analysis of the variations in the line profile asymmetry parameter (LPAP) for PT Pup. (a) Identification of the primary frequency, $f_1 = 6.0274$ d^{-1}. (b) After prewhitening for f_1 the amplitude spectrum is below the noise floor (solid line).

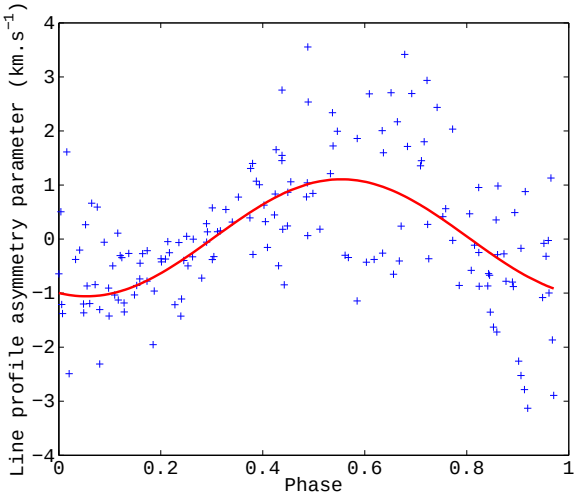

Figure 4.15: Values of the LPAP for each observation of PT Pup phased on f_1. The continuous red line is a fit to the data.

4.3.3 Other lines and cross correlated result

All the previous work has been done on a single line, but it is important to perform the same analysis on other spectral lines. Two frequently chosen lines for analysis are He I lines at 4713 Å and 5876 Å . Two other lines from Table 4.1 were also selected due to their extremely different ionization potentials (IP): Mg II (4481 Å) with a low IP of 7.35 eV and C III (4647 Å) with a high IP of 24.38 eV. There are many lines of O II and N II and so an independent cross-correlation was performed on both of these species, using respectively 137 and 98 spectral lines.

Figure 4.16 is a plot of the radial velocities measured for each of these species over a single night containing 14 observations of PT Pup. The low signal of the Mg II and especially the C III lines can cause the measure of the radial velocity to be wrong, producing a few outliers. This figure proves that all lines, from weak to strong, from low to high ionization potential, are affected by the same pulsation and are *in phase*. This is a prerequisite to any further cross-correlation. A full cross-correlation was then preformed and the data set produced can be analyzed together with the other data sets for each line or species.

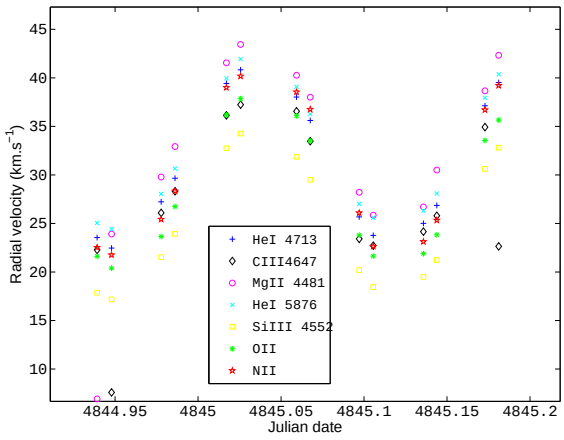

Figure 4.16: Radial velocities of different species for PT Pup.. All the spectral lines are varying in phase and with comparable amplitudes.

Table 4.3 lists the results of all our analysis on each species. An obvious conclusion from this table is that all the lines vary with the same frequencies. The main frequency is always very strong while the secondary frequency cannot always be detected. It

is interesting to note that with the cross-correlated data, the frequencies become detectable in the equivalent width variations. This is because there are many lines in the cross-correlation function and some of them are not isolated, which introduces some asymmetry in the resulting line profile. The equivalent width determination is then affected by a radial velocity shift. To avoid this effect it is necessary to change the boundaries of the equivalent width evaluation according to the frequency and amplitude of the radial velocity variations. This would suppose that frequency of the main pulsation (or even the secondary) is already known, but its determination is our motivation for changing the way in which the equivalent width is calculated, hence it was decided not to proceed in this way.

The analysis of the equivalent width and radial velocity variations for the cross-correlated profile are shown respectively on Figures 4.17 and 4.18. They are very similar to the radial velocity Fourier analysis done for the Si III line (Figure 4.10). From this it is concluded that even if all the lines vary with the same frequencies and in phase, a cross-correlation is not necessary. PT Pup is bright and the signal to noise ratio is very good in individual lines, allowing the analysis to be performed with as much (if not better) confidence as doing it on a cross-correlated profile.

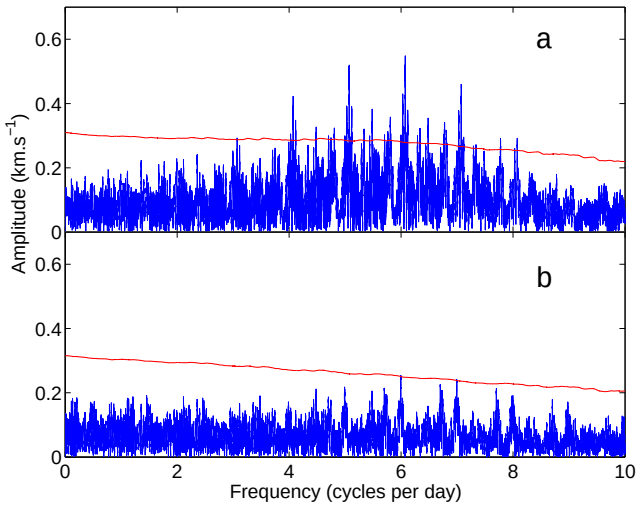

Figure 4.17: Fourier analysis of the variations in equivalent width from the cross-correlated data of PT Pup. (a) detects $f_1 = 6.0743$ d^{-1} and (b) detects $f_2 = 5.9938$ d^{-1}.

Table 4.3: Frequency analysis done on eight different spectral lines or cross-correlated profiles for PT Pup. The four methods of analysis are the variations in the equivalent width (EW), radial velocity (RV), pixel-by-pixel (P-b-P) and line profile asymmetry parameter (LPAP). All the frequencies listed are in units of d^{-1}.

Species	EW	RV	P-b-P	LPAP
Si III (4552 Å)		6.074	6.074	6.027
		5.994		
He I (4713 Å)		6.074	6.074	
He I (5876 Å)		6.074	6.074	
Mg II (4481 Å)		6.074	6.074	
		5.994		
C III (4647 Å)		6.074	6.074	
		5.994		
O II (137 lines)	6.074	6.074	6.074	5.996
N II (98 lines)	6.074	6.074	6.074	
Full CCF	6.074	6.074	6.074	5.998
	5.994	5.994	5.994	

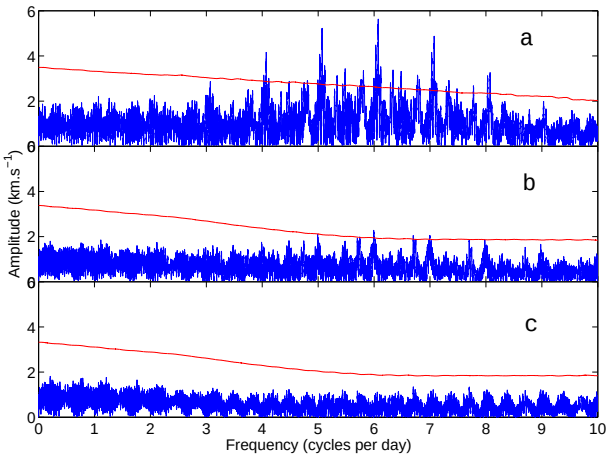

Figure 4.18: Fourier analysis of the variations in radial velocity for the cross-correlated data of PT Pup. (a) detects $f_1 = 6.0743$ d^{-1} and (b) detects $f_2 = 5.9938$ d^{-1}. This graph is very similar to the one shown on Figure 4.10 for the Si III line.

4.3.4 Summary of frequencies

Two frequencies are found, similar to the ones reported by Heynderickx (1992): $f_1 = 6.0743 \pm 0.0001$ d^{-1} and $f_2 = 5.9938 \pm 0.0002$ d^{-1}. With every method of detection, the amplitude of the primary pulsation 6.0743 d^{-1} is found to be greater than the amplitude of the secondary pulsation by a factor of about 2.5 whenever the secondary is detected. In the result of Heynderickx (1992) it appears to be the opposite with their primary frequency corresponding to our secondary and vice versa. This can be explained in two ways which seem to be both necessary in this case. Firstly, as calculated by Cugier et al. (1994), when determining the amplitude of pulsation the results are dependent on the degree ℓ and the method used. From Figure 6 of Cugier et al. (1994), the ratio of the radial velocity amplitude (in km.s^{-1}) to photometric amplitude (in mag)can be as low as 200 for $\ell = 2$ and as high as 1500 for $\ell = 0$. These values are dependent on stellar mass. We will see if mode identification can settle part of that issue. In order to provide confidence in our frequency determinations, Figure 4.19 shows the sampling of our data phased on the first and the second frequencies. Both frequencies are reasonably well sampled.

4.4 Mode identification

For the frequency analysis we perform a mode identification using the Si III line at 4552 Å. The only previous mode identification on this star was done by Heynderickx et al. (1994). From photometric observations they derived $\ell = 2 \pm 1$ for their primary pulsation which seems to correspond to our secondary, and $\ell = 0$ for their secondary which seems to be our primary.

All the parameters used for the mode identifications on the data of PT Pup are listed below. They are either taken from the literature or computed beforehand. The first set of parameters are not allowed to vary because we need to limit the parameter space in order to have the algorithm functioning at its best. It does not affect our results since these parameters have negligible effects on the mode identification.

- R= 5.4 R$_\odot$
- M= 10.6 M$_\odot$

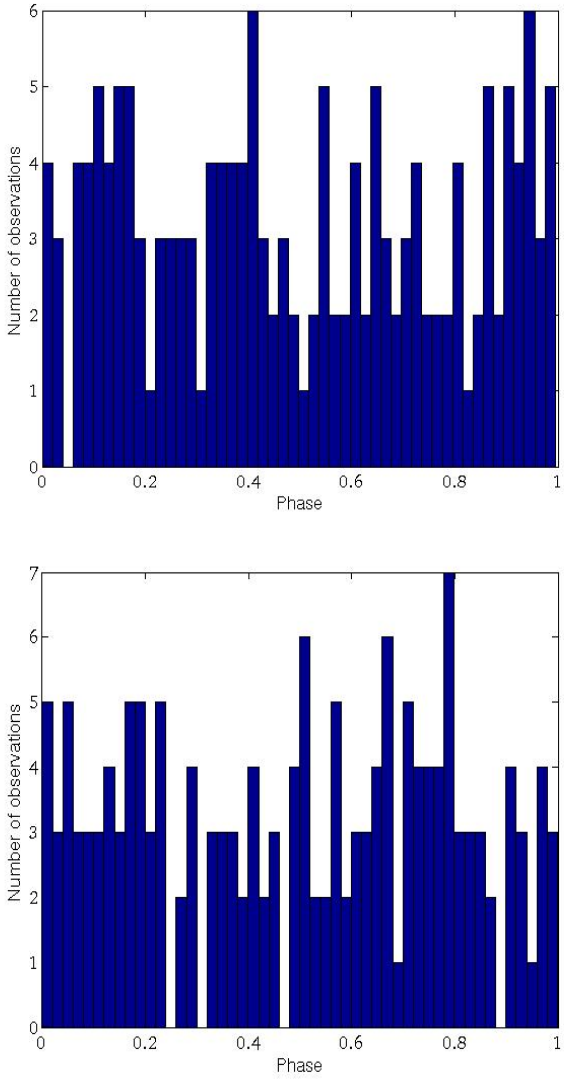

Figure 4.19: Data sampling. (top) Observations of PT Pup phased on (a) the primary frequency $f_1 = 6.0743$ d^{-1} and on (bottom) the secondary frequency$f_2 = 5.9938$ d^{-1}. These graphs show that the data is well sampled over both f_1 and f_2.

- $T_{eff} = 23800$ K
- $\log g = 4.00$
- $[Fe/H] = 0.00$

The following parameters, specific to the mean line profile, will be allowed to vary in order to improve the fit:

- $v \sin i$: 1 to 15 km.s^{-1}
- i : 5^o to 90^o
- Equivalent width : 10 to 13 km.s^{-1}
- Intrinsic width : 15 to 22 km.s^{-1}
- Zero-point shift (i.e. the radial velocity) : 24 to 29 km.s^{-1}

A large parameter space for the pulsational mode characteristics was explored for both frequencies. A low degree pulsational mode was suspected and so only values of $\ell \leq 3$ were investigated. This meant that the final set of variable parameters were:

- ℓ : 0 to 3
- m : $-\ell$ to $+\ell$
- Amplitude : 0.1 to 20 km.s^{-1}
- Phase : 0 to 2π

The primary pulsation is best fitted by a (1;+1) mode (Figure 4.20) with a very small χ^2 value of 0.97. This is an extremely good fit. However there are two other likely modes: (0;0) and (1;0) with respective χ^2 values of 1.56 and 1.59. The difference between these modes can be seen on the phase across the profile. It shows that the left and right parts of the line profile are moving out of phase in all three cases, but for (0;0) and (1;0) the transition between these two parts is very sharp (see Figure 4.21 for the radial case), while the transition is smoother for the (1;+1) case. The data shows a smooth transition, hence the (1;+1) mode is clearly the best solution. However, considering the uncertainty inherent to any measurement, it could be impossible to reproduce a

very sharp transition of phase between the left and right parts of the line profile in a real data set. Hence the FPF method would prefer a (1;+1) mode over a radial mode in the case of any star with a clear radial mode.

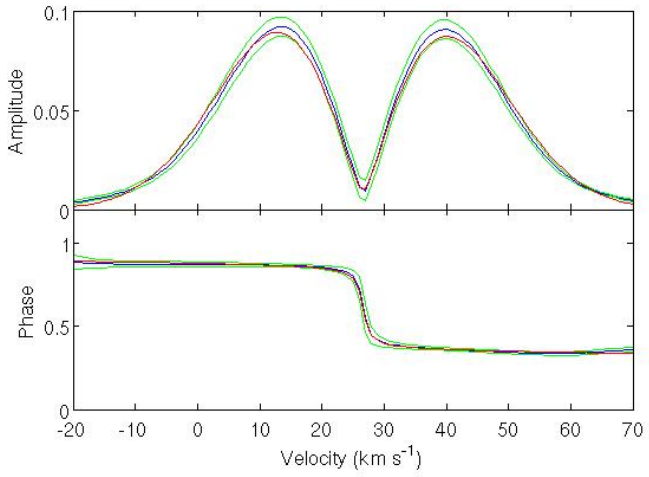

Figure 4.20: Best fit to the primary pulsation of PT Pup. Two Fourier parameters are fitted: (top) the amplitude variation (normalized intensity) and (bottom) the phase across the profile. The data is in blue, closely surrounded by its uncertainty in green. The red curves are the fit. This fit is obtained with a (1;+1) mode.

In order to get a better idea about the spectroscopic observational differences between a radial and a (1;+1) mode, a synthetic set of observations was produced for both cases with the same sampling as the real data set. These are then presented by subtracting the mean from all observations and phasing them on the primary frequency (Figure 4.22). The differences are not clear, which explains the confusion about the exact determination of the pulsational mode. The result of Heynderickx et al. (1994) is clearly in favor of a radial mode for this pulsation. This agrees with the current analysis and the suggestion that modes with $m = 0$ are underestimated in the FPF method due to their sharp transition in the phase across the profile.

The fit to the primary pulsation gives information about the properties of the star. It shows that the central point of the amplitude variations, and therefore of the spectral line, is situated at a radial velocity of 26.4 ± 0.4 km.s^{-1}. The best estimate for $v \sin i$ is 3 ± 3 km.s^{-1}. Figure 4.23 shows the information given about i depending on the chosen mode. Unfortunately a radial mode cannot give us any information on the inclination

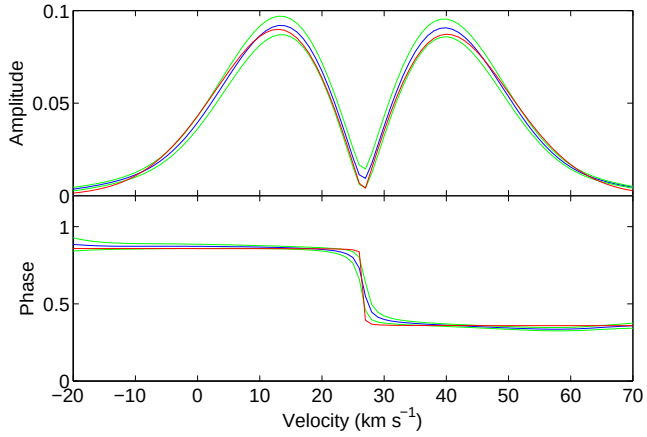

Figure 4.21: Second best fit to the primary pulsation of PT Pup. Two Fourier parameters are fitted: (top) the amplitude variation (normalized intensity) and (bottom) the phase across the profile. The data is in blue, closely surrounded by its uncertainty in green. The red curves are the fit. This fit corresponds to a radial mode: $\ell = 0$ and $m = 0$. The sharp transition in the fit of the phase does not perfectly match the data.

angle i because it affects all the surface of the star in the same way at the same time. Thus a radial mode will have the same effects on observations from any angle.

The best fit for the secondary pulsation is also a (1;+1) mode, this time with a χ^2 value of 0.23 (Figure 4.24). Five other modes were also tested, all almost equally valid for this pulsation: (2;+1) at a χ^2 of 0.23, (2;+2) at 0.24, (2;0) at 0.56, the radial mode at 0.58 and finally (1;0) at 0.59. The radial mode and the two tesseral modes are tested because, as seen for the primary frequency, their sharp transition in the phase is the only way in which they are inferior to the other fits. We doubt that realistic data sets could reproduce this sharp transition, as it means that all the surface elements behave perfectly according to the pulsation. No other dynamics are taken into account in the models, such as coronal mass ejection. These modes should therefore be considered as valid propositions. These two groups of modes are considered separately.

For the case of $m \geq 1$, $\ell = 1$ is a better fit than $\ell = 2$. When $m = 0$ then $\ell = 2$ becomes the best fit. It is interesting to note that Heynderickx et al. (1994) had a large uncertainty when identifying ℓ for this pulsation but concluded that it was $\ell = 2$.

The χ^2 values for the mode identification of the secondary pulsation appear lower than for the primary pulsation only because the uncertainties in the data are greater.

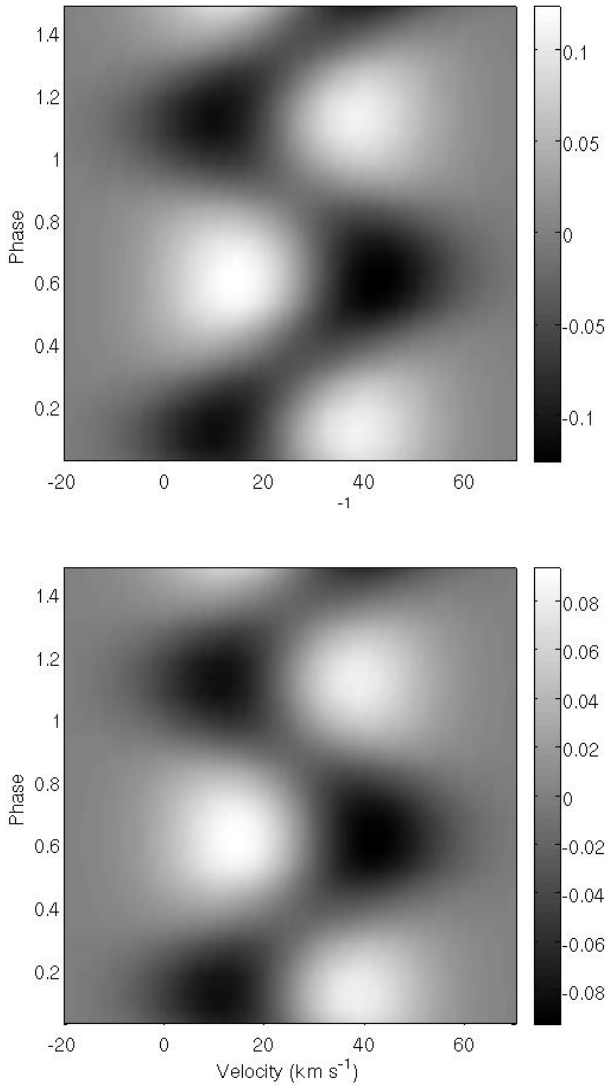

Figure 4.22: Synthetic LPV produced using (top) a (1;+1) mode and (bottom) a radial mode.

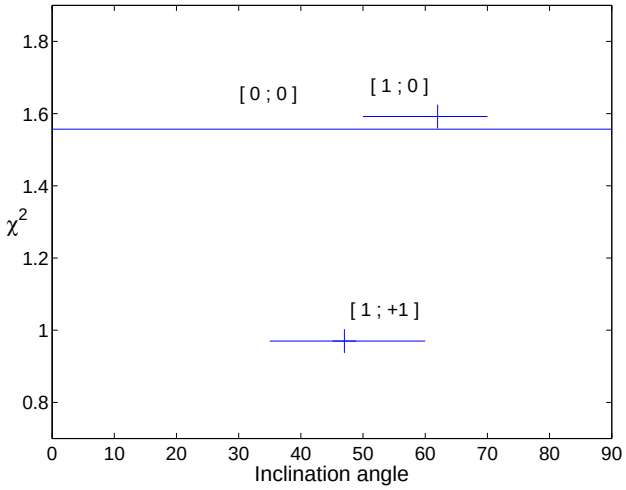

Figure 4.23: χ^2 plot of the inclination angle i for three different modes of pulsation for the primary pulsation of PT Pup. Only the most likely modes are displayed. The horizontal lines represent the range of probable values of i and the small vertical lines indicate its most likely value. The value of ℓ and m are in square brackets above each of their corresponding χ^2 information. We can see that the radial mode is equally valid for all inclinations.

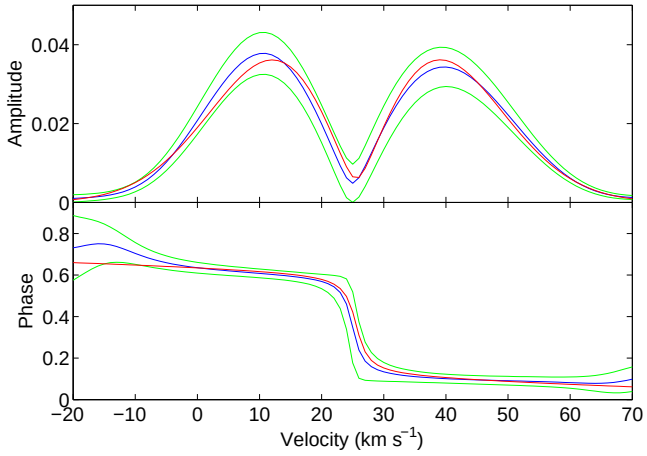

Figure 4.24: Best fit to the Fourier parameters of the secondary pulsation of PT Pup. The amplitude (normalized intensity) (top) and the phase (bottom) across the profile are very well fitted by a (1;+1) mode. The data is in blue, closely surrounded by its uncertainty in green. The red curves are the fit. We can note the larger uncertainties compared with the Fourier parameters of the primary pulsation in Figure 4.20

The signal is much weaker for the secondary pulsation, yielding larger uncertainties and thus more modes could fit the data. The v sin i derived with this fit agrees well with the one obtained from the fit to the primary frequency within uncertainties: $v \sin i = 4 \pm 4$ km.s^{-1}. The radial velocity differs slightly (0.8 km.s^{-1}) at a lower velocity of 25.6 km.s^{-1}. This is why both frequencies could not have been fitted together. The signal to noise ratio is very good, and since the primary pulsation largely dominates the secondary, all fits to the secondary would have been centered around 26.4 km.s^{-1} therefore significantly increasing the χ^2 values of the best fits. The reason for that radial velocity shift between the two pulsations is unknown. The information obtained about the inclination angle i can be seen in Figure 4.25. If the secondary pulsation corresponds to a (1;+1) mode then 40 $\leq i \leq$ 65. However if it is a (2;0) mode then 33 $\leq i \leq$ 43.

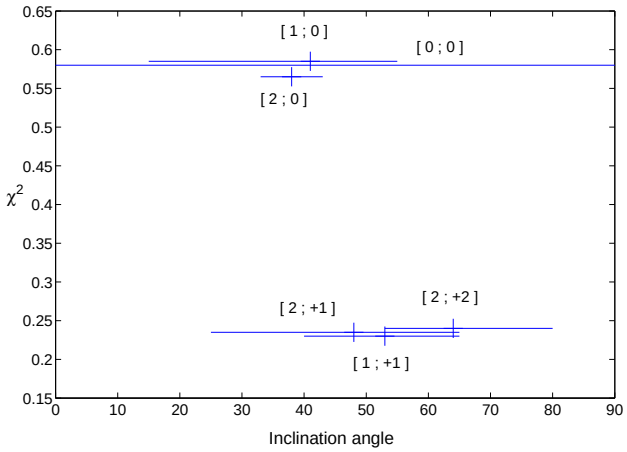

Figure 4.25: χ^2 plot of the inclination angle for six different modes of pulsation for the secondary pulsation of PT Pup. The horizontal lines represent the range of probable values of i and the small vertical lines indicate its most likely value. The value of ℓ and m are in square brackets above each of their corresponding χ^2 information. Note that these χ^2 values cannot be directly compared with those in Figure 4.23 (see text for details).

4.5 Summary

Many methods have been used for the frequency analysis of the PT Pup data and have identified two frequencies. A clear primary frequency at $f_1 = 6.0743 \pm 0.0001$ d^{-1}

and a lower amplitude secondary frequency at $f_2 = 5.9938 \pm 0.0002$ d^{-1}. These were derived from the analysis of the radial velocity variations in the Si III line at 4552 Å. Other methods were used on Si III and also on other single lines or cross-correlated profiles. All analysis gave very similar results. Both frequencies can be linked to the ones found by Heynderickx (1992), although it seems that their relative amplitudes have been inverted as their primary frequency corresponds to our secondary, and their secondary to our primary: 6.01016 ± 0.00001 d^{-1} and 6.06352 ± 0.00002 d^{-1}.

The mode identification of the primary pulsation yields a (1;+1) mode as the most probable mode of pulsation, but the radial (0;0) mode is also possible. The radial mode is also identified by Heynderickx et al. (1994) using photometry. This makes it our preferred solution. There are two possible modes for the secondary pulsation: (1;+1) and (2;0). Heynderickx et al. (1994) identifies this as a $\ell = 2$ mode of pulsation. However his result is uncertain and not sufficient for the (1;+1) mode to be ruled out. A confident determination of this mode would give a good indication of the inclination angle i for PT Pup.

We can now investigate the variability of the amplitude of pulsations by comparing our results with Heynderickx (1992) in the light of the work done by Cugier et al. (1994). The amplitudes of pulsation found through radial velocity are 4.38 km.s^{-1} for f_1 and 1.88 km.s^{-1} for f_2. From Figures 22 and 24 of Heynderickx (1992), we approximate the photometric amplitudes to 0.0009 mag for f_1 and 0.009 mag for f_2. The ratios are:

$$f_1 : \frac{4.38}{0.0009} = 4867$$

$$f_2 : \frac{1.88}{0.009} = 209$$

$$\frac{ratio_1}{ratio_2} = \frac{4867}{209} \approx 23.3$$

If we take $\ell = 0$ for f_1 and $\ell = 2$ for f_2, Figure 6 of Cugier et al. (1994) tells us that the ratio of the amplitudes for f_1 over the amplitudes for f_2 should be approximately

$$\frac{ratio_1}{ratio_2} \approx \frac{1500}{200} = 7.5$$

So the method of analysis and the value of the degree ℓ can account for a large variation of amplitudes which partially explains the discrepancy between our results and the results of Heynderickx (1992). But a factor of at least 3 is still unaccounted for. A more in depth analysis of this phenomenon might explain it, but it seems that

intrinsic variations in the amplitudes of one or both pulsations happened between 1994 and today. The amplitude of f_1 has increased and/or the amplitude of f_2 has decreased.

Chapter 5

HD 189631

HD 189631, also known as HIP 98689, is a southern hemisphere winter object (RA: 20 02 41; DEC: -41 25 04; epoch = 2000). Before this thesis, it had not been extensively observed. The first frequency analysis was done by Handler (1999) from HIPPARCOS data, while its γ Doradus nature was later confirmed by Handler and Shobbrook (2002).

5.1 Observations

We obtained 422 spectra for this star from three different sites. Figure 5.1 is the histogram showing all the observing sessions of HD 189631. More than 300 spectra were taken within the first week, a group of 48 observations were taken one year later. Details of the observing campaign are shown on Table 5.1.

Table 5.1: Observing log for HD 189631.

Instrument	Observer	Start date	Length of run	Number of spectra
HARPS	P. de Cat	July 2^{nd} 2008	7 nights	273
HERCULES	P. Kilmartin	July 2^{nd} 2008	9 nights	38
HERCULES	K. Pollard	August 5^{th} 2008	5 nights	7
FEROS	L. Mantegazza	July 12^{th} 2008	8 nights	56
HARPS	E. Poretti	June 22^{nd} 2009	10 nights	23
HARPS	J.C. Suárez	July 17^{th} 2009	4 nights	25

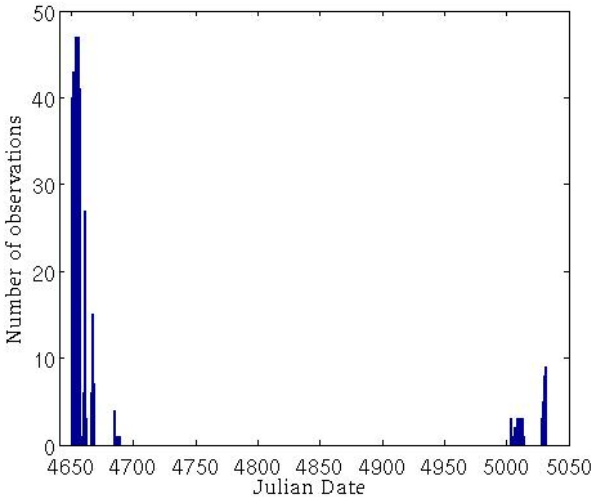

Figure 5.1: The complete data set of HD 189631 is represented on this histogram.. The dates shown are JD-2450000.

5.2 Properties

No extensive spectroscopic observations of this star have been published. Perryman and ESA (1997) note a spectral type of A9 V.

5.2.1 Line profile variation

A few observations are necessary to show without a doubt that HD 189631 exhibits strong variations in its spectral line profile. Figure 5.2 is illustrating this by showing the cross correlated profile of the first 25 observations. Unlike PT Pup, the shape of this line profile is strongly affected while the radial velocity does not seem to vary. This is a good indicator of a g-mode pulsating star since it excludes a dominant radial mode of pulsation for HD 189631. Pulsation modes with $\ell \geq 1$ are expected.

5.2.2 v sin i

From our data we find v sin $i = 43.6 \pm 0.5$ km.s^{-1}. As described in Chapter 3 we used two methods to determine v sin i. A least-squares fit of our data by a broadened Gaussian profile yields v sin $i = 43.8 \pm 0.6$ km.s^{-1} (Figure 5.3) while comparing the Fourier transforms of our data and of a Gaussian broadened to v sin $i = 20$ km.s^{-1} gives v sin $i = 43.5 \pm 0.5$ km.s^{-1} (Figure 5.4).

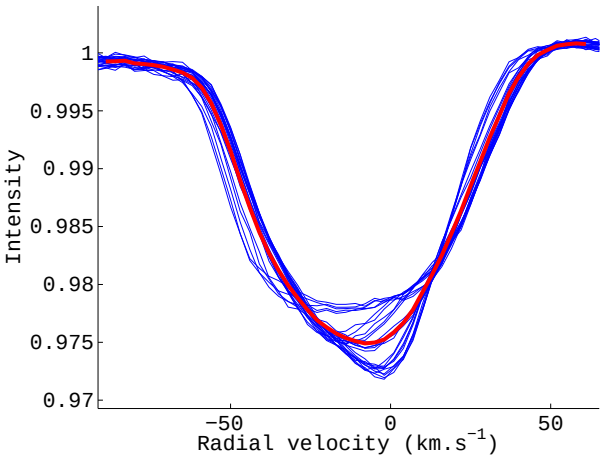

Figure 5.2: Variations of the cross correlated profile of HD 189631. The first 25 observations are displayed in blue while their mean is shown by the thick red line.

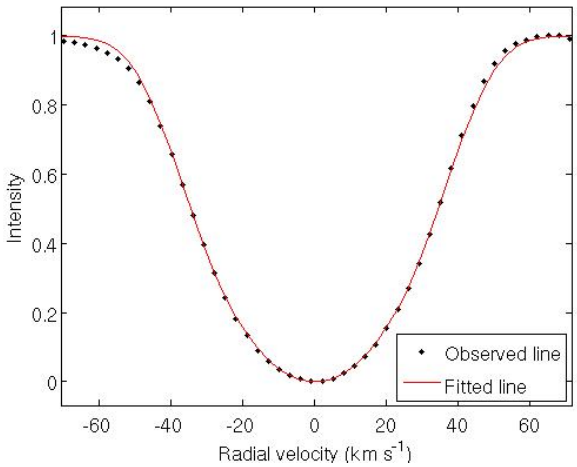

Figure 5.3: Measuring v sin i with the Gaussian method for HD 189631. The v sin i determination by fitting a broadened Gaussian to the mean spectral line of HD 189631. This yields v sin $i = 43.78 \pm 0.6$ km.s^{-1}.

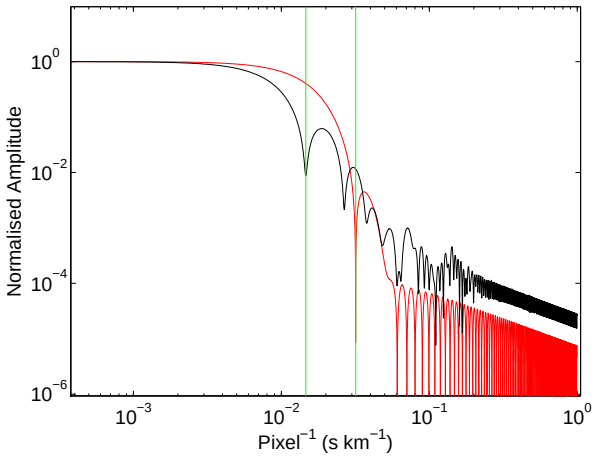

Figure 5.4: Measuring v sin i with the Fourier minima method for HD 189631. A log-log plot of the Fourier transform of the mean of our observations of HD 189631 (solid line) is compared with a Gaussian broadened to v sin $i = 20$ km.s^{-1} (dashed line). The vertical lines indicate the positions of the first minima. The ratio of the first minima along the abscissa (multiplied by 20 km.s^{-1}) gives v sin $i = 43.48 \pm 0.5$ km.s^{-1}.

5.2.3 Radial velocity

Only two measurements of the radial velocity of HD 189631 have been published. Duflot et al. (1995) listed -6.9 km.s^{-1} while Gontcharov (2006) gave -6.9 ± 4.5 km.s^{-1}. Using the bisector method and recording the value at 50% of the line depth we obtain -10.13 km.s^{-1} from the average of our 422 cross-correlated spectra. Figure 5.5 and Table 5.2 show that there is a very small asymmetry, concentrated in the upper part of the spectral line.

Summary Table 5.3 lists the results of these two methods on our individual observations, as well as the results of the radial velocity determination. Note that the values of the minima and maxima are not outliers. The large standard deviations are expected in a pulsating star.

5.3 Frequency analysis

In order to analyze properly our Fourier frequency graphs, we need to take a look at the spectral window, displayed on Figure 5.6. A spectral window is showing which aliasing

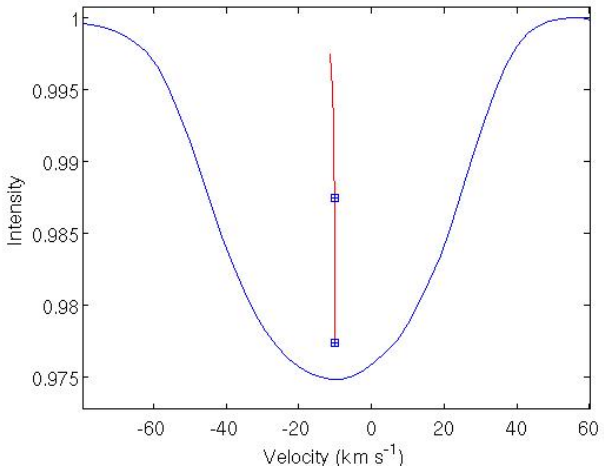

Figure 5.5: Radial velocity determination for HD 189631. The spectral line is the mean of 422 cross correlated observations, the central line is its bisector. The two symbols are situated at 50% and 90% of the line depth.

Table 5.2: Radial velocity of HD 189631 - Radial velocity measured at different depths of the mean spectral line for HD 189631.

Line depth (in %)	Velocity (km.s^{-1})
20	-10.70
30	-10.46
40	-10.26
50	-10.13
60	-10.04
70	-10.10
80	-10.18
90	-10.18

Table 5.3: RV and v sin i results for HD 189631. Various results from our detailed analysis of the radial velocity (RV) and v sin i, the latter either using the broadened Gaussian method ($(v \sin i)_G$) or the Fourier minima method ($(v \sin i)_F$). The first row (mean line) shows our result using the mean of our 422 cross correlated observations. The other rows refer to the analysis of the 422 individual observations. We chose a 50% line depth for our radial velocity measurements.

	RV	$(v \sin i)_G$	$(v \sin i)_F$
	km.s^{-1}	km.s^{-1}	km.s^{-1}
mean line	-10.13	43.78	43.48
individual average	-10.17	43.48	43.74
min	-15.13	35.60	36.65
max	-6.57	51.25	51.83
standard deviation (σ)	1.66	3.14	3.18

peaks will be enhanced due to our sampling. In the case of HD 189631 the data set is large therefore the noise is low. The one day aliases are not extremely high due to the fact that it was observed in Chile and New Zealand in the same period.

In the following subsections the frequencies are identified using different methods and therefore they are not necessarily found in the same order or identified by every method of analysis. We however keep a constant notation for each frequency. To avoid confusion, remember that for instance f_5 can appear before f_1 (in the equivalent width analysis). The way to order them appears clear once we have the result from every methods.

5.3.1 Photometric frequency analysis

Handler (1999) analyzed the photometric data of HD 189631 from HIPPARCOS, finding one frequency at 1.67 d^{-1} and noting a weak, complicated signal. Later, Handler and Shobbrook (2002) confirmed it as a γ Doradus target and noted the absence of δ Scuti-type pulsations.

5.3.2 Equivalent width frequency analysis

A Fourier analysis of the equivalent width variations identifies three frequencies: $f_5 = 0.9787$ d^{-1}, $f_1 = 1.6718$ d^{-1} and $f_2 = 1.4511$ d^{-1}(see Figure 5.7). f_1 matches the single photometric result from Handler (1999). It seems that the pulsational mode

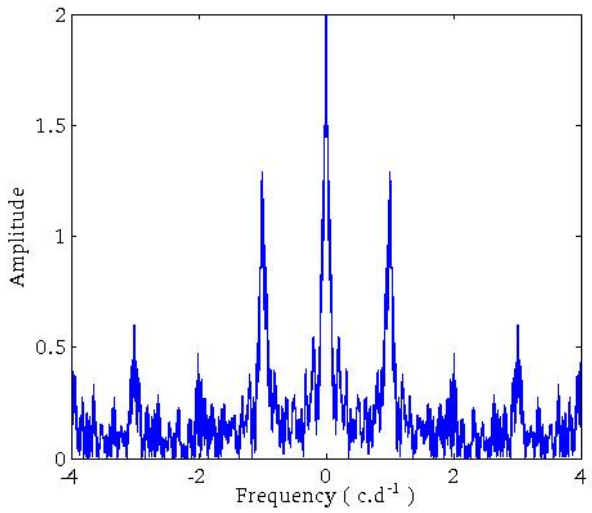

Figure 5.6: The spectral window shows the expected aliasing pattern due to our data sampling.

which oscillate at these frequencies is weakly affecting the equivalent width of the spectral lines as the amplitude of pulsations are less than 1% of the mean equivalent width: 1.71 km.s^{-1}. Furthermore fitting the frequencies to the data only accounts for 17.95% (f_5), 27.64% (f_5 and f_1) and 39.63% (f_5, f_1 and f_2) of the observed variations.

Since the equivalent width is lightly affected by the pulsations the uncertainty is higher with this method than with the other methods. This can be seen on Figure 5.8 which shows the data taken during seven consecutive clear nights with a fit produced using the three identified frequencies.

5.3.3 Radial velocity frequency analysis

The first moment analysis (radial velocity variations) shows four frequencies: f_1 = 1.6772 d^{-1}, f_2 = 1.4200 d^{-1}, f_4 = 1.8227 d^{-1} and f_3 = 0.0711 d^{-1} (see Figure 5.9). The first frequency was identified in the Hipparcos photometry. The first and second frequencies were also found in our equivalent width analysis (Section 5.3.2). The last two frequencies have never been identified before. Fitting f_1 to the data explains 33.07% of the variations of radial velocity observed. Including f_2 accounts for 56.54% , adding f_4 we get to 67.25% and all four frequencies together explain 78.25% of the observed variations.

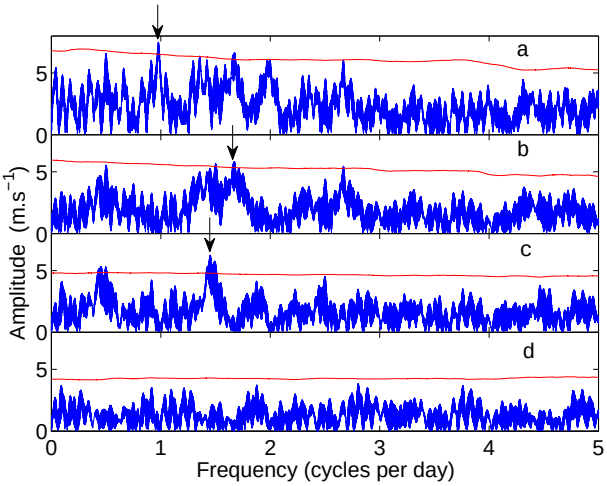

Figure 5.7: Fourier analysis for HD 189631 of the variation in equivalent widths. (a) identifies $f_5 = 0.9787$ d^{-1} as the main frequency with an amplitude of 0.0075 km.s^{-1}. After prewhitening the data we find (b) $f_1 = 1.6718$ d^{-1} at an amplitude of 0.0058 km.s^{-1}, and finally (c) $f_2 = 1.4511$ d^{-1} at an amplitude of 0.0062 km.s^{-1}. The eventual remaining frequencies are hidden by the noise. Our detection limit is shown by the solid red line.

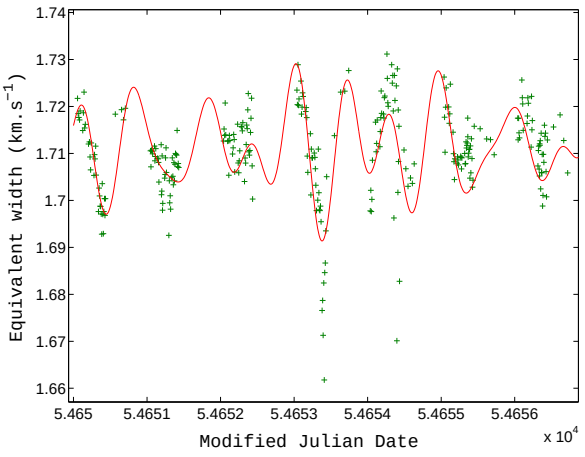

Figure 5.8: Equivalent width variations of HD 189631 fitted with three frequencies. The equivalent width of 303 cross-correlated line profiles within seven consecutive nights at ESO la Silla, using HARPS and FEROS, is fitted by a solid line using f_5, f_1 and f_2.

The choice of f_3 is a difficult one to make as the highest peak is at 0.0711 d^{-1}. The noise floor, from drift noise, increases when approaching low frequencies. An alias can thus be artificially enhanced by this noise when approaching zero, so f_3 could be an alias of a frequency at 1.07 d^{-1}.

Figure 5.10 is showing the data taken during seven consecutive clear nights fitted by our four frequencies. The radial velocity variations are clear and the signal-to-noise ratio is good. We also show the residuals on the lower panel of Figure 5.10, where we can see that some sinusoidal pattern seems to be present. The chosen threshold of 15 in spectral significance prevents us from identifying more frequencies, but by being less restrictive we could certainly find a few more. However, these frequencies have a low signal therefore further mode identification would be very uncertain. A combined mode identification taking into account too many pulsational frequencies would corrupt the information derived by using only the dominant pulsations. We decided to be consistent through all of our frequency analysis and not report frequencies below the threshold of 15.

5.3.4 Pixel-by-pixel frequency analysis

In the pixel-by-pixel method, the normalized intensity variation of every single pixel in the line profile is analyzed as a time series and a Fourier spectrum produced for each. An average of these Fourier spectra is then taken. Once again the main frequency is clearly identified, this time by using the Pixel-by-Pixel method (Figure 5.11): $f_1 = 1.6797$ d^{-1}. For the second frequency (Figure 5.12) we also find $f_2 = 1.4149$ d^{-1}. The third frequency (Figure 5.13) is found at $f_3 = 0.0739$ d^{-1}, while the fourth (Figure 5.14) is at $f_4 = 1.8228$ d^{-1}. Because there is some debate on a possible alias of f_3, we have prewhitened our data by a least-square fit to f_1, f_2 and f_4 and phase it on f_3 and the possible alias at 1.07 d^{-1} (Figure 5.15). f_3 seems to correspond to a more regular pulsation than its alias.

On the left panel of Figure 5.16 we show the line profile variations after subtracting the mean line profile from all observations. Using the pixel-by-pixel method we can fit a different pulsational amplitude to each pixel independently. It also recognizes that all pixels are not pulsating in phase, therefore computing a phase across the profile which represents the phase shift between different parts of the line profile. The amplitude and phase across the profile derived from this data for each of the four frequencies can

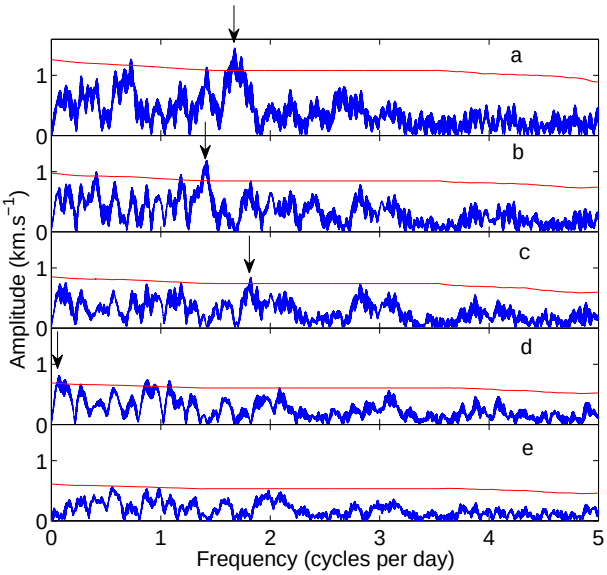

Figure 5.9: Fourier analysis for HD 189631 of the variation in radial velocity. (a) identifies $f_1 = 1.6772$ d^{-1} as the main frequency with an amplitude of 1.45 km.s^{-1}. After prewhitening the data we find (b) $f_2 = 1.4200$ d^{-1} with an amplitude of 1.19 km.s^{-1}, then (c) $f_4 = 1.8227$ d^{-1} with an amplitude of 0.84 km.s^{-1}, (d) $f_3 = 0.0711$ d^{-1} with an amplitude of 0.82 km.s^{-1}. (e) shows the noise floor. Our detection limit is shown by the solid red line.

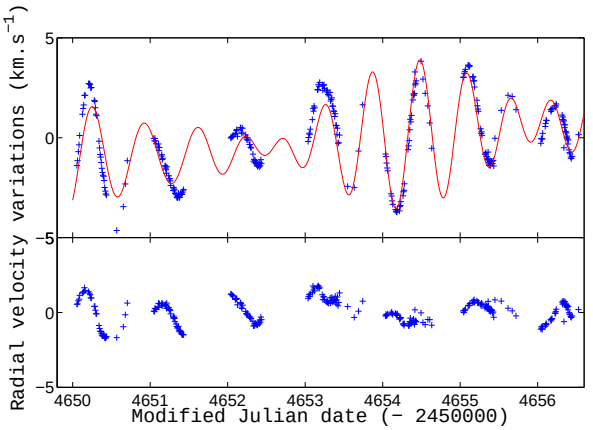

Figure 5.10: Top: The radial velocity of 303 cross-correlated line profiles of HD 189631 observed within seven consecutive nights. The fitted curve is done using the four identified frequencies. Below: Residuals after removing the effects of the four frequencies.

be used to produce a fit shown on the right panel of Figure 5.16. This synthetic data is using the dates of each observations in order to reproduce the data sampling. The data is phased on the first identified frequency: $f_1 = 1.6797$ d^{-1}. This fit accounts for 69.5% of the variations observed in our data set. f_1 alone is responsible for 27.0%, f_1 and f_2 account for 44.7% while f_1, f_2 and f_3 account for 53.4% of the intensity variations.

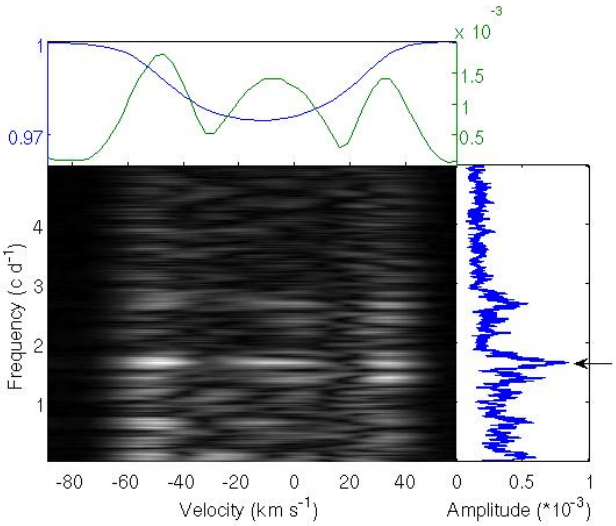

Figure 5.11: Fourier analysis for HD 189631 using the pixel-by-pixel method - f_1. The top panel shows the mean spectral line along with the amplitude variations at $f_1 = 1.6797$ d^{-1}. The central panel shows the 2D frequency analysis done on each pixel of the profile. The right panel shows an average across the profile. We identify f_1 as the main frequency, indicated by an arrow.

5.3.5 Investigating the asymmetry of the line profile

We analyzed the asymmetry of the line profile in the way described in subsection 3.3.4. We can confirm the results of the previous sections: $f_3 = 0.0739$ d^{-1}, $f_1 = 1.6822$ d^{-1}, $f_4 = 1.8198$ d^{-1} and , $f_2 = 1.4226$ d^{-1} (Figure 5.17). In this case f_3 is responsible for 20.03% of the observed variations, f_3 and f_1 together contribute for 33.86%, f_3, f_1 and f_4 combined account for 46.77%, and combining all four frequencies explains 59.50% of the variations. The mean LPAP is equal to -0.60 km.s^{-1} which shows that HD 189631 does not exhibit a strong asymmetry in its line profile unlike AC Lep (see Chapter 6).

In Figure 5.18 we show the data taken during seven consecutive clear nights fitted by our four frequencies.

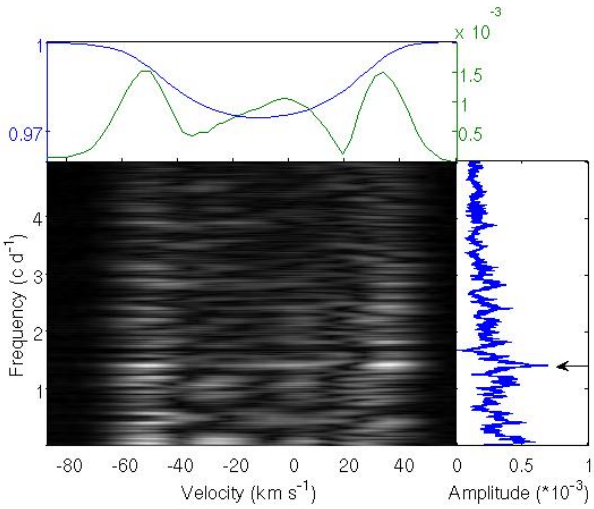

Figure 5.12: Fourier analysis for HD 189631 using the pixel-by-pixel method - f_2. After prewhitening the data we find a second frequency at 1.4149 d^{-1}.

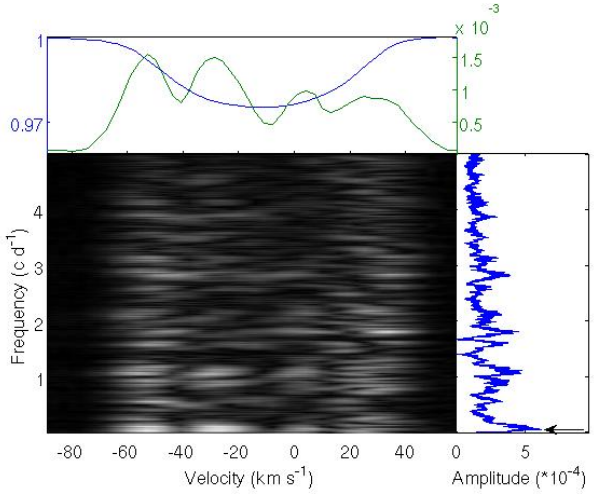

Figure 5.13: Fourier analysis for HD 189631 using the pixel-by-pixel method - f_3. After prewhitening the data with f_1 and f_2 we find the third frequency at 0.0739 d^{-1}.

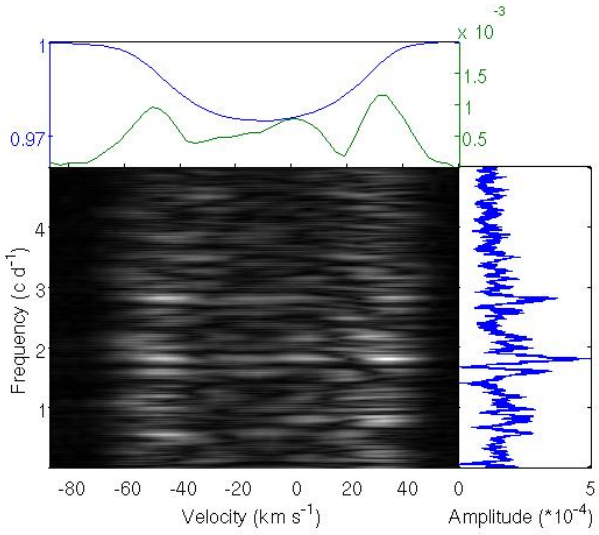

Figure 5.14: Fourier analysis for HD 189631 using the pixel-by-pixel method - f_4. After removing the first three frequencies we find the fourth frequency at 1.8228 d^{-1}.

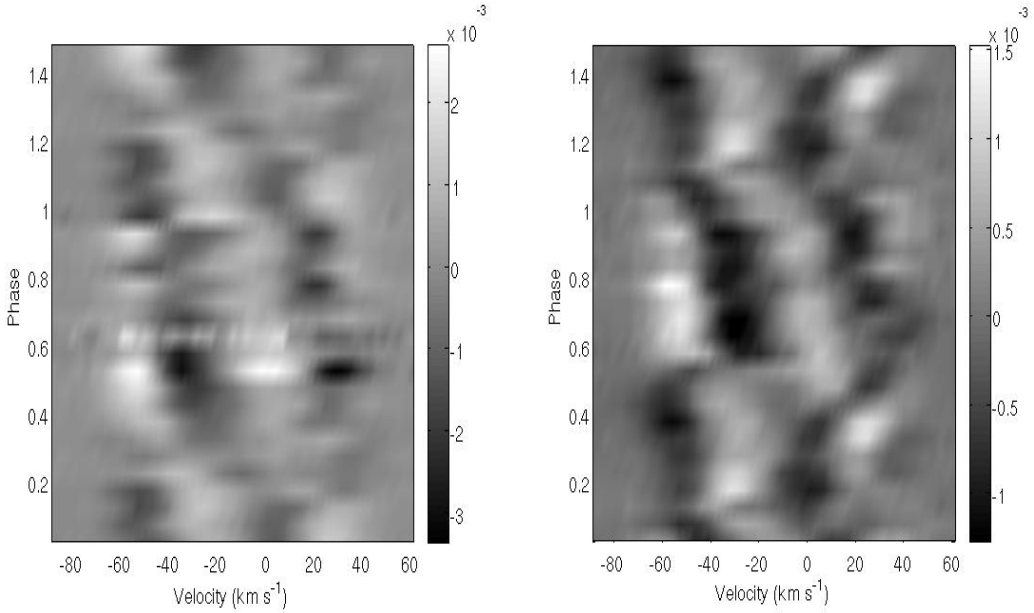

Figure 5.15: Looking for the third frequency. Line profile variations observed in HD 189631 after removing the effects of f_1, f_2 and f_4. The left panel is phased on $f_3 = 0.0739$ d^{-1} while the right panel is phased on 1.0700 d^{-1}. The average line profile has been subtracted from all observations.

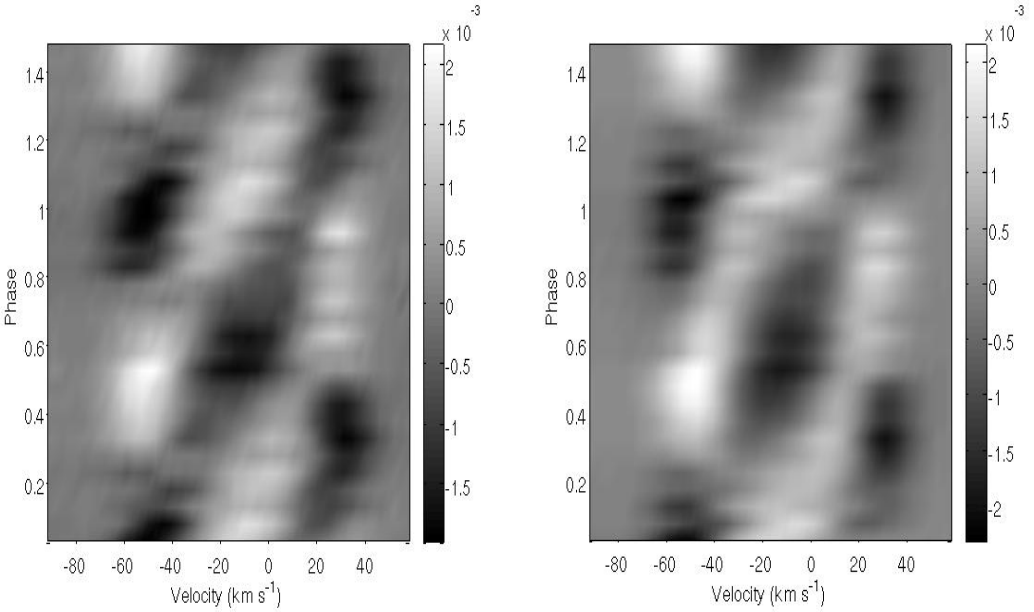

Figure 5.16: LPVs of HD 189631 fitted. Left panel: Line profile variation observed in HD 189631 phased on $f_1 = 1.6797$ d^{-1}. Right panel: A least-squares fit to the data is done with the independent pixel amplitude variations and phase across the profile derived for the four frequencies. It is also phased on f_1. The average line profile has been subtracted from all observations on each panel.

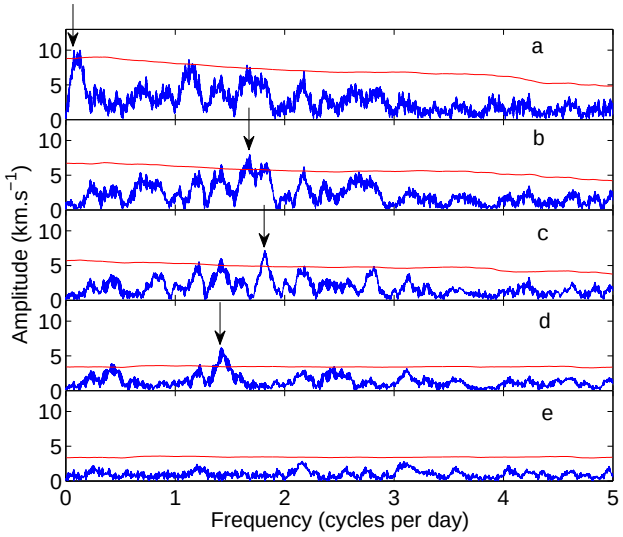

Figure 5.17: Fourier analysis of the LPAP data set of HD 189631. (a) identifies $f_3 = 0.0739$ d^{-1} with an amplitude of 9.94 km.s^{-1}. For every other panel we prewhiten the data with the previously identified frequencies. In (b) we find $f_1 = 1.6822$ d^{-1} at an amplitude of 7.97 km.s^{-1}, in (c) we find $f_4 = 1.8198$ d^{-1} at an amplitude of 7.18 km.s^{-1}, finally in (d) we see $f_2 = 1.4226$ d^{-1} with an amplitude of 6.15 km.s^{-1}. (e) shows the noise floor. Our detection limit is shown by the solid red line.

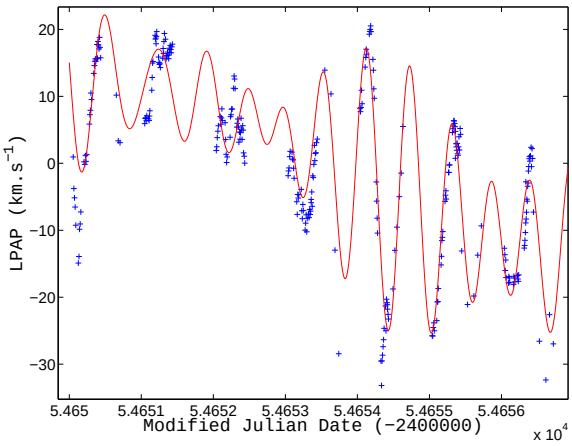

Figure 5.18: . The LPAP of 303 cross-correlated line profiles taken during seven consecutive clear nights fitted with a solid line produced by a combination of f_1, f_2, f_3 and f_4.

Table 5.4: Summary of the frequency analysis of the HD 189631 pulsations. The amplitudes should only be compared within a column because they scale differently depending on which method was used and the units are different: Equivalent width (EW), radial velocity (RV) and LPAP amplitudes are in km.s^{-1}, pixel-by-pixel (PbP) amplitudes are in normalized intensity $*10^{-3}$, and photometric amplitudes are in units of mmag. The bottom part of the table shows the fraction of the variation explained by fitting the frequencies to the data.

f	EW	RV	PbP	LPAP	Phot. [a]
d^{-1}	m.s^{-1}	km.s^{-1}	$*10^{-3}$	km.s^{-1}	mmag
f_1	1.67 (5.8)	1.68 (1.45)	1.68 (0.85)	1.68 (7.97)	1.67
f_2	1.45 (6.2)	1.42 (1.19)	1.41 (0.69)	1.42 (6.15)	
f_3		0.07 (0.82)	0.07 (0.61)	0.07 (9.94)	
f_4		1.82 (0.84)	1.82 (0.50)	1.82 (7.18)	
f_5	0.98 (7.5)				
one f	18% (f_5)	33% (f_1)	27% (f_1)	20% (f_3)	
two f	28% ($f_5 + f_1$)	57% ($f_1 + f_2$)	45% ($f_1 + f_2$)	34% ($f_3 + f_1$)	
three f	40% ($f_5 + f_1 + f_2$)	67% ($f_1 + f_2 + f_4$)	53% ($f_1 + f_2 + f_3$)	47% ($f_3 + f_1 + f_4$)	
four f		78% ($f_1+f_2+f_4+f_3$)	70% ($f_1+f_2+f_3+f_4$)	59% ($f_3+f_1+f_4+f_2$)	

[a]Handler (1999)

5.3.6 Summary of frequencies

Five frequencies were found, $f_1 = 1.6719 \pm 0.0005$ and $f_2 = 1.4200 \pm 0.0005$ being found with every method of analysis. Aliasing patterns make the identification of $f_3 = 0.0711 \pm 0.0005$ difficult. We have more confidence on the identification of $f_4 = 1.8227 \pm 0.0005$. Only f_1 was confirmed by previous photometric observations. The summary of our analysis is shown in Table 5.4. The frequencies and their associated uncertainties listed here are the ones found within the radial velocity variations as this method is the one giving us the lowest uncertainties.

Having a look at the sampling of these frequencies by our data set can give us confidence on their accurate determinations. Figure 5.19 is showing four histograms corresponding to each frequency. The sampling of f_1 and f_2 is very good. For f_4 it is slightly inferior but still good. However for f_3, as expected in the case of a frequency approaching 0, the sampling is not satisfactory. More data would solve this issue.

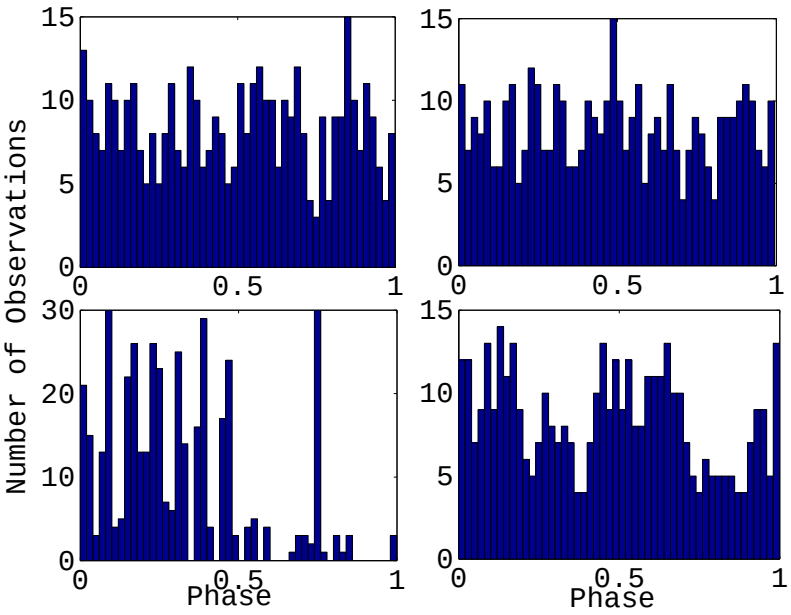

Figure 5.19: Frequencies of HD 189631 sampled by our data set. (top-left) shows the sampling of f_1, (top-right) is for f_2, (bottom-left) for f_3 and (bottom-right) for f_4.

5.4 Mode identification

As in section 4.4 we need to give a set of parameters for all mode identifications. Most of them are estimated for HD 189631 because none of these parameters have been evaluated in publications. The estimations are based on its spectral type: A9 V. The first set of parameters are not allowed to vary because we need to limit the parameter space in order to have the algorithm functioning at its best. It does not affect our results since these parameters have negligible effects on the mode identification. The equivalent width is an exception as it is critical in the identification of the modes, but its determination is very precise so we already know what the result will be if we let it vary. This was confirmed by simulations with smaller parameter space but a free equivalent width.

- R= 1.6 $R_\odot$
- M= 1.5 $M_\odot$
- T_{eff} = 7500 K

- $\log g = 4.20$
- $[Fe/H] = 0.08$
- Equivalent width= 1.72 km.s^{-1}

The following parameters, specific to the mean line profile, will vary in order to improve the fit:

- $v \sin i$ from 42 to 45 km.s^{-1}
- i from 5^o to 90^o
- Intrinsic width from 7 to 13 km.s^{-1}
- Zero-point shift (i.e. the radial velocity) from -13 to -7 km.s^{-1}

Finally we explore a large parameter space for the pulsational mode characteristics for each frequency:

- l from 0 to 5
- m from $-l$ to $+l$
- Amplitude from 0.1 to 20 km.s^{-1}
- Complete range for the phase from 0 to 2π

5.4.1 Independent mode identifications

In order to reduce the total parameter space we begin by performing mode identifications on each frequency independently. The primary pulsation is best fitted by a mode with (1 ; +1) with $\chi^2 = 59$, the second best fit is obtained by an (1 ; -1) with $\chi^2 = 80$. Both fits depend on the inclination angle i.

The mode identification of the secondary pulsation has many solutions. Most of these are very dependent on i and solutions are found mostly around the maximum, $i = 90^o$, and minimum, $i = 7^o$, where the equatorial velocity would reach a critical value. We note here two possibilities: First, (2 ; -2) with $\chi^2 = 42$ is a good fit in both low ($i = 12^o$) and high inclination ($i = 88^o$). This mode fits well the amplitude variations in the wings of the spectral line, but poorly the centre as the data shows one

central maximum where the fit has two. Second, (3 ; −2) with $\chi^2 = 67$ spans a wide range of inclinations centred on $i = 32^o$.

The third pulsation at $f_3 = 0.0711$ d^{-1} lies outside the expected range of frequencies for a γ Doradus star: 0.3 to 3 d^{-1}. This happens if a pulsation has a co-rotating frequency comparable with the rotational frequency of the star in the opposite direction, i.e. a retrograde mode. Thus two conditions apply when investigating the modes of pulsation:

$$m < 0 \tag{5.1}$$

$$|m(1 - C)f_{rot}| + O(f_{rot}^2) > 0.3 - f_3 \tag{5.2}$$

where C is the Ledoux constant describing effects of the Coriolis force (Ledoux, 1951) and the second order term describes effects of the centrifugal force. Only one mode is selected as the fit is largely superior to all other possibilities: (2 ; −2) ; $\chi^2 = 22$. This solution fulfills both conditions for the considered range of v sin i and inclination angle i.

Finally, the fourth pulsation has two possible modes which are very different, but the χ^2 values are comparable: (2 ; −2) with $\chi^2 = 22$ and (4 ; +1) with $\chi^2 = 23$. From this result we can say that it is not justified to assign an individual uncertainty to each of the wavenumbers values as the most likely alternative solutions often have very different values.

Figure 5.20 summarizes the most likely modes along with their dependency on the inclination angle of the star. These independent fits provide us with a different set of parameters (radial velocity, rotational velocity and inclination angle) for each pulsation, so a combined fit is required to achieve consistency of these stellar parameters.

5.4.2 Combined mode identification

A combined mode identification is now performed with a smaller parameter space. Some of the parameters output by the best fits are presented in Table 5.5.

For this data set the 95%-significance limit is situated at $\chi^2 = 67$. The fit for each pulsational frequency are displayed on Figures 5.21, 5.22, 5.23 and 5.24 where both best fits are displayed. We note that in some occasions the phase fitting seems poor.

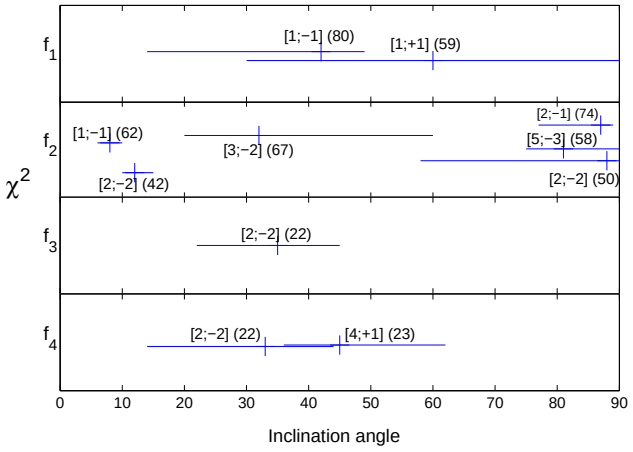

Figure 5.20: χ^2 plot of the inclination angle depending on the different modes of pulsation for HD 189631. Only the most likely modes are displayed. The horizontal lines represent the range of probable values of i and the small vertical lines indicate its most likely value. The value of ℓ and m are in square brackets with their associated χ^2 value to their right.

Table 5.5: Results of a mode identification of HD 189631 for the four identified frequencies. The first four columns correspond to the ℓ and m wavenumbers of the pulsation modes associated with each frequency.

f_1	f_2	f_3	f_4	i	v sin i km.s^{-1}	Radial velocity km.s^{-1}	Intrinsic width km.s^{-1}	χ^2
1;+1	3;-2	2;-2	4;+1	43.6^o	43.7	-9.2	9.6	34
1;+1	3;-2	2;-2	2;-2	38.0^o	43.3	-9.6	10.0	35
1;+1	3;-2	2;-2	1;0	48.2^o	44.3	-9.6	9.7	39
1;+1	3;+1	2;-2	2;-2	41.5^o	44.4	-10.2	10.2	41
1;+1	3;-2	2;-2	3;+1	45.7^o	43.7	-10.0	10.1	41
1;+1	3;+1	2;-2	4;+1	41.3^o	44.1	-10.2	10.9	41
1;+1	3;-2	2;-2	3;-2	46.4^o	43.9	-9.6	10.1	42

In fact if the difference between the data and the fit is an integer they are considered in the same phase of the pulsation, but one cycle apart. Thus the fit is considered good. Overall, a perfect fit is not expected as other modes are present at different frequencies with comparable amplitudes. Again, the centre of the amplitude variations is not quite in agreement with the measured radial velocity from the line profile: -10.15 km.s^{-1} . The value of v sin i is in good agreement and the inclination angle is quite plausible.

We note that the second best fit, obtained with (2 ; −2) for the fourth pulsation, is also a very good candidate with $\chi^2 = 34.73$. In this case $i = 38.0^o$.

The fit to the secondary frequency is not entirely satisfying. Another good candidate for this pulsation is (2 ; −2) with a low χ^2, but this mode has four maxima across its amplitude variation profile (this is clearly visible on Figures 5.23 and 5.24 when fitted to the third and fourth frequencies) whereas the data only shows three (Figure 5.22). By comparing Figures 5.21 & 5.22, we can think that the secondary frequency would be well fitted by a (1 ; +1) mode but this mode was not included in Figure 5.20 as its individual χ^2 was too high (113.65). It was later tested together with the other most likely modes and was still excluded by the statistics: $\chi^2 = 58.01$ which is much higher than 34.33 (most likely mode) and places it outside of the five best fits for this frequency. It is however still below the 95%-significance limit of 67.

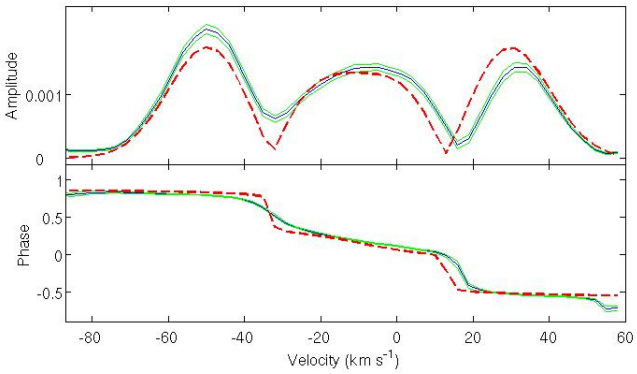

Figure 5.21: First pulsational mode of HD 189631. Fourier parameter of the primary pulsation of HD 189631 fitted by a (1 ; +1) mode. The amplitude is measured in normalized intensity and the phase is dimensionless. The data is surrounded by its uncertainty, the dashed line is the fit.

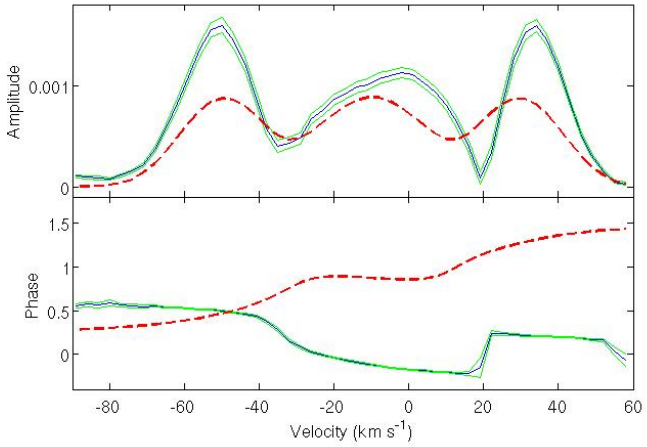

Figure 5.22: Second pulsational mode of HD 189631. Fourier parameter of the second pulsation of HD 189631 fitted by a $(3\ ;\ -2)$ mode.

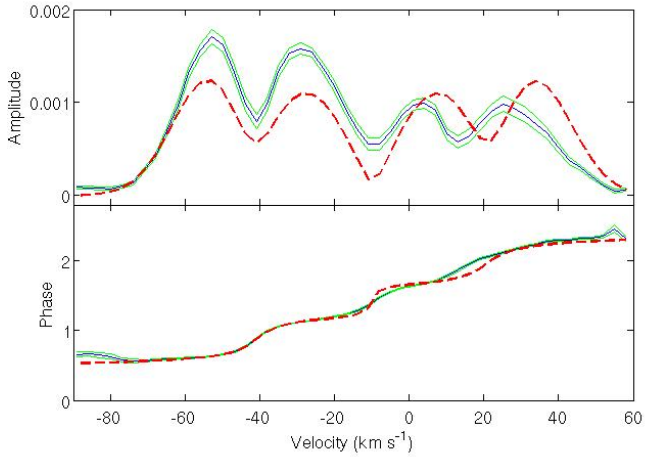

Figure 5.23: Third pulsational mode of HD 189631. Fourier parameter of the third pulsation of HD 189631 fitted by a $(2\ ;\ -2)$ mode.

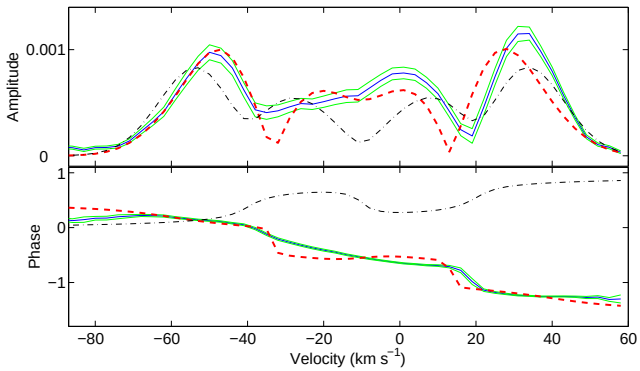

Figure 5.24: Fourth pulsational mode of HD 189631. Fourier parameter of the fourth pulsation of HD 189631 fitted by the best fit: a (4 ; +1) mode (dashed line); and the second best fit: (2 ; −2) (dash-dotted).

5.5 Summary

The analysis of HD 189631 was based on 422 spectra obtained over 13 months from two sites: La Silla in Chile and MJUO in New Zealand. We measured v sin i to be 43.6 ± 0.5 km.s^{-1} and the radial velocity at -10.1 km.s^{-1}.

The frequency analysis allows us to identify four frequencies: $f_1 = 1.6719 \pm 0.0005$ d^{-1}, $f_2 = 1.4200 \pm 0.0005$ d^{-1}, $f_3 = 0.0711 \pm 0.0005$ d^{-1} and $f_4 = 1.8227 \pm 0.0005$ d^{-1}. The only result previously published on this star was by Handler (1999) and confirms $f_1 = 1.67$ d^{-1} from photometry. We have some confidence in the mode identification of the pulsations associated with f_1 (1 ; +1) and f_3 (2 ; −2). We are not satisfied by the fit obtained for f_2 with (3 ; −2) mode, but it is still the best solution. For f_4 we are not able to choose between two modes: (4 ; +1) or (2 ; −2).

Chapter 6

AC Lepus

AC Lepus, also named HR 2118, HIP 28434 or HD 40745, is a southern hemisphere summer object (RA: 06 00 18; DEC: -12 54 00; epoch = 2000). It has been discovered to be a variable star by the HIPPARCOS team (Perryman and ESA, 1997), and later progressively classified as a γ Doradus through several publications (Aerts et al., 1998; Handler, 1999; Kazarovets et al., 2000).

6.1 Observations

We obtained 248 spectra for this star, all taken from MJUO. Figure 6.1 is a histogram showing a complete overview of the observing sessions of AC Lep. We did a first group of observations to collect a few spectra of various potential targets. After selecting this star as a main target, a dedicated observing scheme was designed, but interrupted for a few months because during this period the star was not observable (i.e. in the "day sky"). This is why most of the data was taken the following year. The details are shown on Table 6.1.

6.2 Properties

This star is of spectral type F2 IV (Perryman and ESA, 1997) or F2 V (Abt and Morrell, 1995), with a surface temperature estimated to be 6790 K (Aerts et al., 1998).

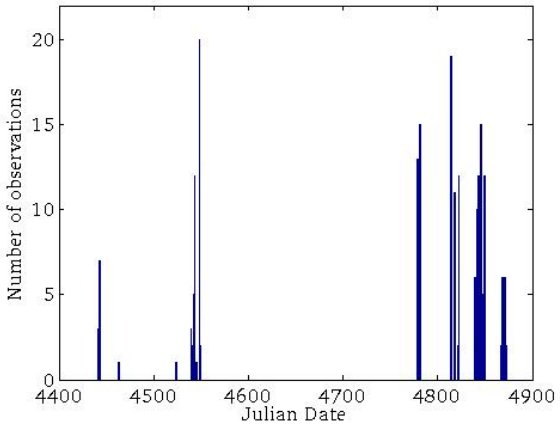

Figure 6.1: The complete data set of AC Lep is represented on this histogram. The dates shown are JD-2450000.

Table 6.1: Observing log for AC Lep.

Instrument	Observer	Start date	JD (-2450000)	Length of run	Number of spectra
HERCULES	F. Maisonneuve	December 7^{th} 2007	4441	3 nights	15
HERCULES	F. Maisonneuve	December 28^{th} 2007	4462	1 night	1
HERCULES	F. Maisonneuve	February 26^{th} 2008	4522	1 night	1
HERCULES	F. Maisonneuve	March 14^{th} 2008	4539	10 nights	47
HERCULES	F. Maisonneuve	November 7^{th} 2008	4777	4 nights	35
HERCULES	P. Kilmartin	December 13^{th} 2008	4813	9 nights	48
HERCULES	F. Maisonneuve	January 7^{th} 2009	4838	11 nights	82
HERCULES	P. Kilmartin	February 5^{th} 2009	4867	6 nights	19

6.2.1 Line profile variation

A few observations are necessary to show without a doubt that AC Lep exhibits strong variations in its spectral line profile. Figure 6.2 is illustrating this by showing the cross correlated profile of the first 25 observations. Unlike PT Pup, and like HD 189631, the shape of this line profile is strongly affected while the radial velocity does not seem to vary. This confirms the g-mode nature of this star's pulsations as it excludes a radial mode of pulsation. Pulsation modes with $\ell \geq 1$ are expected.

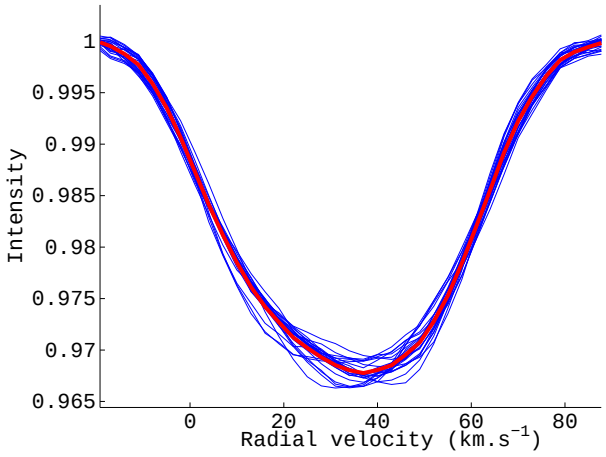

Figure 6.2: Variations of the cross correlated profile of AC Lep. The first 25 observations are displayed in blue while their mean is shown by the thick red line.

6.2.2 v sin i

From the mean of our 248 cross-correlated spectra we find $v \sin i = 37.9 \pm 0.5$ km.s^{-1}. As seen in Figures 6.3 and 6.4 we used two methods to determine $v \sin i$, the Fourier first minima method and the rotationally broadened Gaussian method, both described by Duflot et al. (1995) and used by Wright (2008). Both methods yield the same result. A least-squares fit of our data by a Gaussian profile broadened by the function of Gray (2005) gives $v \sin i = 37.92$ km.s^{-1}. Using the first minima method gives $v \sin i = 37.93$ km.s^{-1}. Our result is in good agreement with previous estimates: Wolff and Simon (1997) estimated 40 km.s^{-1}, Royer et al. (2002) found 42 km.s^{-1}, Mathias et al. (2004) found 37 km.s^{-1}, De Cat et al. (2006) determined 39 km.s^{-1} and Henry et al. (2007) obtained 41 km.s^{-1}. It is noted however that the methods used to

determine v sin i usually assume a symmetric line profile, whereas the mean of our 248 observations still exhibits an asymmetry.

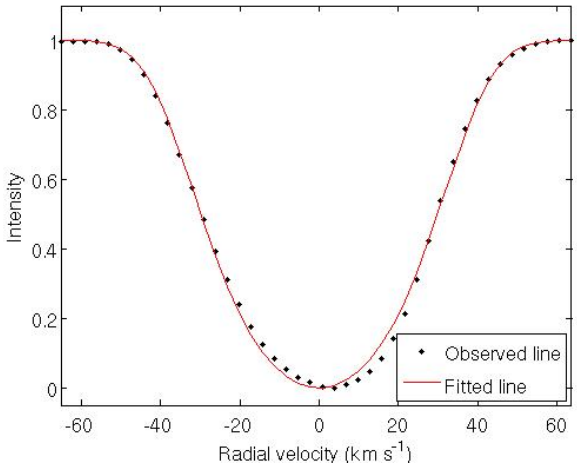

Figure 6.3: Measuring v sin i with the Gaussian method for AC Lep. The v sin i determination by fitting a broadened Gaussian to the mean spectral line of AC Lep. This yields v sin $i = 37.92 \pm 0.7$ km.s^{-1}. We can note the asymmetry in the data.

6.2.3 Radial velocity

Previous work by De Cat et al. (2006) and Henry et al. (2007), both using a cross-correlation technique, reported a radial velocity of 31.8 km.s^{-1} from eight and four spectra respectively.

We used the bisector method to determine the radial velocity at different levels in the cross correlated spectral line, as shown in Figure 6.5 and Table 6.2. Gray (1988) describes this method as the best way to describe the asymmetry. The line bisector consists of the midpoints of horizontal line segments extending across the profile. Since the average line is asymmetric, looking at different depths in the spectral line will yield different results. We used the value measured at 50% of the line depth to define the radial velocity. We also used the line bisector values at 50% and 90% to compute a slope which we denote as the line profile asymmetry parameter LPAP, representing the asymmetry in the line. In section 6.3.5 we show the results of analyzing the variations in this slope to find pulsation frequencies.

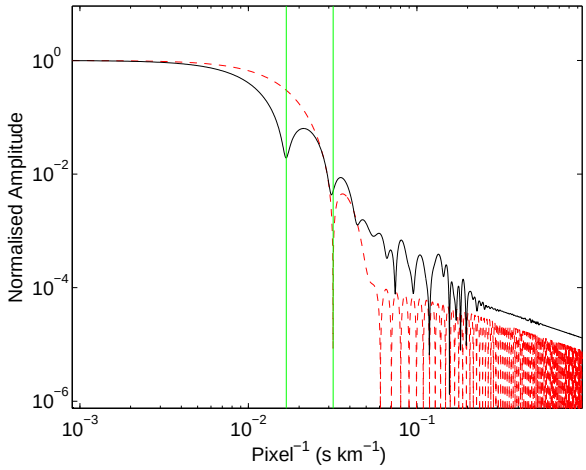

Figure 6.4: Measuring v sin i with the Fourier minima method for AC Lep. A log-log plot of the Fourier transform of the mean of our observations of AC Lep (solid line) is compared with a Gaussian broadened to v sin $i = 20$ km.s^{-1} (dashed line). The vertical lines indicate the positions of the first minima. The ratio of the first minima along the abscissa (multiplied by 20 km.s^{-1}) gives v sin $i = 37.93 \pm 0.5$ km.s^{-1}.

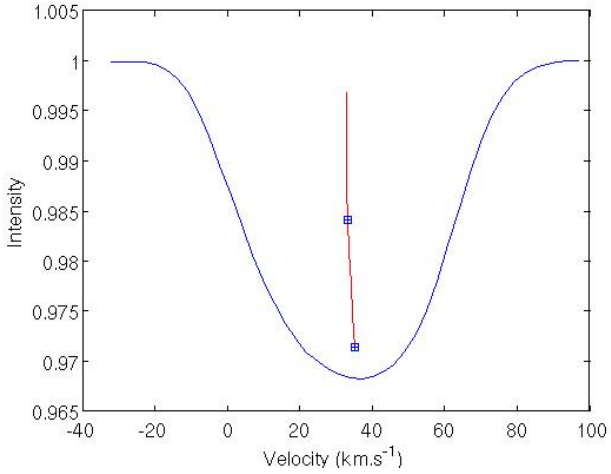

Figure 6.5: Radial velocity determination for AC Lep. The spectral line is the mean of 248 cross correlated observations and the central line is its bisector. The two symbols are situated at 50% and 90% of the line depth.

Table 6.2: Radial velocity of AC Lep measured at different depths of the mean spectral line.

Line depth (in %)	Velocity (km.s^{-1})
20	32.79
30	32.84
40	32.98
50	33.25
60	33.56
70	34.06
80	34.65
90	35.33

Table 6.3: Results from our detailed analysis of the radial velocity (RV) and v sin i. The latter used either the broadened Gaussian method $(v \sin i)_G$ or the Fourier minima method $(v \sin i)_F$. The mean line uses the mean of our 248 cross correlated observations. The other values refer to the analysis of the 248 individual observations. We chose a 50% line depth for our radial velocity measurements.

	RV km.s^{-1}	$(v \sin i)_G$ km.s^{-1}	$(v \sin i)_F$ km.s^{-1}
mean line	33.25	37.92	37.93
individual average	33.26	37.70	37.97
min	31.51	33.87	34.31
max	34.70	41.30	41.00
standard deviation (σ)	0.74	1.7	1.5

Summary Table 6.3 lists the results of these two methods on our individual observations, as well as the results of the radial velocity determination. The values of the minima and maxima represent the range of the 248 individual observations. The large standard deviations are expected in a pulsating star. The broadened Gaussian method gives results more scattered than with the Fourier minima method because it is more affected by the asymmetry of the line profile.

6.3 Frequency analysis

The same techniques are used for AC Lep with one exception: Since the noise level is higher we need to lower our spectral significance threshold in order to identify some frequencies. It is therefore set to 10 instead of 15 in the case of HD 189631.

The spectral window is presented in Figure 6.6. Since all observations for this star were taken from a single site (MJUO), it is expected to see strong aliasing patterns at $\pm$ 1 day around the true frequency(ies).

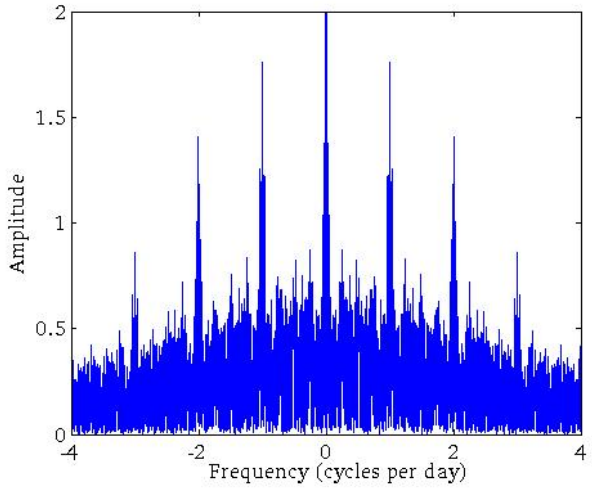

Figure 6.6: The spectral window shows the expected aliasing pattern due to our data sampling.

6.3.1 Photometric frequency analysis

AC Lep was discovered to be variable with a frequency of 1.2134 d^{-1} by the Hipparcos mission team (Perryman and ESA, 1997). It has been progressively admitted as a γ Doradus star through the works of Aerts et al. (1998), Handler (1999), Kazarovets et al. (2000) and Handler and Shobbrook (2002). Aerts et al. (1998) re-analyzed the Hipparcos data and found frequencies of 1.1426 d^{-1} and 1.1211 d^{-1}, but only poorly explaining the total variance observed in the data. Henry et al. (2007) identified four frequencies from more than 270 photometric observations: 1.2132, 0.7361, 0.5377 and 2.1820 d^{-1} in amplitude order. However, due to the low amplitudes involved, they note that a misidentification of one or two frequencies was possible.

We therefore performed our own frequency identification on the data of Henry et al. (2007). Re-analyzing the data from the B filter confirms their results (1.2132, 0.7362, 0.5375 and 2.1820 d^{-1}), while the data from the V filter gives a slightly different result: 1.2140, 0.5380, 0.7360 and 1.1797 d^{-1} in amplitude order. Note the reversal of the second and third frequencies and the possible one day alias with the last frequency.

6.3.2 Equivalent width frequency analysis

A Fourier analysis of the equivalent width variations has identified three frequencies: $f_4 = 0.9764$ d^{-1}, $f_5 = 4.9937$ d^{-1}, and $f_1 = 0.7523$ d^{-1} (see Figure 6.7). Only the third one has been previously identified as a secondary frequency by Henry et al. (2007) from photometry. Fitting the three frequencies and their amplitude to the data explains 55% of the variations observed in the equivalent width measurements. f_4 alone is responsible for 39% while f_4 and f_5 together explain 47%.

When the equivalent width data are phased to these three frequencies the sampling is good.

Figure 6.8 focuses on a portion of the data (91 observations) taken during 11 nights in January 2009. The fit includes f_3, f_4 and f_1.

6.3.3 Radial velocity frequency analysis

The first moment analysis (radial velocity variations) shows two frequencies: $f_1 = 0.7523$ d^{-1} and $f_3 = 0.5782$ d^{-1} (Figure 6.9). The latter frequency might be related to the third one listed by Henry et al. (2007) at 0.5380 d^{-1}. Evaluating the residuals show that f_1 is responsible for 43% of the observed variations of measured radial velocity. Adding f_3 to this analysis explains 54% of the variations. Figure 6.10 focuses on a portion of the data (91 observations) taken within 11 nights in January 2009. The fit includes f_1 and f_3.

6.3.4 Pixel-by-pixel frequency analysis

The pixel-by-pixel method allows us to identify two frequencies $f_2 = 1.0863$ d^{-1} (Figure 6.11) then $f_1 = 0.7523$ d^{-1}, even if an alias (1-f) comes first (Figure 6.12). We believe we made the right choice because $f_1 = 0.7523$ d^{-1} has been previously identified in our analysis and in the photometric work of Henry et al. (2007).

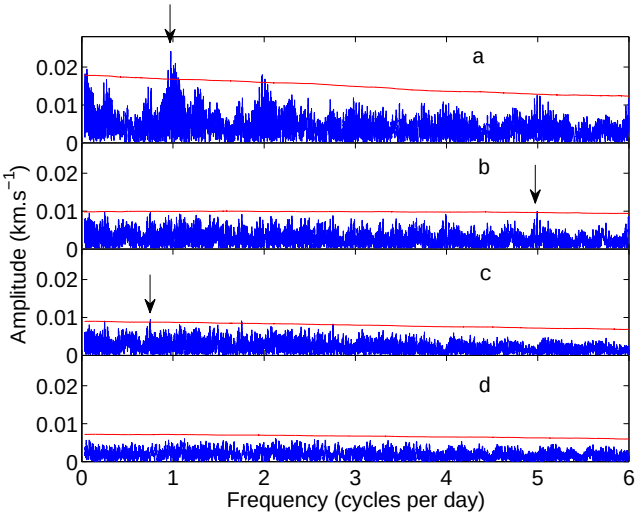

Figure 6.7: Fourier analysis for AC Lep of the variation in equivalent widths. (a) Identifies $f_4 = 0.9764$ d^{-1} as the main frequency with an amplitude of 0.024 km.s^{-1}. After prewhitening the data we find (b) $f_5 = 4.9937$ d^{-1} at an amplitude of 0.010 km.s^{-1}, and finally (c) $f_1 = 0.7523$ d^{-1} at an amplitude of 0.009 km.s^{-1} after prewhitening for both previously identified frequencies. (d) shows the noise floor. Our detection limit is shown by the solid red line.

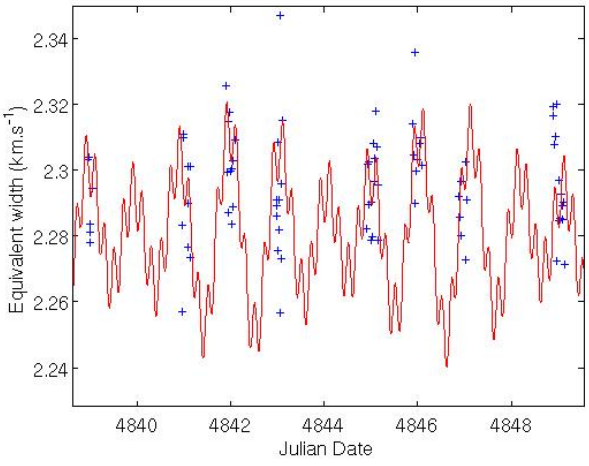

Figure 6.8: Equivalent width variations of AC Lep fitted with three frequencies. The equivalent width of 91 cross-correlated line profiles of AC Lep taken over 11 nights (2009 Jan 7-17) is fitted by a solid line produced by a combination of f_4, f_5 and f_1.

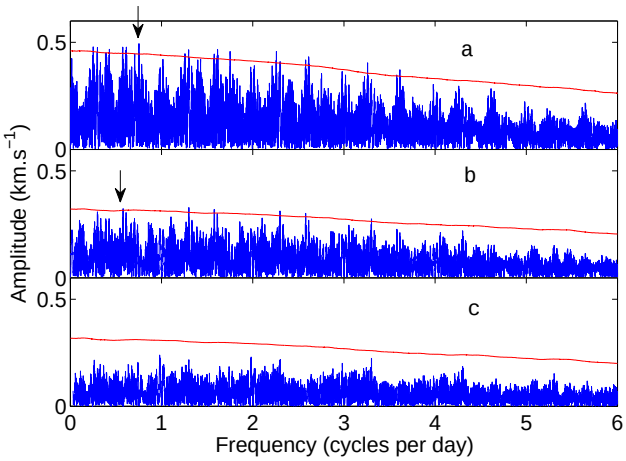

Figure 6.9: Fourier analysis for AC Lep of the variation in radial velocity. (a) identifies $f_1 = 0.7522$ d^{-1} as the main frequency with an amplitude of 0.49 km.s^{-1}. After prewhitening the data we find (b) $f_3 = 0.5782$ d^{-1} at an amplitude of 0.33 km.s^{-1}. (c) shows the noise floor. Our detection limit is shown by the solid red line.

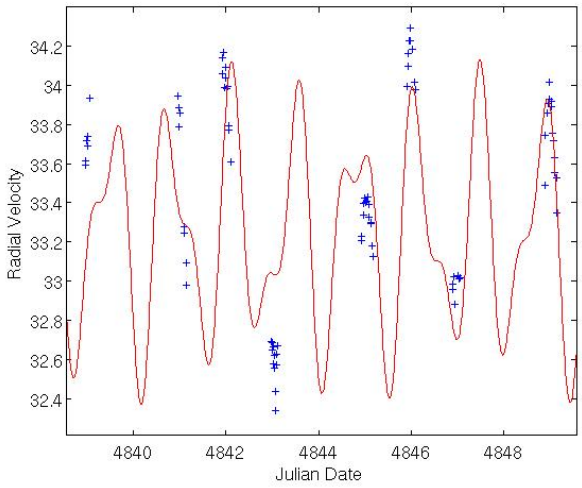

Figure 6.10: Radial velocity variations (in km.s^{-1}) of AC Lep fitted with two frequencies. The radial velocity of 91 cross-correlated line profiles of AC Lep taken within 11 nights (2009 Jan 7-17) is fitted by a solid line produced by a combination of f_1 and f_3.

In the left panel of Figure 6.13 we show the line profile variations after subtracting the mean line profile from all observations. The data are phased on the first identified frequency using the pixel-by-pixel method: $f_2 = 1.0863$ d^{-1}. Specific patterns on these 2-dimensional grey-scale plots are often a characterization of the mode of pulsation. We can see a trend going from the bottom left corner to the top right corner. It can be compared with a least-squares fit to the data using the parameters derived when finding f_2, i.e. the amplitude and phase across the profile at each point in the line profile (right panel of Figure 6.13). This fit accounts for 17% of the variations observed in our data set.

We can now prewhiten the data (which is equivalent to subtracting the right panel of Figure 6.13 from its left panel) and phase it again to $f_1 = 0.7523$ d^{-1}, as shown on Figure 6.14. Performing a least-squares fit of both frequencies on the data shows that 36% of the total variations of intensity observed in the line profile can be explained.

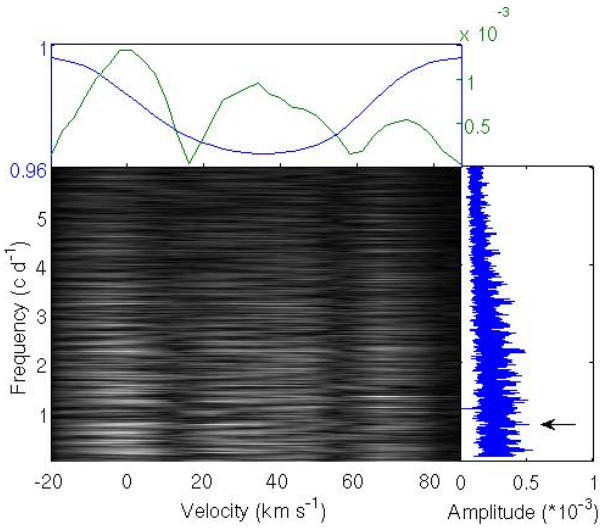

Figure 6.11: Fourier analysis using the pixel-by-pixel method on the AC Lep data. The top panel shows the mean spectral line along with the amplitude variations at $f_2 = 1.08635$ d^{-1}. The centre panel shows the 2D frequency analysis for each pixel of the profile. The right panel shows an average across the profile. We identify $f_2 = 1.08635$ d^{-1} as the main frequency, indicated by an arrow.

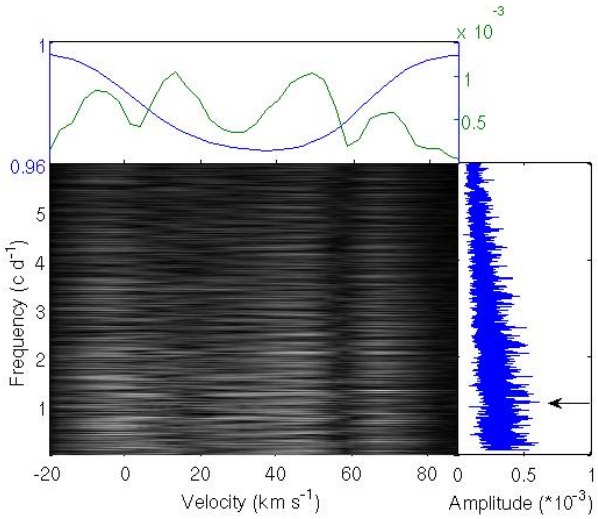

Figure 6.12: Fourier analysis using the pixel-by-pixel method on the data of AC Lep. After prewhitening the data we find a frequency at 0.24767 d^{-1}, but we identify this as an alias (1-f) and instead take $f_1 = 0.7521$ d^{-1} as our second frequency.

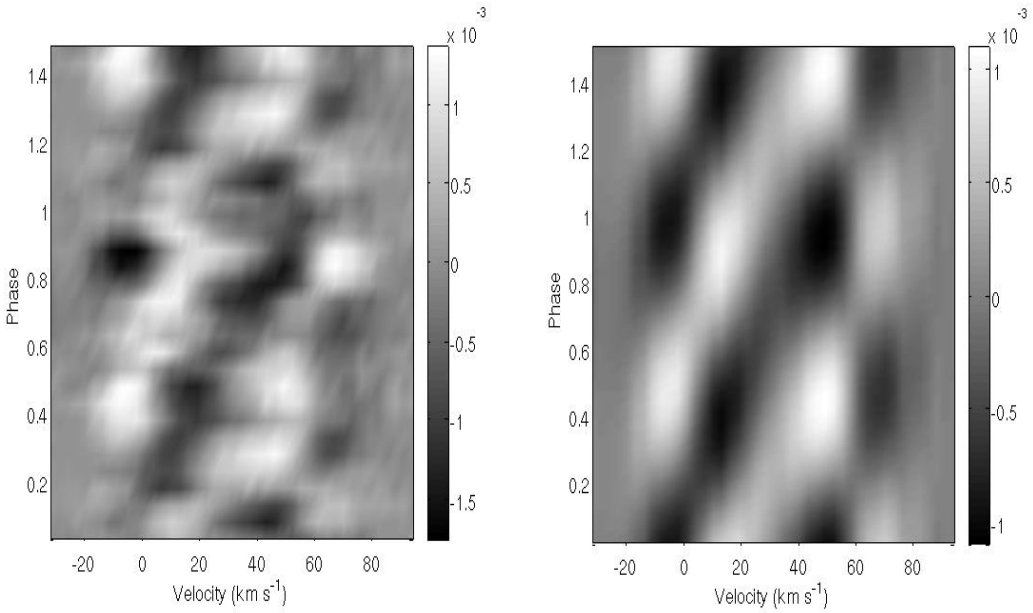

Figure 6.13: Left panel: Line profile variations observed in AC Lep. Right panel: A least-squares fit to the AC Lep data is done with the amplitude and phase across the profile for that frequency. The data is phased on the first frequency found by using the pixel-by-pixel method: $f_2 = 1.0863$ d^{-1}. The average line profile has been subtracted from all observations.

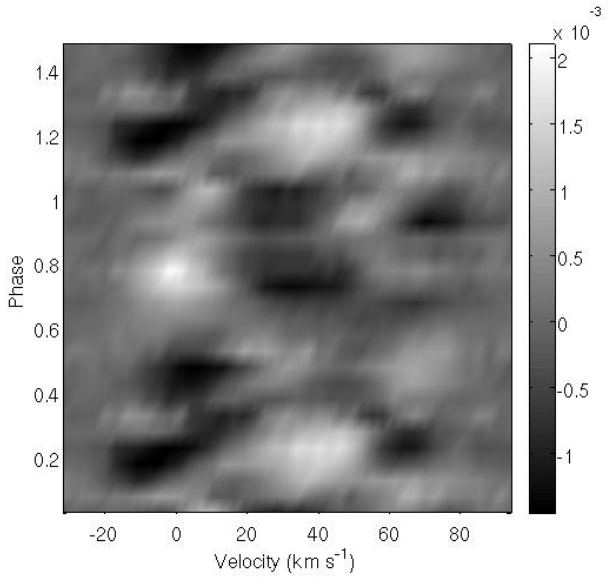

Figure 6.14: Line profile variations observed in AC Lep after prewhitening with the first frequency. The data is phased on the second frequency found by using the pixel-by-pixel method: $f_1 = 0.7521$ d^{-1}. The average line profile has been subtracted from all observations.

6.3.5 Investigating the variations of the asymmetry of the line profile

The results of the LPAP analysis are shown on Figure 6.15. The highest peak at 0.0867 d^{-1} is considered to be an alias of 1.0898 d^{-1} due to its low frequency and the fact that it corresponds to a one-day alias ($f_2 - 1$) of the first frequency in section 3.2.4. The second highest peak is at $f_1 = 0.7523$ d^{-1} and the third is $f_2 = 1.0898$ d^{-1}, but these two frequencies have almost equal amplitudes. If we prewhiten the data with f_1 we recover f_2.

Note that for AC Lep the mean LPAP is equal to 4.99 km.s^{-1}. This is strongly asymmetric.

Figure 6.16 shows the fit produced by both frequencies on a selected fraction of the data (91 observations in January 2009). The fraction of the variance explained by f_1 is 21%, and by f_1 and f_2 is 46%.

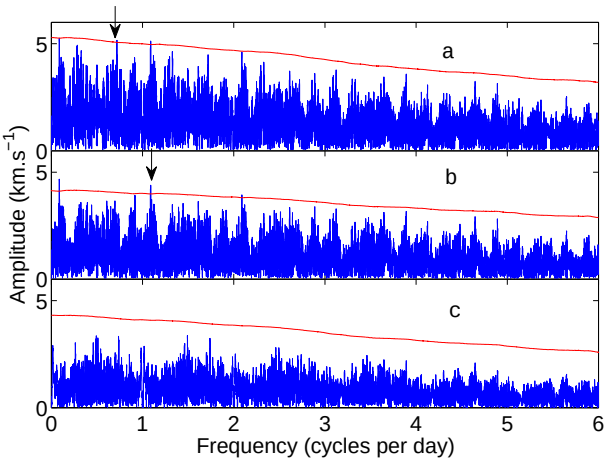

Figure 6.15: Fourier analysis of the LPAP data set of AC Lep. (a) is showing the highest peak at 0.0867 d^{-1}, but is considered a (f-1) alias of f_2. The second highest peak is at f_1=0.7523 d^{-1} at an amplitude of 5.12 km.s^{-1}. After prewhitening the data with f_1 (b) we find f_2=1.0898 d^{-1} with an amplitude of 4.40 km.s^{-1}. (c) shows the noise floor. Our detection limit is shown by the solid line.

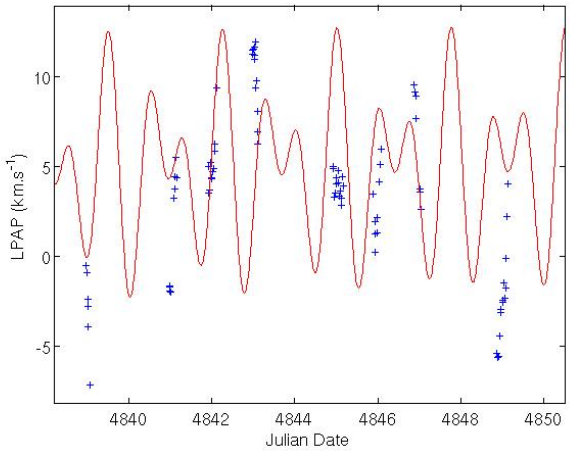

Figure 6.16: LPAP of AC Lep fitted by two frequencies. The LPAP of 91 cross-correlated line profiles of AC Lep taken within 11 nights (2009 Jan 7-17) is fitted by a solid line produced by a combination of f_1 and f_2.

6.3.6 Summary of frequencies

In Table 6.4 we summarize the frequencies identified for AC Lep from the various methods.

It is clear that the main pulsational frequency is $f_1 = 0.7523 \pm 0.0005$ d^{-1} as we found it using three different methods and it was seen as the 2^{nd} strongest frequency in the photometric analysis by Henry et al. (2007). We also note that our secondary frequency $f_2 = 1.0863 \pm 0.0007$ d^{-1} has not been listed previously. This could mean that f_2 is associated with a pulsation mode that is hard to detect with photometry. The frequencies and their associated uncertainties listed here are the ones found with the pixel-by-pixel method as it is the one giving us the lowest uncertainties.

It is interesting to note that the main frequency found by previous photometric analysis (1.213 d^{-1}) is not detected in our data, so a good combination of spectroscopic and photometric analysis is required in order to detect a maximum number of pulsation frequencies. More data in a concentrated campaign is needed to confidently determine the frequencies of variation occurring in this star.

The sampling of these two frequencies by our data set is shown on Figure 6.17. The histograms are proving that both f_1 and f_2 are very well sampled.

6.4 Mode identification

A large set of parameters is used as input for the mode identification. The values used for the metallicity, effective temperature and log g are taken from the spectroscopic analysis of Bruntt et al. (2008). The mass and radius are estimated according to these parameters and the spectral type, which seem to indicate that AC Lep is situated just above the main sequence like a pre-MS star or a subgiant.

The first set of parameters are not allowed to vary because we need to limit the parameter space in order to have the algorithm functioning at its best. It does not affect our results since these parameters have negligible effects on the mode identification. The equivalent width is an exception as it is critical in the identification of the modes, but its determination is very precise so we already know what the result will be if we let it vary. This was confirmed by simulations with smaller parameter space but a free equivalent width.

Table 6.4: Summary of all possible frequencies for AC Lep pulsations. All frequencies are in units of d^{-1} and the corresponding amplitudes are shown in brackets. Amplitudes should only be compared within a column because they scale differently depending on which method was used, and the units are different: Equivalent width (EW), radial velocity (RV) and LPAP amplitudes are in $km.s^{-1}$, pixel-by-pixel (PbP) amplitudes are in normalized intensity $*10^{-3}$, and photometric amplitudes are in units of mmag. The bottom part shows the fraction of the variation explained by fitting the frequencies to the data.

f	EW	RV	PbP	LPAP	Phot. [a]
d^{-1}	$km.s^{-1}$	$km.s^{-1}$	$*10^{-3}$	$km.s^{-1}$	(mmag)
f_1	0.75 (0.09)	0.75 (0.49)	0.75 (5.2)	0.72 (5.16)	0.74 (4.31)
f_2			1.09 (6.1)	1.09 (3.68)	
f_3	0.98 (0.024)				
f_4	4.99 (0.010)				
f_5		1.30 (0.33)			
f_6					1.21 (5.52)
f_7					0.54 (3.66)
f_8					2.18 (3.88)
one f	22% (f_3)	29% (f_1)	11% (f_2)	21% (f_1)	13% (f_6)
two f	27% ($f_3 + f_4$)	42% ($f_1 + f_5$)	23% ($f_2 + f_1$)	36% ($f_1 + f_2$)	20% ($f_6 + f_1$)
three f	33% ($f_3 + f_4 + f_1$)				26% ($f_6 + f_1 + f_7$)
four f					31% ($f_6+f_1+f_7+f_8$)

[a] Henry et al. (2007)

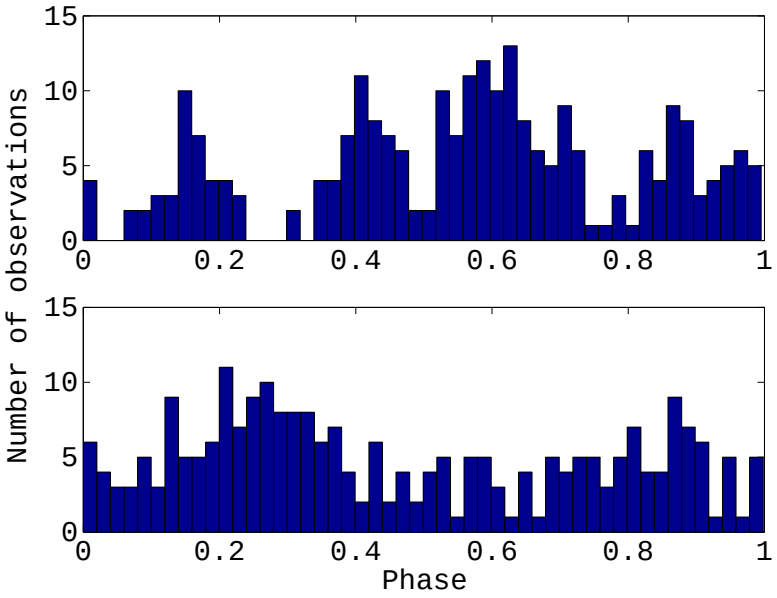

Figure 6.17: Frequencies of AC Lep sampled by our data set. The top panel shows the sampling of f_1 while the bottom panel is for f_2.

- R= 1.7 $R_\odot$
- M= 1.2 $M_\odot$
- $T_{eff} = 6900$ K
- $\log g = 4.05$
- $[Fe/H] = 0.08$
- Equivalent width= 2.35 km.s^{-1}

The next set of input parameters, all characteristics of the mean line profile, were allowed to vary to improve the fit:

- $v \sin i$ from 35 to 39 km.s^{-1}
- i from 8^o to 90^o
- Intrinsic width from 5 to 16 km.s^{-1}

- Zero-point shift (radial velocity) from 29 to 33 km.s^{-1}

Then for each frequency we explore a large parameter space for the pulsational mode characteristics:

- ℓ from 0 to 5
- m from $-\ell$ to $+\ell$
- Amplitude from 0.1 to 20 km.s^{-1}
- Complete range for the phase from 0 to 2π

6.4.1 Independent mode identifications

The parameter space involved for a full mode identification is extremely large and we need to reduce it in order for the algorithm to function properly. We thus start with mode identifications on each frequency independently. The primary pulsation is best fitted by a mode with $(2\ ;\ -1)$, i.e. $\ell = 2\ ;\ m = -1$, with $\chi^2 = 15$. The radial velocity and v sin i agree with the previous results within their respective uncertainties. This fit does not provide any information about the inclination angle as changing i has little effect on the fit. It is therefore not restrictive with other pulsations.

The mode identification of the secondary pulsation is easier because this pulsation is characterized by four maxima in the mean amplitude variation spectrum (Figures 6.20 & 6.21). This limits the possibilities as few modes behave in this way. The best fit is obtained by a $(3\ ;\ -3)$ mode with $\chi^2 = 11$. This fit is strongly dependant on the inclination angle. The second best fit is a $(2\ ;\ -2)$ mode with $\chi^2 = 13$. It also gives us information about the inclination angle. Figure 6.18 summarizes the most likely modes along with their dependency on the inclination angle of the star.

These independent fits provide us with a different set of parameters (radial velocity, rotational velocity and inclination angle) for each pulsation, so a combined fit is required to achieve consistency of these stellar parameters.

6.4.2 Combined mode identification

Now that a few modes have been selected we can run a combined mode identification with a smaller parameter space. The two solutions considered have very similar χ^2

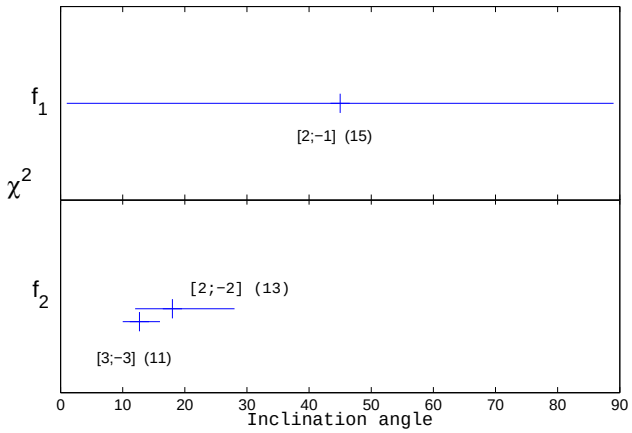

Figure 6.18: χ^2 plot of the inclination angle depending on the different modes of pulsation for AC Lep. Only the most likely modes are displayed. The horizontal lines represent the range of probable values of i and the small vertical lines indicate its most likely value. The value of ℓ and m are in square brackets with their associated χ^2 value to their right. The result for the primary frequency is on top while the result for the secondary frequency is below.

values so we will present both results. The fit to the primary pulsation for both solutions is the same and shown on Figure 6.19. The 95%-confidence limit of χ^2 is 52. Table 6.5 lists our best results.

The best fit, obtained by a $(3\ ;\ -3)$ mode for the secondary pulsation with $\chi^2 = 24$, is shown on Figure 6.20. It tells us that the zero-point shift, or radial velocity, is around 30 km.s^{-1}, which disagrees with our analysis in section 4.1. It is interesting to note that the centre of the amplitude variations does not agree with the centre of the spectral

Table 6.5: Results of a mode identification of AC Lep for both identified frequencies. The first four columns correspond to the ℓ and m wavenumbers of the pulsation modes associated with each frequency.

f_1	f_2	i	$v \sin i$ km.s^{-1}	Radial velocity km.s^{-1}	Intrinsic width km.s^{-1}	χ^2
2;-1	3;-3	13^o	38.0	29.9	9.0	24
2;-1	2;-2	18^o	38.0	30.1	11.2	25
2;-1	3;-2	17^o	38.9	32.3	13.4	37

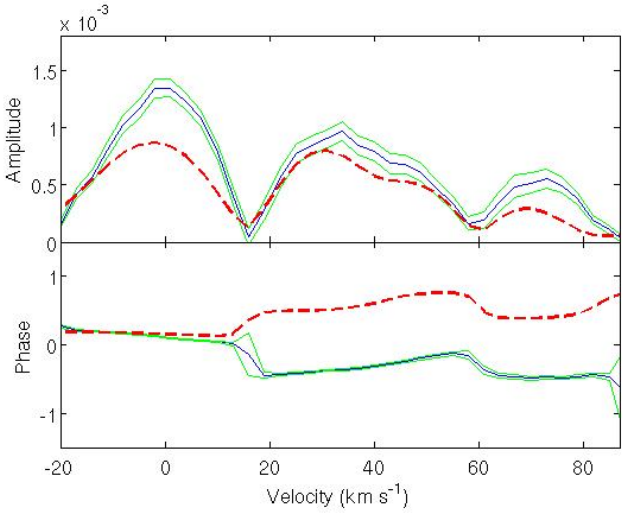

Figure 6.19: First pulsational mode of AC Lep. Fourier parameters of the primary pulsation of AC Lep fitted by a $(2\ ;\ -1)$ mode. The amplitude is measured in normalized intensity and the phase is dimensionless. The data is surrounded by its uncertainty, the dashed line is the fit.

line. Another note is that the inclination angle of the star is very small in this case: $i = 12.7^o \pm 6$. With the known v sin i (38 km.s^{-1}) this yields a very high rotational velocity of 172 km.s^{-1}. Changing i produces a very different amplitude variation so i is one of the most important factors in this case to obtain a good fit. It is possible that AC Lep is a fast rotator, or that this mode has been misidentified.

Figure 6.21 shows the second best fit which is obtained by an $(2\ ;\ -2)$ mode for the secondary pulsation with $\chi^2 = 25$. The inclination angle is now $17.9^o \pm 11$, which yields to slower rotational velocity.

6.5 Summary

The analysis of AC Lep was based on 248 observations, all obtained from MJUO in Tekapo, New Zealand. From this the v sin i can be found at 37.9 ± 0.5, and the radial velocity at 33.2 km.s^{-1}.

We found several frequencies in the Fourier spectrum of AC Lep, only one, $f_1 = 0.7521 \pm 0.0005$ d^{-1}, being convincing because it was found with several methods including photometry. Only one other frequency $f_2 = 1.0864 \pm 0.0007$ d^{-1} was found by two methods. Three more frequencies ($f_3 = 0.98$ d^{-1}, $f_4 = 4.99$ d^{-1} and $f_5 = 1.30$ d^{-1})

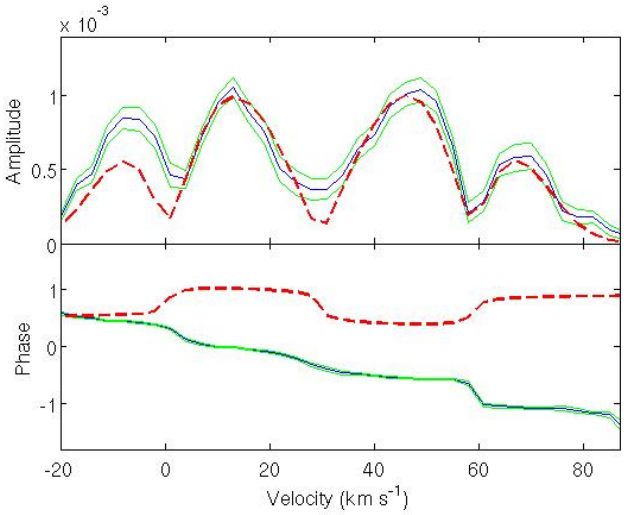

Figure 6.20: Second pulsational mode of AC Lep. Fourier parameter of the secondary pulsation of AC Lep fitted by a mode with $(3\ ;\ -3)$.

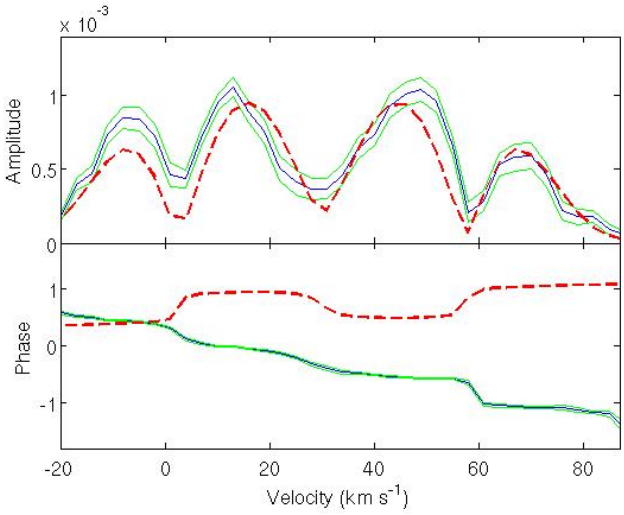

Figure 6.21: Second pulsational mode of AC Lep (bis). Fourier parameter of the secondary pulsation of AC Lep fitted by a mode with $(2\ ;\ -2)$.

were found with low amplitudes and the three other frequencies listed by Henry et al. (2007) using photometry (their $f_1 = 1.2132$ d^{-1}, $f_3 = 0.5377$ d^{-1} and $f_4 = 2.1820$ d^{-1}) could not be confirmed by our spectroscopic study. We restricted ourselves to only two frequencies for the mode identification because if a frequency is misidentified its mode identification is meaningless and all mode identifications performed on other pulsations are compromised. For f_1 we identified a mode with $(2\ ;\ -1)$ and for f_2 we found $(3\ ;\ -3)$ or $(2\ ;\ -2)$. An extensive set of observations is needed to improve the quality of this analysis.

Chapter 7

Discussion

This chapter summarizes and discusses the results of Chapters 4, 5 and 6 about the frequency determination and mode identification of the data sets of, respectively, PT Pup, HD 189631 and AC Lep. The line profiles of other targets observed during this work are presented, and, if enough spectra were obtained, preliminary results are given. A parallel is done with the results from the literature cited in Chapter 1.

7.1 Frequency and mode identification on β Cephei stars

Many methods have been used for the frequency analysis of the PT Pup data and have identified two frequencies. A clear primary frequency at $f_1 = 6.0743 \pm 0.0001$ d^{-1} and a lower amplitude secondary frequency at $f_2 = 5.9938 \pm 0.0002$ d^{-1}. These were derived from the analysis of the radial velocity variations in the Si III line at 4552 Å. Other methods were used on Si III and also on other single lines or cross-correlated profiles. All analysis gave very similar results. Both frequencies can be linked to the ones found by Heynderickx (1992), although their relative amplitudes have been inverted as their primary frequency corresponds to our secondary, and their secondary to our primary: 6.01016 ± 0.00001 d^{-1} and 6.06352 ± 0.00002 d^{-1}.

The FPF method gives excellent results in the case of PT Pup (Chapter 4). The only issue concerns the discrimination between the low ℓ modes. In particular, the synthetic radial mode produces a very sharp transition between the left and right parts of the phase across the profile. This sharp transition is probably not observable in real data, as it would mean that all the surface elements behave perfectly according to the

pulsation. No other dynamics are taken into account in the models, such as coronal mass ejection. Thus a radial mode should not be ruled out on the only argument that another mode produces a better fit. Complementary and independent mode identification from photometry can bring the missing piece of information. Axisymmetric ($m = 0$) modes in general are discriminated against when using the FPF method for the same reason. Taking this into account, and referring to the photometric result of Heynderickx et al. (1994), the primary pulsation ($f_1 = 6.0743$ d^{-1}) is thought to be a radial mode, while for the secondary pulsation ($f_2 = 5.9938$ d^{-1}) two modes are possible: ($\ell = 2$; $m = 0$) and ($\ell = 1$; $m = +1$).

The amplitudes of pulsations of PT Puppis were found to vary greatly when compared to the results of Heynderickx (1992). As seen at the end of chapter 4, this is largely explained by the method of analysis if we take $\ell = 0$ for f_1 and $\ell = 2$ for f_2. Largely, but not completely explained, which suggests that intrinsic variations in the pulsation amplitudes have occurred. Either the amplitude of f_1 increased or the amplitude of f_2 decreased, or both happened simultaneously.

The spectroscopic data set of another β Cephei star, HD 163472, has been analyzed by Wright (2008), identifying a radial mode and a $\ell = 3$ or $\ell = 4$ mode. These results, as well as others, based on photometry and/or spectroscopy, from Aerts et al. (2003), De Ridder et al. (2004), Handler et al. (2006), Desmet et al. (2009) or Briquet et al. (2009), suggest that all β Cephei stars pulsate in low degree ℓ modes, with at least one radial ($\ell = 0$) mode. However this could be a selection effect since the observed targets were chosen for their high amplitudes and low projected rotational velocities. They thus have a higher probability to have radial modes excited to observable amplitudes.

Finally, HD 64365 was observed in order to chose a β Cephei target for this thesis. After obtaining 16 observations it was clear that the LPVs were very strong and the same conclusions could be made at that stage about both β Cephei targets, PT Pup and HD 64365. The latter was not chosen in this work because it was fainter than PT Pup. The Si III spectral line is shown for the 16 observations in Figure 7.1.

The mean of these observations allows us to estimate the radial velocity at 25.0 km.s^{-1} using the bisector method. The value of $v \sin i$ is low and the methods used are not reliable in the case of a hot, slowly rotating star. By adopting a conservative approach, $v \sin i$ can be confirmed to be less than 20 km.s^{-1}. The large amplitude of the pulsation,

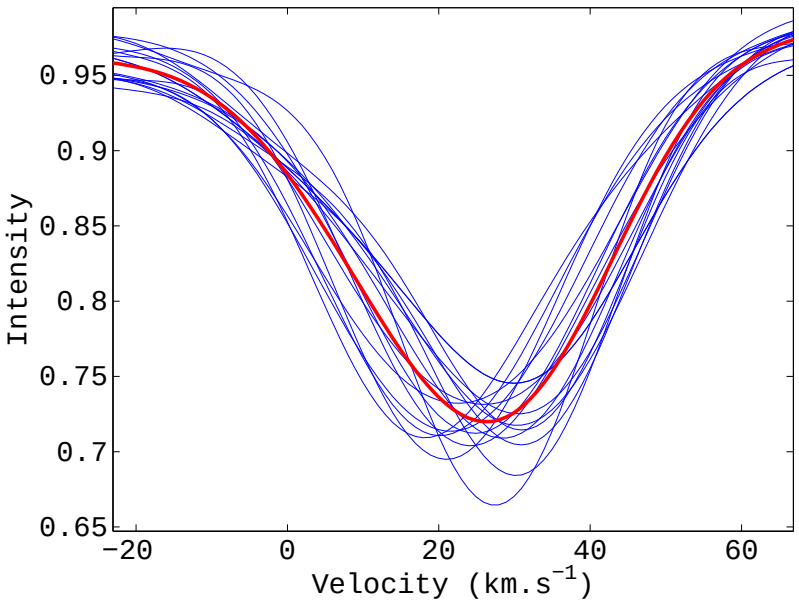

Figure 7.1: Line profile variations in HD 64365. The Si III line at 4553 Å taken from 16 observations is found to be strongly varying. The mean of all observations is shown in red.

and the fact that the symmetry of the line profile is maintained during the pulsation, points towards a low degree mode like in PT Pup.

From our experience of β Cephei pulsations, 40 to 100 observations should be enough to determine the frequency and amplitude of one or two pulsations, as well as identifying their mode of pulsation. This number depends on the magnitude of the star, the amplitude of its pulsations, the resolving power of the instruments used and the sampling of observations. Much larger data sets could be used to study more pulsations, or analyze the temporal variations in amplitude, and maybe frequency, of the pulsations. In the case of γ Doradus pulsators, the accurate determination of frequencies and the identification of their pulsational modes are already important challenges requiring extremely large data sets.

7.2 Frequency and mode identification on γ Doradus stars

We found several frequencies in the Fourier spectrum of AC Lep, only one, $f_1 = 0.7521 \pm 0.0005$ d^{-1}, being convincing because it was found with several methods including

photometry. Only one other frequency $f_2 = 1.0864 \pm 0.0007$ d^{-1} was found by two methods. Three more frequencies ($f_3 = 0.98$ d^{-1}, $f_4 = 4.99$ d^{-1} and $f_5 = 1.30$ d^{-1}) were found with low amplitudes and the three other frequencies listed by Henry et al. (2007) using photometry (their $f_1 = 1.2132$ d^{-1}, $f_3 = 0.5377$ d^{-1} and $f_4 = 2.1820$ d^{-1}) could not be confirmed by our spectroscopic study. The identified frequencies can only account for at most 55% of the observed pulsation; this leaves about 45% ignored in the analysis of AC Lep so we must be cautious in the interpretation of the results of the mode identification. The noise level is high. More frequencies, including the ones found by photometric studies, could be found on a larger data set. In particular it is suspicious that the frequency with the largest amplitude in photometry could not be detected in our study. We suggest a data set of more than 400 observations within a single season to improve the quality of our analysis on this star would be required, as it seems that 248 data points are still not enough in the case of AC Lep. We plan on obtaining more spectra of this star in the future. We restricted ourselves to only two frequencies for the mode identification because if a frequency is misidentified its mode identification is meaningless and all mode identifications performed on other pulsations are compromised. This is the complicated puzzle of AC Lep. For f_1 we identified a mode with (2 ; −1) and for f_2 we found (3 ; −3) or (2 ; −2).

The analysis is simpler for HD 189631 where four frequencies are found: $f_1 = 1.6719 \pm 0.0005$ d^{-1}, $f_2 = 1.4200 \pm 0.0005$ d^{-1}, $f_3 = 0.0711 \pm 0.0005$ d^{-1} and $f_4 = 1.8227 \pm 0.0005$ d^{-1}. The only result previously published on this star was by Handler (1999) and confirms $f_1 = 1.67$ d^{-1} from photometry. The identified frequencies account for 70% of the observed pulsation, which is satisfying, but possibly leaves a few low amplitude pulsations to be identified because the noise was much lower on this target. We have some confidence in the mode identification of the pulsations associated with f_1 (1 ; +1) and f_3 (2 ; −2). We are not satisfied by the fit obtained for f_2 with (3 ; −2) mode, but it is still the best solution. For f_4 we hesitate between two modes: (4 ; +1) or (2 ; −2). Preliminary work on this star with a data set comparable in size to the one we have for AC Lep also gave results easier to interpret than our results on AC Lep.

We have more confidence in our frequency determination for HD 189631 than for AC Lep. Note that the amplitudes of the equivalent width variations are small, thus the modes of pulsation associated with all frequencies appears to have a very small effect

on the equivalent width of the spectral line. When a pulsation affects the spectral line by decreasing the intensity on one side of the profile, the intensity on the other side is increased. The pulsation induces Doppler shifting by movements of surface elements, but the overall absorption of light by the chemical elements in the stellar atmosphere is vastly unchanged. Thus the equivalent width remains unaffected by the pulsations.

Spectroscopic mode identification of other γ Doradus stars have been published. Balona et al. (1996) worked on γ Doradus itself, identifying $f_1 = (3; +3)$, $f_2 = (1; +1)$ and $f_3 = (1; +1)$. Aerts et al. (2004a) identified only $\ell = 1$ modes for three pulsations in HD 12901 and three pulsations in HD 48501. This was also the case for two pulsations of HD 209295 studied by Handler et al. (2002). These results seem to indicate that most, if not all, γ Doradus pulsations are $\ell = 1$ modes. However, contrary to this, Uytterhoeven et al. (2008a) note about HR 2514 that

> "all modes, for which an identification was possible, appear to be high-degree modes ($3 \leq \ell \leq 8$), which implies that future modelling will be extremely challenging."

Lower degree modes were identified in our work, but we nevertheless agree with the statement that modelling will be extremely challenging. Hatzes (1998) and Jankov et al. (2006) find high degree modes ($\ell \geq 2$) in γ Doradus variables, respectively HD 164615 and HD 195068. The only previous mode identification using the FPF method was done by Wright (2008) on QW Puppis (HD 55892) and NX Lupus (HD 139095). High degree modes were identified in both cases. The frequencies, amplitudes and modes of pulsations listed from nine published works in spectroscopic mode identification are all presented graphically in Figure 7.2, taken from Table 1.1. It is interesting to note that the apparent dominance of $\ell = 1$ modes can be due to a selection effect. Among the g modes, these are the least affected by geometrical cancellation. They will have large apparent amplitudes and will be easily detected by surveys of variability. Their higher signal-to-noise ratio also allows for an easier mode identification.

Uytterhoeven et al. (2008a) also found that the star HR 2514 shows both γ Doradus and δ Scuti types of pulsation. They suggest that this would be the case for many γ Doradus stars. We were unable to detect δ Scuti type pulsations in AC Lep and HD 189631.

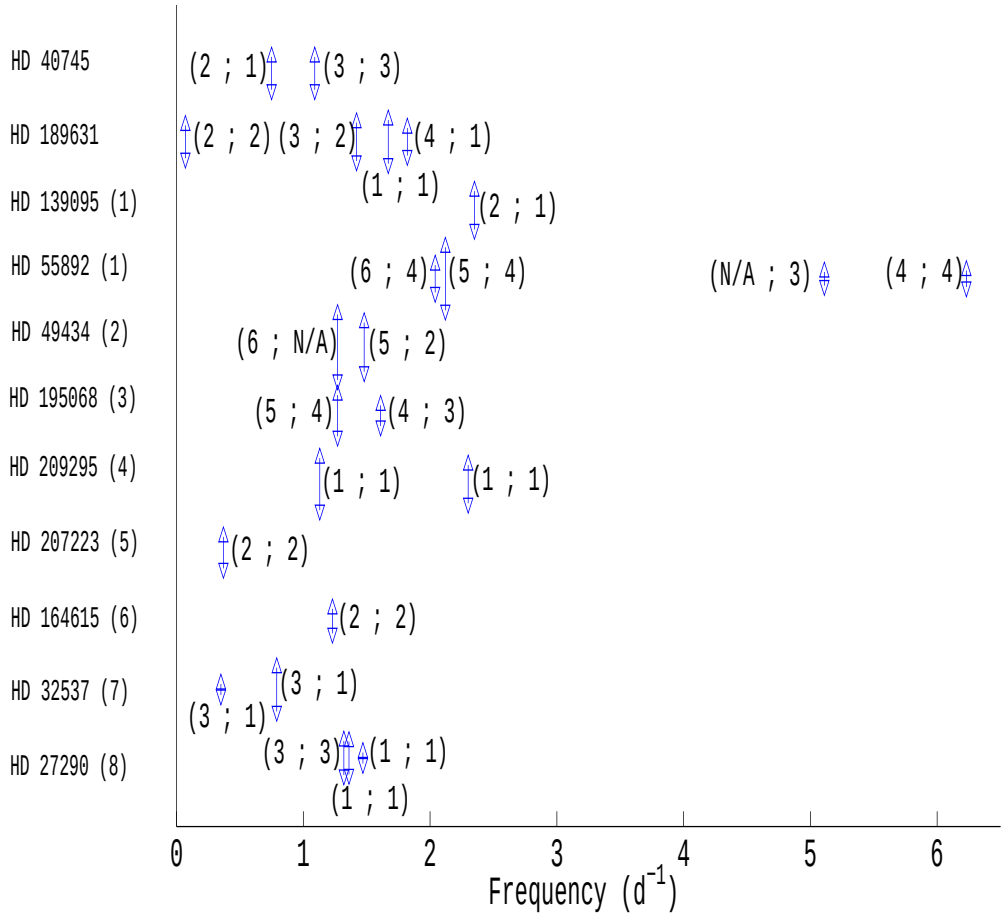

Figure 7.2: Results of spectroscopic mode identification of γ Doradus stars from the literature. The size of the bars is proportional to the amplitude of the corresponding frequency. Since these amplitudes are obtained from different techniques in different publications, they can only be compared relative to other frequencies identified in the same paper. For each frequency, the identified pulsational mode is indicated in brackets in this form: $(\ell\ ;\ m)$. The results of nine different publications are represented on this graphic. The references on the y axis correspond to: (1) Wright (2008); (2) Uytterhoeven et al. (2008a); (3) Jankov et al. (2006); (4) Handler et al. (2002); (5) Aerts and Kaye (2001); (6) Hatzes (1998); (7) Aerts and Krisciunas (1996); (8) Balona et al. (1996).

7.3 Additional γ Doradus targets

In this work we obtained a few spectra on four other γ Doradus stars. All four have been classified as bona fide γ Doradus targets, by De Cat et al. (2006) for EP Cetus and IN Libra, and by Handler and Shobbrook (2002) for V769 Monoceros and NX Lupus. As the study of γ Doradus type pulsations requires many observations, we had to concentrate our efforts on AC Lep, therefore leaving these targets to be studied in detail in future work.

All observations about these four stars were obtained from MJUO. Single line profiles are presented here instead of cross-correlated profiles because cross-correlation relies on a good fit to the mean spectrum of the star which is not possible from this sparse sample. Therefore, in Figures 7.3 to 7.6, which present the Ca I line at 6122 Å for these stars, the signal-to-noise ratio is low.

We ignored EP Cet because it was not visible in the sky at the optimum time of our long observation campaign. EP Cet looks promising for further study of γ Doradus pulsations. Figure 7.3 shows the 11 observations of the Ca I line at 6122 Å. As expected, the line profile seems to vary with the pulsation. The spike on the right side corresponds to a residual cosmic ray in a single observation.

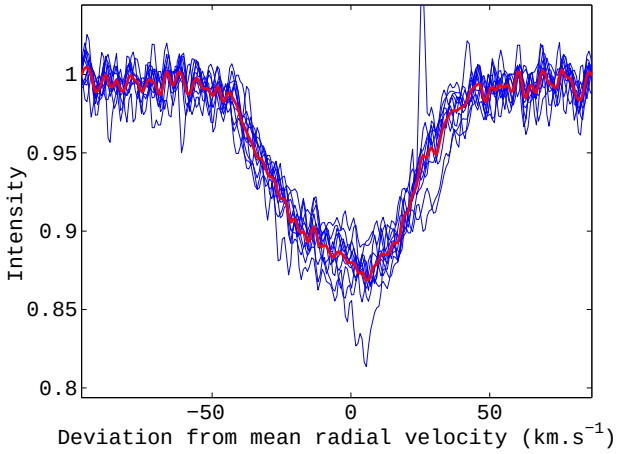

Figure 7.3: Ca I line at 6122 Å of EP Cet. The individual observations are in blue, the mean of all 11 observations is in red.

V769 Mon is fainter than AC Lep. As seen in Figure 7.4, the calcium line at 6122 Å does not show a strong LPV pattern. This could mean that the main pulsation was

poorly sampled, i.e. all observations were taken in the same part of the pulsation cycle, or that the Ca I line is not affected by the pulsation, although this seems unlikely. It could simply mean that the pulsations have a low amplitude, and a cross-correlation, which increases the signal-to-noise ratio, would produce data in which the pulsations could be clearly detected.

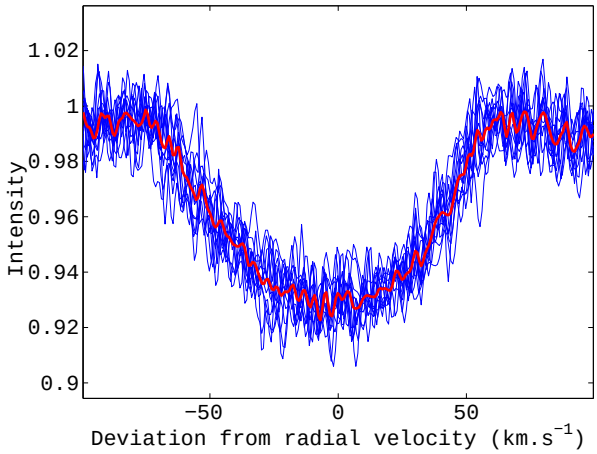

Figure 7.4: Ca I line at 6122 Å of V769 Mon. The individual observations are in blue, the mean of all 13 observations is in red.

NX Lup was observed to follow up on the results of Wright (2008). Only 37 spectra were obtained (Figure 7.5). Considering the faintness of this star, only poor signal-to-noise spectra were obtained, and this new set of data could not contribute significantly to modify the results of Wright (2008). The line profile variations are small and a cross-correlation is absolutely necessary to further analyze this data.

Only two spectra were obtained for IN Lib (Figure 7.6), which is not enough to draw any conclusions on the pulsations of this star. It is brighter than NX Lup and therefore better signal-to-noise has been achieved. It has been chosen as a research target by Emily Brunsden, currently working on her PhD at the University of Canterbury.

7.4 The methods of analysis

The uncertainties in the mode identification cannot be simply listed in a "plus or minus" form. In fact, when uncertain about the value of ℓ, the second best fit often corresponds

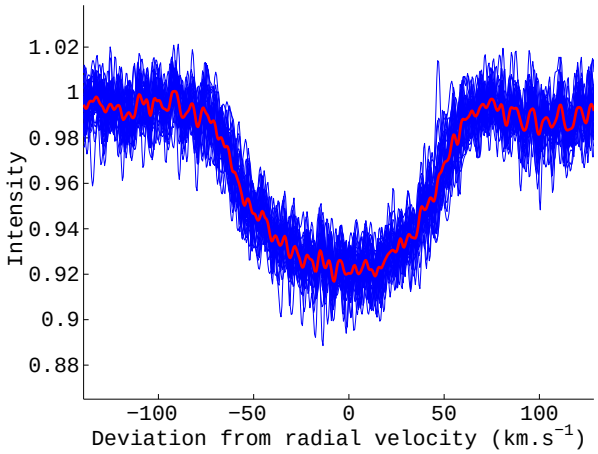

Figure 7.5: Ca I line at 6122 Å of NX Lup. The individual observations are in blue, the mean of all 37 observations is in red.

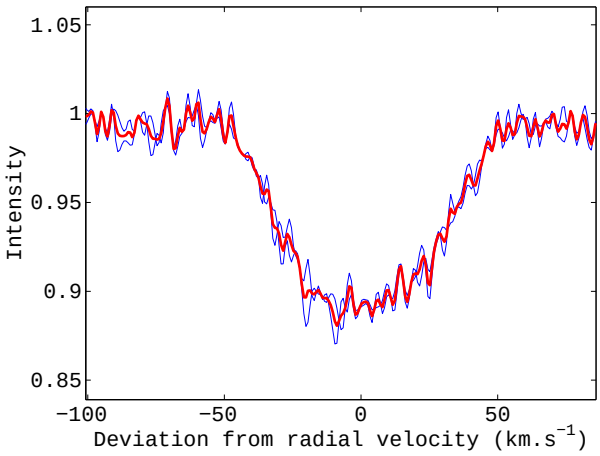

Figure 7.6: Ca I line at 6122 Å of IN Lib. The individual observations are in blue, the mean of the two observations is in red.

to a mode which is not ± 1, but ± 2. For the value of m, the second best fits do not seem correlated to the value of m. This is why in this work, when a strong uncertainty about a mode identification arises, we simply list the second best solution.

For HD 189631, the two identified modes for f_1 and f_4 have a positive m value of $+1$. In these cases the rotational effects become important and should be evaluated to the second order for a better fit, whereas the models used in this study only take the Coriolis force into account which is the first order of rotation. The second order is the centrifugal force. The mode identification of p modes will largely benefit from this improvement of the models as the centrifugal force modifies the local surface gravity and therefore affects vertical movements (dominant in p modes) rather than horizontal ones (dominant in g modes). Also note that for AC Lep the amplitude variation in the wings is always underestimated by the fit.

As has already been noted for the case of the β Cephei star PT Pup, axisymmetric ($m = 0$) modes seem to be difficult to detect when using the FPF method. Synthetic models predict a sharp transition in the phase across the profile which is difficult to observe in real data. It is likely that every mode identification method has a weakness and therefore large spectroscopic data sets should be analyzed using more than one method, in order to rule out the dependency of the results on the method used.

An interesting result from this analysis is that different pulsations observed in the same star can be centred around different radial velocities. For instance, in PT Pup, f_1 is at 26.4 km.s^{-1} and f_2 at 25.6 km.s^{-1}. This phenomenon is observed in every star, thus outlining the uncertainty in the measurement of the radial velocity using the FPF method. This is one of the reasons why a combined mode identification is important as it produces a single coherent set of variables for the target star. It is possible that in the extreme case of PT Pup, the secondary pulsation, being very close to the primary pulsation in frequency space, is affected by the dominant primary, giving a sort of "optical effect". By this we mean that specific sections of the cycle of the secondary pulsation were always observed through the same sections of the primary pulsation. An equal data sampling over not only both frequencies, but also over the beat frequency ($f_1 - f_2 = 0.0805$ d^{-1}), would remove this effect. Once again, more data always solves issues.

Another method of analysis used in this thesis work was the LPAP analysis. A symmetric line profile would produce an average LPAP equal to zero, whereas an asym-

metry towards the blue (shorter wavelengths) will give a negative result, and towards the red (larger wavelengths) a positive result. The average LPAP for our targets are: 4.99 km.s^{-1} for AC Lep and -0.30 km.s^{-1} for HD 189631. With 248 observations and no gaps in the sampling of each identified frequency it is hard to understand why the line profile of AC Lep exhibits such a strong asymmetry. It would be interesting to investigate the value of the mean LPAP for many γ Doradus stars and maybe on some other similar g-mode pulsators like SPB stars. A comparison of the LPAP of many targets would inform us if these deviations from the expected symmetry are dominantly found to be positive or negative. The pulsational nature of the star and the sampling of the data can account for some deviation from a null LPAP, but we expect that overall these deviations would not show a trend across all g mode pulsators. The treatment of the data(reduction process, continuum fitting...), if not done perfectly, will also affect the LPAP.

Chapter 8

Conclusion and future work

We have performed one of the few spectroscopic mode identifications on gravity mode pulsators, only the second one using the FPF method. This is a first step in order to improve our methods of analysis, particularly the FPF method which has been shown to work well for pressure mode pulsators such as β Cephei and δ Scuti stars (Zima, 2006). We are satisfied by the results of the FPF method, but an adaptation of the models used to the conditions encountered in g-mode pulsations can, and should, be done.

In order to test the frequency analysis and mode identification methods, the analysis of a p-mode pulsator, the β Cephei star PT Pup, was performed. This was necessary because the FPF method was found to have difficulties with g-mode pulsators (Zima et al., 2007). Therefore a good understanding of this method was required before using it on data sets from γ Doradus stars. The analysis of PT Pup allowed the identification of two frequencies, a clear primary one at $f_1 = 6.0743 \pm 0.0001$ d^{-1} and a secondary one at $f_2 = 5.9938 \pm 0.0002$ d^{-1}, which had an amplitude lower than the amplitude of the primary by a factor of four. The primary pulsation is identified as a radial mode ($\ell = 0$; $m = 0$) while two modes are possible for the secondary, (2 ; 0) and (1 ; +1).

These results confirm the work of Heynderickx (1992) and prove that the FPF method is efficient and reliable. This is not surprising as β Cephei stars have few strong pulsations which are therefore easy to study. The picture is more complicated when dealing with γ Doradus stars.

The same techniques of frequency analysis and mode identification were used for the analysis of the two γ Doradus targets. Four modes of pulsation have been identified

from the data of HD 189631: $(1\ ;\ +1)$ at $f_1 = 1.6719 \pm 0.0005$ d^{-1}, $(3\ ;\ -2)$ at $f_2 = 1.4200 \pm 0.0005$ d^{-1}, $(2\ ;\ -2)$ at $f_3 = 0.0711 \pm 0.0005$ d^{-1} and $(4\ ;\ +1)$ or $(2\ ;\ -2)$ at $f_4 = 1.8227 \pm 0.0005$ d^{-1}. Two modes were found for AC Lep: $(2\ ;\ -1)$ at $f_1 = 0.7521 \pm 0.0005$ d^{-1} and $(3\ ;\ -3)$ or $(2\ ;\ -2)$ at $f_2 = 1.0864 \pm 0.0007$ d^{-1}.

This research on HD 189631 was done on one of the largest data set ever used for the identification of g-mode pulsations. The frequency determination is robust and we attempted the identification of four modes with a varied range of confidence in our results. This data set will be expanded to check the stability of the frequencies over time and look for other ones. Seismic modelling can be attempted on this target and the group at the university of Canterbury is looking into this. HD 189631 is a good candidate for successful modelling with the determination of n, but also the inclination angle i.

All published results of spectroscopic mode identification in γ Doradus stars, including ours (see Table 1.1) identify low to moderate degree ℓ modes, which is likely due to a selection effect. High ℓ modes have more cancellation and therefore a lower apparent amplitude. All studies tend to choose targets with high amplitudes for an easier analysis. The methods used are also more efficient for low degree modes. Contrary to other publications on mode identification we do not give uncertainty on the modes identified as a range around our result. When fitting synthetic models to our data, the first and second best fits are rarely related. Since the second best fit is independent of the first it needs to be presented separately. For instance, the fourth pulsation of HD 189631 was identified as a $(4\ ;\ +1)$ or $(2\ ;\ -2)$ mode. Quoting a range around our best fit would have been: $(4 \pm 2\ ;\ +1 \pm 3)$. This is very misleading as many modes in this range were clearly excluded. We believe that results using the FPF method should be presented in this way rather than estimating a $\pm$ uncertainty around the best fit.

Not all γ Doradus stars show the same complexity in their Fourier spectrum. Very large data sets are needed for a good analysis. Note that, when working with data sets of equal size, the analysis was easier for HD 189631 than for AC Lep. Better results might have been obtained for AC Lep with hundreds of additional observations as this star seems to be a particularly complicated case. The mode identification is not straight forward so these results should not be considered as conclusive. Comparing them with an independent mode identification based on photometric colour information could reinforce the results.

Future work A future challenge is to produce models which incorporate less assumptions and more complicated physics. This can be done with rotation, semi-convection, overshooting or diffusion. Of these, the effects of rotation on the observation of stellar pulsations are dominant. Townsend (2003) shows that under high rotational velocities photometric ratios cannot be used to find the degree ℓ, and the amplitudes of pulsations are greater in the equatorial region than in the polar regions. Thus rotation is strongly affecting the observable characteristic of the pulsational modes and the models used to identify these modes must be upgraded in the future to incorporate rotation. New models must evaluate rotation effects to the first and second order which correspond respectively to the Coriolis and the centrifugal force. This is a focus of the Christchurch team at the moment. Also, the observed frequencies need to be shifted by the rotation frequency of the star. This shift depends on the value of m. Unfortunately the exact rotation frequency of the star remains unknown as long as the inclination angle i is unknown.

The mode identification of g-mode pulsations requires large spectroscopic data sets. These pulsations often have high-degree modes and photometric data can only identify low degree modes (Breger et al., 1997). Further asteroseismic modelling based on our results may determine the radial wavenumber n and hence much information about the internal structure of these stars. This modelling will be challenging.

Similar research to this work can be carried on using different stars. Many γ Doradus targets have been identified without being further analyzed. In this work, HD 14940 was found to show clear line profile variations, but many other targets are potentially promising. The analysis of their pulsations, possibly done by independent groups, would bring important new information in the field of asteroseismology.

The analysis of large spectroscopic data sets of γ Doradus targets should be done using several spectroscopic mode identification methods in order to study their accuracy. If available, the analysis of photometric data should also be done. Identifying the modes of pulsations in g-mode pulsators is not an easy task and all available resources should be used for it.

References

H. A. Abt and N. I. Morrell. The Relation between Rotational Velocities and Spectral Peculiarities among A-Type Stars. *Astrophysical Journal Supplement*, 99:135–+, July 1995. doi: 10.1086/192182. 101

H. A. Abt, H. Levato, and M. Grosso. Rotational Velocities of B Stars. *The Astrophysical Journal*, 573:359–365, July 2002. doi: 10.1086/340590. 51

C. Aerts. Mode identification of pulsating stars from line-profile variations with the moment method: a more accurate discriminant. *Astronomy and Astrophysics*, 314: 115–122, October 1996. 10

C. Aerts and A. B. Kaye. A Spectroscopic Analysis of the γ Doradus Star HD 207223 = HR 8330. *The Astrophysical Journal*, 553:814–822, June 2001. doi: 10.1086/320973. 13, 15, 128

C. Aerts and K. Krisciunas. Mode identification of the slowly pulsating F0V star V398 Aurigae (9 Aur). *Monthly Notices of the Royal Astronomical Society*, 278:877–882, February 1996. 13, 128

C. Aerts, L. Eyer, and E. Kestens. The discovery of new gamma Doradus stars from the HIPPARCOS mission. *Astronomy and Astrophysics*, 337:790–796, September 1998. 101, 107

C. Aerts, H. Lehmann, M. Briquet, R. Scuflaire, M. A. Dupret, J. De Ridder, and A. Thoul. Spectroscopic mode identification for the beta Cephei star EN (16) Lacertae. *Astronomy and Astrophysics*, 399:639–645, February 2003. doi: 10.1051/0004-6361:20021750. 11, 48, 124

REFERENCES

C. Aerts, J. Cuypers, P. De Cat, M. A. Dupret, J. De Ridder, L. Eyer, R. Scuflaire, and C. Waelkens. Long-term multicolour photometry and high-resolution spectroscopy of the two γ Doradus stars HD 12901 and HD 48501. *Astronomy and Astrophysics*, 415:1079–1088, March 2004a. doi: 10.1051/0004-6361:20034628. 13, 127

C. Aerts, P. De Cat, G. Handler, U. Heiter, L. A. Balona, J. Krzesinski, P. Mathias, H. Lehmann, I. Ilyin, J. De Ridder, S. Dreizler, A. Bruch, I. Traulsen, A. Hoffmann, D. James, E. Romero-Colmenero, T. Maas, M. A. T. Groenewegen, J. H. Telting, K. Uytterhoeven, C. Koen, P. L. Cottrell, J. Bentley, D. J. Wright, and J. Cuypers. Asteroseismology of the β Cephei star ν Eridani - II. Spectroscopic observations and pulsational frequency analysis. *Monthly Notices of the Royal Astronomical Society*, 347:463–470, January 2004b. doi: 10.1111/j.1365-2966.2004.07215.x. 41, 48

C. Aerts, J. Christensen-Dalsgaard, and D. W. Kurtz. Asteroseismology. *Astronomy and astrophysics library*, 2007. 2, 5, 10

C. Aerts, J. Christensen-Dalsgaard, M. Cunha, and D. W. Kurtz. The Current Status of Asteroseismology. *Solar Physics*, 251:3–20, September 2008. doi: 10.1007/s11207-008-9182-z. 1

A. Baglin, M. Auvergne, P. Barge, M. Deleuil, C. Catala, E. Michel, W. Weiss, and The COROT Team. Scientific Objectives for a Minisat: CoRoT. In M. Fridlund, A. Baglin, J. Lochard, & L. Conroy, editor, *ESA Special Publication*, volume 1306 of *ESA Special Publication*, pages 33–+, November 2006. 12

L. A. Balona. Mode identification from line profile variations. *Monthly Notices of the Royal Astronomical Society*, 219:111–129, March 1986. 10, 40

L. A. Balona. Mode Identification from Line Profiles using the Direct Fitting Technique. *Astrophysics and Space Science*, 284:121–124, 2003. 10

L. A. Balona and R. S. Stobie. The effect of radial and non-radial stellar oscillations on the light, colour and velocity variations. *Monthly Notices of the Royal Astronomical Society*, 189:649–658, December 1979. 9

L. A. Balona, T. Böhm, B. H. Foing, K. K. Ghosh, E. Janot-Pacheco, K. Krisciunas, A.-M. Lagrange, W. A. Lawson, S. D. James, J. Baudrand, C. Catala, M. Dreux,

P. Felenbok, and J. B. Hearnshaw. Line profile variations in γ Doradus. *Monthly Notices of the Royal Astronomical Society*, 281:1315–1325, August 1996. 13, 15, 127, 128

S. V. Berdyugina, J. H. Telting, and H. Korhonen. Surface imaging of stellar non-radial pulsations. I. Inversions of simulated data. *Astronomy and Astrophysics*, 406: 273–280, July 2003. doi: 10.1051/0004-6361:20030746. 10

M. Breger, G. Handler, R. Garrido, N. Audard, F. Beichbuchner, W. Zima, M. Paparo, Z.-P. Li, S.-Y. Jiang, Z.-L. Liu, A.-Y. Zhou, H. Pikall, A. Stankov, J. A. Guzik, M. Sperl, J. Krzesinski, W. Ogloza, G. Pajdosz, S. Zola, E. Serkowitsch, P. Reegen, T. Rumpf, and A. Schmalwieser. The variability of a newly discovered γ Doradus star, HD 108100. *Astronomy and Astrophysics*, 324:566–572, August 1997. 13, 137

M. Briquet and C. Aerts. A new version of the moment method, optimized for mode identification in multiperiodic stars. *Astronomy and Astrophysics*, 398:687–696, February 2003. doi: 10.1051/0004-6361:20021683. 10

M. Briquet, T. Morel, A. Thoul, R. Scuflaire, A. Miglio, J. Montalbán, M.-A. Dupret, and C. Aerts. An asteroseismic study of the β Cephei star θ Ophiuchi: constraints on global stellar parameters and core overshooting. *Monthly Notices of the Royal Astronomical Society*, 381:1482–1488, November 2007. doi: 10.1111/j.1365-2966.2007.12142.x. 1

M. Briquet, K. Uytterhoeven, T. Morel, C. Aerts, P. De Cat, P. Mathias, K. Lefever, A. Miglio, E. Poretti, S. Martín-Ruiz, M. Paparó, M. Rainer, F. Carrier, J. Gutiérrez-Soto, J. C. Valtier, J. M. Benkő, Z. Bognár, E. Niemczura, P. J. Amado, J. C. Suárez, A. Moya, C. Rodríguez-López, and R. Garrido. Ground-based observations of the β Cephei CoRoT main target HD 180 642: abundance analysis and mode identification. *Astronomy and Astrophysics*, 506:269–280, October 2009. doi: 10.1051/0004-6361/200912025. 11, 124

H. Bruntt, P. De Cat, and C. Aerts. A spectroscopic study of southern (candidate) γ Doradus stars. II. Detailed abundance analysis and fundamental parameters. *Astronomy and Astrophysics*, 478:487–496, February 2008. doi: 10.1051/0004-6361:20078523. 115

R. Casas, J. C. Suárez, A. Moya, and R. Garrido. A comprehensive asteroseismic modelling of the high-amplitude δ Scuti star RV Arietis. *Astronomy and Astrophysics*, 455:1019–1029, September 2006. doi: 10.1051/0004-6361:20065054. 1

J. Christensen-Dalsgaard. Seismological studies of the sun and other stars. *Advances in Space Research*, 2:11–19, 1982. doi: 10.1016/0273-1177(82)90250-2. 12

J. Christensen-Dalsgaard. *Stellar oscillations, fifth edition.* Institut for Fysik og Astronomi, Aarhus Universitet, 2003. 8

A. W. J. Cousins and P. R. Warren. Variable Stars Observed During the Cape Bright Star Programme. *Monthly Notes of the Astronomical Society of South Africa*, 22: 65–+, 1963. 12

H. Cugier, W. A. Dziembowski, and A. A. Pamyatnykh. Nonadiabatic observables in beta Cephei models. *Astronomy and Astrophysics*, 291:143–154, November 1994. 66, 74

M. S. Cunha, C. Aerts, J. Christensen-Dalsgaard, A. Baglin, L. Bigot, T. M. Brown, C. Catala, O. L. Creevey, A. Domiciano de Souza, P. Eggenberger, P. J. V. Garcia, F. Grundahl, P. Kervella, D. W. Kurtz, P. Mathias, A. Miglio, M. J. P. F. G. Monteiro, G. Perrin, F. P. Pijpers, D. Pourbaix, A. Quirrenbach, K. Rousselet-Perraut, T. C. Teixeira, F. Thévenin, and M. J. Thompson. Asteroseismology and interferometry. *The Astronomy and Astrophysics Review*, 14:217–360, November 2007. doi: 10.1007/s00159-007-0007-0. 5, 8, 9

J. Daszyńska-Daszkiewicz, W. A. Dziembowski, and A. A. Pamyatnykh. Constraints on stellar convection from multi-colour photometry of delta Scuti stars. *Astronomy and Astrophysics*, 407:999–1006, September 2003. doi: 10.1051/0004-6361:20030947. 10

P. De Cat, L. Eyer, J. Cuypers, C. Aerts, B. Vandenbussche, K. Uytterhoeven, K. Reyniers, K. Kolenberg, M. Groenewegen, G. Raskin, T. Maas, and S. Jankov. A spectroscopic study of southern (candidate) γ Doradus stars. I. Time series analysis. *Astronomy and Astrophysics*, 449:281–292, April 2006. doi: 10.1051/0004-6361: 20053655. 12, 103, 104

P. De Cat, D. J. Wright, K. R. Pollard, F. Maisonneuve, P. M. Kilmartin, H. Lehmann, S. Yang, E. Kambe, S. Saesen, F. Carrier, D. Mkrtichian, L. Mantegazza, M. Rainer, E. Poretti, D. Laney, and J. N. Fu. Towards asteroseismology of main-sequence g-mode pulsators: spectroscopic multi-site campaigns for slowly pulsating B stars and γ Doradus stars. In J. A. Guzik & P. A. Bradley, editor, *American Institute of Physics Conference Series*, volume 1170 of *American Institute of Physics Conference Series*, pages 480–482, September 2009. doi: 10.1063/1.3246548. 12

J. De Ridder, J. H. Telting, L. A. Balona, G. Handler, M. Briquet, J. Daszyńska-Daszkiewicz, K. Lefever, A. J. Korn, U. Heiter, and C. Aerts. Asteroseismology of the β Cephei star ν Eridani - III. Extended frequency analysis and mode identification. *Monthly Notices of the Royal Astronomical Society*, 351:324–332, June 2004. doi: 10.1111/j.1365-2966.2004.07791.x. 11, 124

M. Desmet, M. Briquet, A. Thoul, W. Zima, P. De Cat, G. Handler, I. Ilyin, E. Kambe, J. Krzesinski, H. Lehmann, S. Masuda, P. Mathias, D. E. Mkrtichian, J. Telting, K. Uytterhoeven, S. L. S. Yang, and C. Aerts. An asteroseismic study of the β Cephei star 12 Lacertae: multisite spectroscopic observations, mode identification and seismic modelling. *Monthly Notices of the Royal Astronomical Society*, 396: 1460–1472, July 2009. doi: 10.1111/j.1365-2966.2009.14790.x. 11, 124

M. Duflot, P. Figon, and N. Meyssonnier. Vitesses radiales. Catalogue WEB: Wilson Evans Batten. Subtittle: Radial velocities: The Wilson-Evans-Batten catalogue. *Astronomy and Astrophysics Supplement*, 114:269–+, December 1995. 80, 103

M.-A. Dupret, J. De Ridder, P. De Cat, C. Aerts, R. Scuflaire, A. Noels, and A. Thoul. A photometric mode identification method, including an improved non-adiabatic treatment of the atmosphere. *Astronomy and Astrophysics*, 398:677–685, February 2003. doi: 10.1051/0004-6361:20021679. 10

M.-A. Dupret, A. Grigahcène, R. Garrido, J. De Ridder, R. Scuflaire, and M. Gabriel. Time-dependent convection seismic study of five γ Doradus stars. *Monthly Notices of the Royal Astronomical Society*, 360:1143–1152, July 2005. doi: 10.1111/j.1365-2966.2005.09114.x. 9

W. Dziembowski. Light and radial velocity variations in a nonradially oscillating star. *Acta Astronomica*, 27:203–211, 1977. 9

W. A. Dziembowski and A. A. Pamiatnykh. The opacity mechanism in B-type stars. I - Unstable modes in Beta Cephei star models. *Monthly Notices of the Royal Astronomical Society*, 262:204–212, May 1993. 8

M. Gabriel. Solar oscillations : theory. *Bulletin of the Astronomical Society of India*, 24:233–+, June 1996. 9

R. L. Gilliland, T. M. Brown, J. Christensen-Dalsgaard, H. Kjeldsen, C. Aerts, T. Appourchaux, S. Basu, T. R. Bedding, W. J. Chaplin, M. S. Cunha, P. De Cat, J. De Ridder, J. A. Guzik, G. Handler, S. Kawaler, L. Kiss, K. Kolenberg, D. W. Kurtz, T. S. Metcalfe, M. J. P. F. G. Monteiro, R. Szabó, T. Arentoft, L. Balona, J. Debosscher, Y. P. Elsworth, P.-O. Quirion, D. Stello, J. C. Suárez, W. J. Borucki, J. M. Jenkins, D. Koch, Y. Kondo, D. W. Latham, J. F. Rowe, and J. H. Steffen. Kepler Asteroseismology Program: Introduction and First Results. *Publications of the Astronomical Society of the Pacific*, 122:131–143, February 2010. doi: 10.1086/650399. 13

G. A. Gontcharov. Pulkovo compilation of radial velocities for 35495 stars in a common system. *Astronomy Letters*, 32:759–771, November 2006. doi: 10.1134/S1063773706110065. 51, 80

D. F. Gray. *Lectures on spectral-line analysis: F,G, and K stars.* Arva: Ontario Gray, 1988. 37, 104

D. F. Gray. *The Observation and Analysis of Stellar Photospheres, 3rd Edition.* Cambridge University Press, September 2005. 34, 36, 103

A. Grigahcène, V. Antoci, L. Balona, G. Catanzaro, J. Daszyńska-Daszkiewicz, J. A. Guzik, G. Handler, G. Houdek, D. W. Kurtz, M. Marconi, M. J. P. F. G. Monteiro, A. Moya, V. Ripepi, J.-C. Suárez, K. Uytterhoeven, W. J. Borucki, T. M. Brown, J. Christensen-Dalsgaard, R. L. Gilliland, J. M. Jenkins, H. Kjeldsen, D. Koch, S. Bernabei, P. Bradley, M. Breger, M. Di Criscienzo, M.-A. Dupret, R. A. García, A. García Hernández, J. Jackiewicz, A. Kaiser, H. Lehmann, S. Martín-Ruiz, P. Mathias, J. Molenda-Żakowicz, J. M. Nemec, J. Nuspl, M. Paparó, M. Roth,

R. Szabó, M. D. Suran, and R. Ventura. Hybrid γ Doradus-δ Scuti Pulsators: New Insights into the Physics of the Oscillations from Kepler Observations. *The Astrophysical Journal Letters*, 713:L192–L197, April 2010. doi: 10.1088/2041-8205/713/2/L192. 13

J. A. Guzik, A. B. Kaye, P. A. Bradley, A. N. Cox, and C. Neuforge. Driving the Gravity-Mode Pulsations in γ Doradus Variables. *The Astrophysical Journal*, 542: L57–L60, October 2000. doi: 10.1086/312908. 9

D. S. Hall. Variable Stars in the Hertzprung-Russell Diagram. In G. W. Henry & J. A. Eaton, editor, *Robotic Telescopes. Current Capabilities, Present Developments, and Future Prospects for Automated Astronomy*, volume 79 of *Astronomical Society of the Pacific Conference Series*, pages 65–+, 1995. 12

G. Handler. The domain of γ Doradus variables in the Hertzsprung-Russell diagram. *Monthly Notices of the Royal Astronomical Society*, 309:L19–L23, October 1999. doi: 10.1046/j.1365-8711.1999.03005.x. 77, 82, 92, 99, 101, 107, 126

G. Handler. Asteroseismology of Delta Scuti and Gamma Doradus Stars. *Journal of Astrophysics and Astronomy*, 26:241–+, June 2005. doi: 10.1007/BF02702332. 12

G. Handler. Confirmation of simultaneous p and g mode excitation in HD 8801 and γ Peg from time-resolved multicolour photometry of six candidate 'hybrid' pulsators. *Monthly Notices of the Royal Astronomical Society*, 398:1339–1351, September 2009. doi: 10.1111/j.1365-2966.2009.15005.x. 12

G. Handler and R. R. Shobbrook. On the relationship between the δ Scuti and γ Doradus pulsators. *Monthly Notices of the Royal Astronomical Society*, 333:251–262, June 2002. doi: 10.1046/j.1365-8711.2002.05401.x. 77, 82, 107, 129

G. Handler, L. A. Balona, R. R. Shobbrook, C. Koen, A. Bruch, E. Romero-Colmenero, A. A. Pamyatnykh, B. Willems, L. Eyer, D. J. James, and T. Maas. Discovery and analysis of p-mode and g-mode oscillations in the A-type primary of the eccentric binary HD 209295*. *Monthly Notices of the Royal Astronomical Society*, 333:262–279, June 2002. doi: 10.1046/j.1365-8711.2002.05295.x. 13, 15, 127, 128

REFERENCES

G. Handler, R. R. Shobbrook, F. F. Vuthela, L. A. Balona, F. Rodler, and T. Tshenye. Asteroseismological studies of three β Cephei stars: IL Vel, V433 Car and KZ Mus. *Monthly Notices of the Royal Astronomical Society*, 341:1005–1019, May 2003. doi: 10.1046/j.1365-8711.2003.06487.x. 1

G. Handler, R. R. Shobbrook, M. Jerzykiewicz, K. Krisciunas, T. Tshenye, E. Rodríguez, V. Costa, A.-Y. Zhou, R. Medupe, W. M. Phorah, R. Garrido, P. J. Amado, M. Paparó, D. Zsuffa, L. Ramokgali, R. Crowe, N. Purves, R. Avila, R. Knight, E. Brassfield, P. M. Kilmartin, and P. L. Cottrell. Asteroseismology of the β Cephei star ν Eridani - I. Photometric observations and pulsational frequency analysis. *Monthly Notices of the Royal Astronomical Society*, 347:454–462, January 2004. doi: 10.1111/j.1365-2966.2004.07214.x. 8

G. Handler, M. Jerzykiewicz, E. Rodríguez, K. Uytterhoeven, P. J. Amado, T. N. Dorokhova, N. I. Dorokhov, E. Poretti, J.-P. Sareyan, L. Parrao, D. Lorenz, D. Zsuffa, R. Drummond, J. Daszyńska-Daszkiewicz, T. Verhoelst, J. De Ridder, B. Acke, P.-O. Bourge, A. I. Movchan, R. Garrido, M. Paparó, T. Sahin, V. Antoci, S. N. Udovichenko, K. Csorba, R. Crowe, B. Berkey, S. Stewart, D. Terry, D. E. Mkrtichian, and C. Aerts. Asteroseismology of the β Cephei star 12 (DD) Lacertae: photometric observations, pulsational frequency analysis and mode identification. *Monthly Notices of the Royal Astronomical Society*, 365:327–338, January 2006. doi: 10.1111/j.1365-2966.2005.09728.x. 8, 11, 124

M. Hareter, P. Reegen, A. Miglio, J. Montalban, A. Kaiser, I. Dekany, E. Guenther, E. Poretti, P. Mathias, and W. Weiss. Gamma Dor and Gamma Dor - Delta Sct Hybrid Stars In The CoRoT LRa01. *ArXiv e-prints*, July 2010. 13

A. P. Hatzes. Spectral line profile variations in the gamma Doradus variable HD 164615: non-radial pulsations versus star-spots. *Monthly Notices of the Royal Astronomical Society*, 299:403–409, September 1998. doi: 10.1046/j.1365-8711.1998.01776.x. 14, 15, 127, 128

J. B. Hearnshaw. Astronomy in New Zealand. *Organizations and Strategies in Astronomy, Vol. 7*, 335:63–86, January 2006. 18

J. B. Hearnshaw, S. I. Barnes, G. M. Kershaw, N. Frost, G. Graham, R. Ritchie, and G. R. Nankivell. The Hercules Échelle Spectrograph at Mt. John. *Experimental Astronomy*, 13:59–76, March 2002. doi: 10.1023/A:1023770225275. 19

J. B. Hearnshaw, S. I. Barnes, N. Frost, G. M. Kershaw, G. Graham, and G. R. Nankivell. HERCULES: A High-resolution Spectrograph for Small to Medium-sized Telescopes. In S. Ikeuchi, J. Hearnshaw, & T. Hanawa, editor, *The Proceedings of the IAU 8th Asian-Pacific Regional Meeting, Volume I*, volume 289 of *Astronomical Society of the Pacific Conference Series*, pages 11–16, May 2003. 19

G. W. Henry, F. C. Fekel, and S. M. Henry. Photometry and Spectroscopy of 11 γ Doradus Stars. *The Astronomical Journal*, 133:1421–1440, April 2007. doi: 10.1086/511820. 103, 104, 107, 108, 115, 116, 122, 126

D. Heynderickx. A photometric study of Beta Cephei stars. I - Frequency analyses. *Astronomy and Astrophysics Supplement Series*, 96:207–254, December 1992. 54, 55, 57, 66, 74, 123, 124, 135

D. Heynderickx, C. Waelkens, and P. Smeyers. A photometric study of β Cephei stars. II. Determination of the degrees L of pulsation modes. *Astronomy and Astrophysics Supplement Series*, 105:447–480, June 1994. 10, 66, 69, 70, 74, 124

G. Houdek, N. J. Balmforth, J. Christensen-Dalsgaard, and D. O. Gough. On the Location of the Instability Strip. In A. Gimenez, E. F. Guinan, & B. Montesinos, editor, *Stellar Structure: Theory and Test of Connective Energy Transport*, volume 173 of *Astronomical Society of the Pacific Conference Series*, pages 317–+, 1999. 12

S. Hubrig, M. Briquet, P. De Cat, M. Schöller, T. Morel, and I. Ilyin. New magnetic field measurements of β Cephei stars and slowly pulsating B stars. *Astronomische Nachrichten*, 330:317–+, April 2009. doi: 10.1002/asna.200811187. 47

S. Jankov, P. Mathias, E. Chapellier, J.-M. Le Contel, and J.-P. Sareyan. Non-radial pulsations in the γ Doradus star HD 195068. *Astronomy and Astrophysics*, 453: 1041–1050, July 2006. doi: 10.1051/0004-6361:20053117. 14, 127, 128

J. Kaler. *The Cambridge Encyclopedia of Stars*. Cambridge University Press, March 2006. vii, 3

T. Kallinger, P. Reegen, and W. W. Weiss. A heuristic derivation of the uncertainty for frequency determination in time series data. *Astronomy and Astrophysics*, 481: 571–574, April 2008. doi: 10.1051/0004-6361:20077559. 40

A. Kanaan, A. Nitta, D. E. Winget, S. O. Kepler, M. H. Montgomery, T. S. Metcalfe, H. Oliveira, L. Fraga, A. F. M. da Costa, J. E. S. Costa, B. G. Castanheira, O. Giovannini, R. E. Nather, A. Mukadam, S. D. Kawaler, M. S. O'Brien, M. D. Reed, S. J. Kleinman, J. L. Provencal, T. K. Watson, D. Kilkenny, D. J. Sullivan, T. Sullivan, B. Shobbrook, X. J. Jiang, B. N. Ashoka, S. Seetha, E. Leibowitz, P. Ibbetson, H. Mendelson, E. G. Meištas, R. Kalytis, D. Ališauskas, D. O'Donoghue, D. Buckley, P. Martinez, F. van Wyk, R. Stobie, F. Marang, L. van Zyl, W. Ogloza, J. Krzesinski, S. Zola, P. Moskalik, M. Breger, A. Stankov, R. Silvotti, A. Piccioni, G. Vauclair, N. Dolez, M. Chevreton, J. Deetjen, S. Dreizler, S. Schuh, J. M. Gonzalez Perez, R. Østensen, A. Ulla, M. Manteiga, O. Suarez, M. R. Burleigh, and M. A. Barstow. Whole Earth Telescope observations of BPM 37093: A seismological test of crystallization theory in white dwarfs. *Astronomy and Astrophysics*, 432:219–224, March 2005. doi: 10.1051/0004-6361:20041125. 2

A. Kaufer, O. Stahl, S. Tubbesing, P. Norregaard, G. Avila, P. Francois, L. Pasquini, and A. Pizzella. Performance report on FEROS, the new fiber-linked echelle spectrograph at the ESO 1.52-m telescope. In M. Iye & A. F. Moorwood, editor, *Society of Photo-Optical Instrumentation Engineers (SPIE) Conference Series*, volume 4008 of *Society of Photo-Optical Instrumentation Engineers (SPIE) Conference Series*, pages 459–466, August 2000. 21

A. B. Kaye, G. Handler, K. Krisciunas, E. Poretti, and F. M. Zerbi. Gamma Doradus Stars: Defining a New Class of Pulsating Variables. *The Publications of the Astronomical Society of the Pacific*, 111:840–844, July 1999. doi: 10.1086/316399. 11, 12

E. V. Kazarovets, N. N. Samus, and O. V. Durlevich. The 75th Name-List of Variable Stars. *Information Bulletin on Variable Stars*, 4870:1–+, March 2000. 101, 107

C. Koen and L. Eyer. New periodic variables from the Hipparcos epoch photometry. *Monthly Notices of the Royal Astronomical Society*, 331:45–59, March 2002. doi: 10.1046/j.1365-8711.2002.05150.x. 54

K. Krisciunas. The sign of four: a new class of cool non-radially pulsating stars? *Comments on Astrophysics*, 17:213–226, 1994. 12

P. Ledoux. The Nonradial Oscillations of Gaseous Stars and the Problem of Beta Canis Majoris. *The Astrophysical Journal*, 114:373–+, November 1951. doi: 10.1086/145477. 95

L. Lefèvre, S. V. Marchenko, A. F. J. Moffat, and A. Acker. A systematic study of variability among OB-stars based on HIPPARCOS photometry. *Astronomy and Astrophysics*, 507:1141–1201, November 2009. doi: 10.1051/0004-6361/200912304. 47, 54

P. Lenz, A. A. Pamyatnykh, M. Breger, and V. Antoci. An asteroseismic study of the δ Scuti star 44 Tauri. *Astronomy and Astrophysics*, 478:855–863, February 2008. doi: 10.1051/0004-6361:20078376. 1

F. Maisonneuve, K. R. Pollard, P. L. Cottrell, P. M. Kilmartin, D. J. Wright, and P. De Cat. Spectroscopic mode identification of main-sequence non-radially pulsating stars. *Astrophysics and Space Science*, 328:105–108, July 2010. doi: 10.1007/s10509-009-0219-z. 12

L. Mantegazza. Mode Detection from Line-Profile Variations. In M. Breger & M. Montgomery, editor, *Delta Scuti and Related Stars*, volume 210 of *Astronomical Society of the Pacific Conference Series*, pages 138–+, 2000. 10, 16, 41, 43

L. Mantegazza, E. Poretti, and F. M. Zerbi. Unusual Variability among Early F-Type Stars - HD224638 and HD224945. *Monthly Notices of the Royal Astronomical Society*, 270:439–+, September 1994. 12

P. Mathias, J.-M. Le Contel, E. Chapellier, S. Jankov, J.-P. Sareyan, E. Poretti, R. Garrido, E. Rodríguez, A. Arellano Ferro, M. Alvarez, L. Parrao, J. Peña, L. Eyer, C. Aerts, P. De Cat, W. W. Weiss, and A. Zhou. Multi-site, multi-technique survey of γ Doradus candidates. I. Spectroscopic results for 59 stars. *Astronomy and Astrophysics*, 417:189–199, April 2004. doi: 10.1051/0004-6361:20034503. 103

M. Mayor, F. Pepe, D. Queloz, F. Bouchy, G. Rupprecht, G. Lo Curto, G. Avila, W. Benz, J.-L. Bertaux, X. Bonfils, T. Dall, H. Dekker, B. Delabre, W. Eckert, M. Fleury, A. Gilliotte, D. Gojak, J. C. Guzman, D. Kohler, J.-L. Lizon, A. Longinotti, C. Lovis, D. Megevand, L. Pasquini, J. Reyes, J.-P. Sivan, D. Sosnowska, R. Soto, S. Udry, A. van Kesteren, L. Weber, and U. Weilenmann. Setting New Standards with HARPS. *The Messenger*, 114:20–24, December 2003. 19

A. Mazumdar, M. Briquet, M. Desmet, and C. Aerts. An asteroseismic study of the β Cephei star β Canis Majoris. *Astronomy and Astrophysics*, 459:589–596, November 2006. doi: 10.1051/0004-6361:20064980. 1

A. Miglio, J. Montalbán, A. Noels, and P. Eggenberger. Probing the properties of convective cores through g modes: high-order g modes in SPB and γ Doradus stars. *Monthly Notices of the Royal Astronomical Society*, 386:1487–1502, May 2008. doi: 10.1111/j.1365-2966.2008.13112.x. 13

M. H. Montgomery and D. Odonoghue. A derivation of the errors for least squares fitting to time series data. *Delta Scuti Star Newsletter*, 13:28–+, July 1999. 40

P. Moskalik and W. A. Dziembowski. New opacities and the origin of the Beta Cephei pulsation. *Astronomy and Astrophysics*, 256:L5–L8, March 1992. 8

A. Moya, J. C. Suárez, P. J. Amado, S. Martin-Ruíz, and R. Garrido. Frequency ratio method for seismic modeling of γ Doradus stars. *Astronomy and Astrophysics*, 432: 189–198, March 2005. doi: 10.1051/0004-6361:20041752. 13

R. Napiwotzki, D. Schoenberner, and V. Wenske. On the determination of effective temperature and surface gravity of B, A, and F stars using Stromgren UVBY beta photometry. *Astronomy and Astrophysics*, 268:653–666, February 1993. 47

C. Neiner, H. F. Henrichs, M. Floquet, Y. Frémat, O. Preuss, A.-M. Hubert, V. C. Geers, A. H. Tijani, J. S. Nichols, and S. Jankov. Rotation, pulsations and magnetic field in ¡ASTROBJ¿V 2052 Ophiuchi¡/ASTROBJ¿: A new He-strong star. *Astronomy and Astrophysics*, 411:565–579, December 2003. doi: 10.1051/0004-6361: 20031342. 11

M. A. C. Perryman and ESA. The HIPPARCOS and TYCHO catalogues. Astrometric and photometric star catalogues derived from the ESA HIPPARCOS Space Astrometry Mission. *ESA Special Publication*, 1200, 1997. 78, 101, 107

K. R. Pollard. A Review Of γ Doradus Variables. In J. A. Guzik & P. A. Bradley, editor, *American Institute of Physics Conference Series*, volume 1170 of *American Institute of Physics Conference Series*, pages 455–466, September 2009. doi: 10.1063/1.3246543. 12

K. R. Pollard, D. J. Wright, P. L. Cottrell, R. M. Woollands, D. J. Ramm, and T. Böhm. Coordinated observational campaigns for non-radially pulsating objects. *Communications in Asteroseismology*, 150:133–+, June 2007. doi: 10.1553/cia150s133. 19

K. R. Pollard, D. J. Wright, W. Zima, P. L. Cottrell, and P. De Cat. High-resolution spectroscopy and mode identification in non-radially pulsating stars. *Communications in Asteroseismology*, 157:118–123, December 2008. 14

M. Rainer. *Laurea Thesis.* PhD thesis, Universitá degli Studi di Milano, 2003. 23

P. Reegen. SigSpec. I. Frequency- and phase-resolved significance in Fourier space. *Astronomy and Astrophysics*, 467:1353–1371, June 2007. doi: 10.1051/0004-6361:20066597. 39

E. Rodríguez, P. J. Amado, J. C. Suárez, A. Moya, M. A. Dupret, E. Poretti, A. Grigahcène, V. Costa, and M. J. López-González. The frequency ratio method and the new multiperiodic γ Doradus star HD 218427. *Astronomy and Astrophysics*, 450:715–723, May 2006a. doi: 10.1051/0004-6361:20053942. 13

E. Rodríguez, V. Costa, A.-Y. Zhou, A. Grigahcène, M. A. Dupret, J. C. Suárez, A. Moya, M. J. López-González, J.-Y. Wei, and Y. Fan. Asteroseismology of the new multiperiodic γ Dor variable HD 239276. *Astronomy and Astrophysics*, 456:261–268, September 2006b. doi: 10.1051/0004-6361:20065211. 1, 13

F. Royer, S. Grenier, M.-O. Baylac, A. E. Gómez, and J. Zorec. Rotational velocities of A-type stars in the northern hemisphere. II. Measurement of v sin i. *Astronomy and Astrophysics*, 393:897–911, October 2002. doi: 10.1051/0004-6361:20020943. 103

C. Schrijvers and J. H. Telting. Line-profile variations due to adiabatic non-radial pulsations in rotating stars. IV. The effects of intrinsic profile variations on the IPS diagnostics. *Astronomy and Astrophysics*, 342:453–463, February 1999. 10

C. Schrijvers, J. H. Telting, C. Aerts, E. Ruymaekers, and H. F. Henrichs. Line-profile variations due to adiabatic non-radial pulsations in rotating stars. I. Observable characteristics of spheroidal modes. *Astronomy and Astrophysics Supplement Series*, 121:343–368, February 1997. doi: 10.1051/aas:1997321. 10

R. R. Shobbrook. Short-Period Variability of Some Early B-Stars. *Monthly Notices of the Royal Astronomical Society*, 196:129–+, July 1981. 47

J. Skuljan. HRSP - A dedicated echelle reduction software package for Hercules. In D. W. Kurtz & K. R. Pollard, editor, *IAU Colloq. 193: Variable Stars in the Local Group*, volume 310 of *Astronomical Society of the Pacific Conference Series*, pages 575–+, May 2004. 23

A. Stankov and G. Handler. Catalog of Galactic β Cephei Stars. *The Astrophysical Journal Supplement Series*, 158:193–216, June 2005. doi: 10.1086/429408. 8, 47

J. C. Suárez, A. Moya, S. Martín-Ruíz, P. J. Amado, A. Grigahcène, and R. Garrido. Frequency ratio method for seismic modelling of γ Doradus stars. II. The role of rotation. *Astronomy and Astrophysics*, 443:271–282, November 2005. doi: 10.1051/0004-6361:20053114. 13

J. H. Telting and C. Schrijvers. Line-profile variations of non-radial adiabatic pulsations of rotating stars. II. The diagnostic value of amplitude and phase diagrams derived from time series of spectra. *Astronomy and Astrophysics*, 317:723–741, February 1997a. vii, 6

J. H. Telting and C. Schrijvers. Line-profile variations of non-radial adiabatic pulsations of rotating stars. III. On the alleged misidentification of tesseral modes. *Astronomy and Astrophysics*, 317:742–748, February 1997b. 10

J. H. Telting, C. Schrijvers, I. V. Ilyin, K. Uytterhoeven, J. De Ridder, C. Aerts, and H. F. Henrichs. A high-resolution spectroscopy survey of β Cephei pulsations in bright stars. *Astronomy and Astrophysics*, 452:945–953, June 2006. doi: 10.1051/0004-6361:20054730. 48

R. H. D. Townsend. Asymptotic expressions for the angular dependence of low-frequency pulsation modes in rotating stars. *Monthly Notices of the Royal Astronomical Society*, 340:1020–1030, April 2003. doi: 10.1046/j.1365-8711.2003.06379.x. 13, 137

R. H. D. Townsend. Influence of the Coriolis force on the instability of slowly pulsating B stars. *Monthly Notices of the Royal Astronomical Society*, 360:465–476, June 2005. doi: 10.1111/j.1365-2966.2005.09002.x. 13

K. Uytterhoeven, P. Mathias, E. Poretti, M. Rainer, S. Martín-Ruiz, E. Rodríguez, P. J. Amado, D. Le Contel, S. Jankov, E. Niemczura, K. R. Pollard, E. Brunsden, M. Paparó, V. Costa, J.-C. Valtier, R. Garrido, J. C. Suárez, P. M. Kilmartin, E. Chapellier, C. Rodríguez-López, A. J. Marin, F. J. Aceituno, V. Casanova, A. Rolland, and I. Olivares. The γ Doradus CoRoT target HD 49434. I. Results from the ground-based campaign. *Astronomy and Astrophysics*, 489:1213–1224, October 2008a. doi: 10.1051/0004-6361:200809992. 13, 14, 127, 128

K. Uytterhoeven, E. Poretti, M. Rainer, L. Mantegazza, W. Zima, C. Aerts, T. Morel, A. Miglio, K. Lefever, P. J. Amado, S. Martín-Ruiz, P. Mathias, J. C. Valtier, M. Paparó, J. M. Benkö, and the CoRoT/SWG Ground-based Observations Working Group. Close-up of primary and secondary asteroseismic CoRoT targets and the ground-based follow-up observations. *Journal of Physics Conference Series*, 118(1): 012077–+, October 2008b. doi: 10.1088/1742-6596/118/1/012077. 12

P. B. Warner, A. B. Kaye, and J. A. Guzik. A Theoretical γ Doradus Instability Strip. *The Astrophysical Journal*, 593:1049–1055, August 2003. doi: 10.1086/376727. 9

R. D. Watson. Contributing factors to flux changes in nonradial stellar pulsations. *Astrophysics and Space Science*, 140:255–290, January 1988. doi: 10.1007/BF00638984. 9

S. Wolff and T. Simon. The Angular Momentum of Main Sequence Stars and Its Relation to Stellar Activity. *Publications of the Astronomical Society of the Pacific*, 109:759–775, July 1997. doi: 10.1086/133942. 103

REFERENCES

D. Wright. *Spectroscopic Mode Identification in a Sample of Non-Radially Pulsating Stars.* PhD thesis, University of Canterbury, New Zealand, 2008. vii, 5, 7, 11, 14, 15, 25, 29, 34, 48, 103, 124, 127, 128, 130

D. J. Wright, P. De Cat, K. R. Pollard, F. Maisonneuve, P. M. Kilmartin, J. H. Telting, E. Kambe, E. Poretti, H. Lehmann, S. Yang, D. Mkrtichian, D. Laney, and J. N. Fu. Results from Classification Observations and a Multi-site Campaign on γ Doradus and SPB Type Stars. In J. A. Guzik & P. A. Bradley, editor, *American Institute of Physics Conference Series*, volume 1170 of *American Institute of Physics Conference Series*, pages 467–473, September 2009. doi: 10.1063/1.3246544. 12

F. M. Zerbi, E. Rodríguez, R. Garrido, S. Martín, K. Akan, K. Luedeke, V. Keskin, C. Ibanoglu, S. Evren, Z. Tunca, R. Pekunlu, M. Paparo, J. Nuspl, K. Krisciunas, and S. Y. Jiang. The Gamma DOR variable HD 164615 - Results from a multisite photometric campaign. *Monthly Notices of the Royal Astronomical Society*, 292: 43–+, November 1997. 13

F. M. Zerbi, E. Rodríguez, R. Garrido, S. Martín, A. Arellano Ferro, J. P. Sareyan, K. Krisciunas, M. C. Akan, S. Evren, C. Ibanoğlu, V. Keskin, R. Pekunlu, Z. Tunca, K. Luedeke, M. Paparo, J. Nuspl, and G. Guerrero. The gamma DOR variable HR 8799: results from a multisite campaign. *Monthly Notices of the Royal Astronomical Society*, 303:275–283, February 1999. doi: 10.1046/j.1365-8711.1999.02209.x. 13

W. Zima. A new method for the spectroscopic identification of stellar non-radial pulsation modes. I. The method and numerical tests. *Astronomy and Astrophysics*, 455: 227–234, August 2006. doi: 10.1051/0004-6361:20064876. 4, 10, 16, 135

W. Zima. FAMIAS User Manual. *Communications in Asteroseismology*, 155:17–121, October 2008. 5, 39

W. Zima, P. De Cat, and C. Aerts. Mode identification of multi-periodic Slowly Pulsating B-stars: results and problems. *Communications in Asteroseismology*, 150:189–+, June 2007. doi: 10.1553/cia150s189. 10, 135

Appendix A

Complete data sets listed by Julian Date (JD).

This appendix presents the complete data sets for each star in the form of tables. The Julian dates given are JD-2450000. The observations of PT Pup, which were all taken with HERCULES at MJUO with an exposure time varying from five to ten minutes, are listed in Table A.1. The observations of HD 189631, collected with HARPS and FEROS at La Silla, Chile, and HERCULES at MJUO, New Zealand, are listed in Tables A.2, A.3 and A.4. The instrument used is indicated in brackets for each data point. Observations were taken with an exposure time varying from five to ten minutes, according to the performance of the instrument. For AC Lep, all the data was collected with HERCULES at MJUO in New Zealand, with an exposure time of 10 minutes. The observations are listed in Table A.5.

Table A.1: Mean Julian date of observations of PT Pup.

4440.953	4778.054	4817.932	4829.044	4841.976	4845.181	4849.069
4441.082	4778.062	4817.941	4829.142	4842.002	4845.904	4849.077
4441.920	4778.095	4817.968	4829.151	4842.010	4845.916	4849.106
4442.001	4778.103	4817.977	4830.033	4842.039	4845.956	4849.114
4442.040	4778.131	4818.041	4830.041	4842.047	4845.965	4849.142
4442.067	4778.140	4818.049	4830.076	4842.076	4845.994	4849.151
4442.108	4778.168	4818.075	4830.084	4842.084	4846.003	4849.159
4442.120	4778.176	4818.083	4830.149	4842.093	4846.041	4867.913
4442.134	4780.100	4821.925	4830.158	4842.137	4846.050	4867.921
4442.919	4780.108	4821.933	4838.979	4842.145	4846.059	4867.983
4443.015	4780.136	4821.964	4838.987	4844.939	4846.090	4867.992
4443.064	4780.144	4821.972	4839.022	4844.948	4846.904	4868.000
4443.093	4780.170	4822.003	4839.040	4844.978	4846.912	4868.009
4443.118	4780.179	4822.011	4841.003	4844.986	4847.033	4868.017
4443.133	4780.976	4822.041	4841.011	4845.017	4847.044	4868.044
4541.915	4780.984	4822.050	4841.068	4845.026	4848.903	4868.053
4542.897	4781.015	4822.080	4841.113	4845.059	4848.912	4870.929
4542.962	4781.024	4822.089	4841.122	4845.068	4848.955	4870.937
4777.100	4781.061	4822.123	4841.148	4845.097	4848.962	4870.984
4777.982	4781.070	4822.132	4841.156	4845.106	4848.991	4870.993
4777.990	4781.108	4822.162	4841.932	4845.136	4848.999	4871.001
4778.017	4781.117	4829.026	4841.940	4845.144	4849.032	4871.028
4778.026	4781.163	4829.035	4841.968	4845.173	4849.040	4871.036

Table A.2: Mean Julian date of the first third of the observations of HD 189631.

4650.055 (HARPS)	4650.680 (HERCULES)	4651.373 (HARPS)	4652.348 (HARPS)
4650.064 (HARPS)	4650.705 (HERCULES)	4651.380 (HARPS)	4652.355 (HARPS)
4650.073 (HARPS)	4651.047 (HARPS)	4651.387 (HARPS)	4652.363 (HARPS)
4650.082 (HARPS)	4651.054 (HARPS)	4651.394 (HARPS)	4652.370 (HARPS)
4650.090 (HARPS)	4651.061 (HARPS)	4651.402 (HARPS)	4652.377 (HARPS)
4650.126 (HARPS)	4651.069 (HARPS)	4651.409 (HARPS)	4652.385 (HARPS)
4650.135 (HARPS)	4651.076 (HARPS)	4651.416 (HARPS)	4652.392 (HARPS)
4650.143 (HARPS)	4651.101 (HARPS)	4651.424 (HARPS)	4652.399 (HARPS)
4650.152 (HARPS)	4651.107 (HARPS)	4651.431 (HARPS)	4652.407 (HARPS)
4650.161 (HARPS)	4651.113 (HARPS)	4652.041 (HARPS)	4652.414 (HARPS)
4650.205 (HARPS)	4651.119 (HARPS)	4652.048 (HARPS)	4652.421 (HARPS)
4650.216 (HARPS)	4651.145 (HARPS)	4652.055 (HARPS)	4652.429 (HARPS)
4650.225 (HARPS)	4651.151 (HARPS)	4652.063 (HARPS)	4652.436 (HARPS)
4650.233 (HARPS)	4651.156 (HARPS)	4652.070 (HARPS)	4653.038 (HARPS)
4650.242 (HARPS)	4651.162 (HARPS)	4652.097 (HARPS)	4653.045 (HARPS)
4650.279 (HARPS)	4651.192 (HARPS)	4652.104 (HARPS)	4653.052 (HARPS)
4650.286 (HARPS)	4651.196 (HARPS)	4652.112 (HARPS)	4653.060 (HARPS)
4650.293 (HARPS)	4651.201 (HARPS)	4652.119 (HARPS)	4653.067 (HARPS)
4650.301 (HARPS)	4651.205 (HARPS)	4652.126 (HARPS)	4653.093 (HARPS)
4650.308 (HARPS)	4651.210 (HARPS)	4652.163 (HARPS)	4653.100 (HARPS)
4650.340 (HARPS)	4651.214 (HARPS)	4652.171 (HARPS)	4653.108 (HARPS)
4650.348 (HARPS)	4651.240 (HARPS)	4652.178 (HARPS)	4653.115 (HARPS)
4650.355 (HARPS)	4651.246 (HARPS)	4652.185 (HARPS)	4653.122 (HARPS)
4650.362 (HARPS)	4651.252 (HARPS)	4652.193 (HARPS)	4653.158 (HARPS)
4650.369 (HARPS)	4651.258 (HARPS)	4652.232 (HARPS)	4653.165 (HARPS)
4650.377 (HARPS)	4651.264 (HARPS)	4652.239 (HARPS)	4653.172 (HARPS)
4650.384 (HARPS)	4651.297 (HARPS)	4652.247 (HARPS)	4653.179 (HARPS)
4650.391 (HARPS)	4651.303 (HARPS)	4652.254 (HARPS)	4653.187 (HARPS)
4650.399 (HARPS)	4651.309 (HARPS)	4652.261 (HARPS)	4653.221 (HARPS)
4650.406 (HARPS)	4651.315 (HARPS)	4652.281 (HARPS)	4653.228 (HARPS)
4650.413 (HARPS)	4651.321 (HARPS)	4652.288 (HARPS)	4653.235 (HARPS)
4650.421 (HARPS)	4651.336 (HARPS)	4652.296 (HARPS)	4653.243 (HARPS)
4650.428 (HARPS)	4651.343 (HARPS)	4652.303 (HARPS)	4653.250 (HARPS)
4650.435 (HARPS)	4651.351 (HARPS)	4652.326 (HARPS)	4653.274 (HARPS)
4650.568 (HERCULES)	4651.358 (HARPS)	4652.333 (HARPS)	4653.282 (HARPS)
4650.654 (HERCULES)	4651.365 (HARPS)	4652.341 (HARPS)	4653.289 (HARPS)

Table A.3: Mean Julian date of the second third of the observations of HD 189631.

4653.296 (HARPS)	4654.184 (HARPS)	4655.102 (HARPS)	4655.433 (HARPS)
4653.304 (HARPS)	4654.190 (HARPS)	4655.110 (HARPS)	4655.449 (HERCULES)
4653.322 (HARPS)	4654.216 (HARPS)	4655.117 (HARPS)	4655.530 (HERCULES)
4653.329 (HARPS)	4654.222 (HARPS)	4655.124 (HARPS)	4655.618 (HERCULES)
4653.337 (HARPS)	4654.228 (HARPS)	4655.162 (HARPS)	4655.671 (HERCULES)
4653.344 (HARPS)	4654.234 (HARPS)	4655.168 (HARPS)	4655.721 (HERCULES)
4653.351 (HARPS)	4654.262 (HARPS)	4655.174 (HARPS)	4656.041 (HARPS)
4653.359 (HERCULES)	4654.268 (HARPS)	4655.180 (HARPS)	4656.047 (HARPS)
4653.359 (HARPS)	4654.274 (HARPS)	4655.186 (HARPS)	4656.053 (HARPS)
4653.366 (HARPS)	4654.280 (HARPS)	4655.217 (HARPS)	4656.059 (HARPS)
4653.373 (HARPS)	4654.327 (HARPS)	4655.223 (HARPS)	4656.065 (HARPS)
4653.381 (HARPS)	4654.335 (HARPS)	4655.229 (HARPS)	4656.097 (HARPS)
4653.388 (HARPS)	4654.342 (HARPS)	4655.235 (HARPS)	4656.103 (HARPS)
4653.395 (HARPS)	4654.349 (HARPS)	4655.265 (HARPS)	4656.109 (HARPS)
4653.403 (HARPS)	4654.357 (HARPS)	4655.271 (HARPS)	4656.115 (HARPS)
4653.410 (HARPS)	4654.364 (HARPS)	4655.276 (HARPS)	4656.168 (HARPS)
4653.417 (HARPS)	4654.371 (HARPS)	4655.281 (HARPS)	4656.173 (HARPS)
4653.424 (HARPS)	4654.390 (HARPS)	4655.320 (HARPS)	4656.179 (HARPS)
4653.432 (HARPS)	4654.397 (HARPS)	4655.326 (HARPS)	4656.185 (HARPS)
4653.443 (HERCULES)	4654.404 (HARPS)	4655.332 (HARPS)	4656.223 (HARPS)
4653.548 (HERCULES)	4654.412 (HARPS)	4655.338 (HARPS)	4656.229 (HARPS)
4653.633 (HERCULES)	4654.416 (HERCULES)	4655.344 (HARPS)	4656.234 (HARPS)
4653.689 (HERCULES)	4654.419 (HARPS)	4655.350 (HARPS)	4656.240 (HARPS)
4653.742 (HERCULES)	4654.426 (HARPS)	4655.356 (HARPS)	4656.316 (HARPS)
4654.036 (HARPS)	4654.433 (HARPS)	4655.361 (HERCULES)	4656.322 (HARPS)
4654.043 (HARPS)	4654.495 (HERCULES)	4655.362 (HARPS)	4656.327 (HARPS)
4654.050 (HARPS)	4654.520 (HERCULES)	4655.368 (HARPS)	4656.332 (HARPS)
4654.058 (HARPS)	4654.549 (HERCULES)	4655.374 (HARPS)	4656.338 (HARPS)
4654.065 (HARPS)	4654.583 (HERCULES)	4655.380 (HARPS)	4656.339 (HERCULES)
4654.108 (HARPS)	4654.608 (HERCULES)	4655.386 (HARPS)	4656.343 (HARPS)
4654.116 (HARPS)	4654.633 (HERCULES)	4655.391 (HARPS)	4656.348 (HARPS)
4654.123 (HARPS)	4655.039 (HARPS)	4655.398 (HARPS)	4656.353 (HARPS)
4654.130 (HARPS)	4655.046 (HARPS)	4655.404 (HARPS)	4656.359 (HARPS)
4654.166 (HARPS)	4655.053 (HARPS)	4655.411 (HARPS)	4656.364 (HARPS)
4654.172 (HARPS)	4655.061 (HARPS)	4655.419 (HARPS)	4656.369 (HARPS)
4654.178 (HARPS)	4655.068 (HARPS)	4655.426 (HARPS)	4656.374 (HARPS)

Table A.4: Mean Julian date of the third third of the observations of HD 189631.

4656.379 (HARPS)	4660.222 (FEROS)	4666.318 (FEROS)	5011.912 (HARPS)
4656.385 (HARPS)	4660.228 (FEROS)	4666.325 (FEROS)	5011.926 (HARPS)
4656.390 (HARPS)	4660.234 (FEROS)	4666.340 (FEROS)	5011.940 (HARPS)
4656.396 (HARPS)	4660.240 (FEROS)	4666.346 (FEROS)	5011.956 (HARPS)
4656.404 (HARPS)	4660.246 (FEROS)	4667.062 (FEROS)	5012.927 (HARPS)
4656.411 (HARPS)	4660.262 (FEROS)	4667.077 (FEROS)	5012.941 (HARPS)
4656.418 (HARPS)	4660.267 (FEROS)	4667.084 (FEROS)	5012.955 (HARPS)
4656.426 (HARPS)	4660.273 (FEROS)	4667.107 (FEROS)	5028.906 (HARPS)
4656.433 (HARPS)	4660.279 (FEROS)	4667.115 (FEROS)	5028.921 (HARPS)
4656.445 (HERCULES)	4660.285 (FEROS)	4667.123 (FEROS)	5028.935 (HARPS)
4656.527 (HERCULES)	4660.291 (FEROS)	4667.130 (FEROS)	5028.949 (HARPS)
4656.617 (HERCULES)	4660.308 (FEROS)	4684.580 (HERCULES)	5029.771 (HARPS)
4656.667 (HERCULES)	4660.314 (FEROS)	4684.595 (HERCULES)	5029.786 (HARPS)
4656.720 (HERCULES)	4660.319 (FEROS)	4684.617 (HERCULES)	5029.800 (HARPS)
4657.403 (HERCULES)	4661.367 (HERCULES)	4684.639 (HERCULES)	5029.809 (HARPS)
4659.372 (HERCULES)	4661.447 (HERCULES)	4686.577 (HERCULES)	5030.761 (HARPS)
4659.453 (HERCULES)	4661.522 (HERCULES)	4687.579 (HERCULES)	5030.778 (HARPS)
4659.529 (HERCULES)	4666.015 (FEROS)	4688.566 (HERCULES)	5030.794 (HARPS)
4659.629 (HERCULES)	4666.021 (FEROS)	5003.914 (HARPS)	5030.809 (HARPS)
4659.673 (HERCULES)	4666.028 (FEROS)	5003.928 (HARPS)	5030.827 (HARPS)
4660.000 (FEROS)	4666.034 (FEROS)	5003.944 (HARPS)	5030.844 (HARPS)
4660.058 (FEROS)	4666.040 (FEROS)	5005.943 (HARPS)	5030.861 (HARPS)
4660.066 (FEROS)	4666.047 (FEROS)	5005.958 (HARPS)	5030.878 (HARPS)
4660.073 (FEROS)	4666.062 (FEROS)	5006.939 (HARPS)	5030.941 (HARPS)
4660.092 (FEROS)	4666.202 (FEROS)	5006.953 (HARPS)	5031.581 (HARPS)
4660.100 (FEROS)	4666.209 (FEROS)	5008.914 (HARPS)	5031.849 (HARPS)
4660.108 (FEROS)	4666.215 (FEROS)	5008.927 (HARPS)	5031.864 (HARPS)
4660.115 (FEROS)	4666.221 (FEROS)	5008.942 (HARPS)	5031.879 (HARPS)
4660.123 (FEROS)	4666.228 (FEROS)	5008.956 (HARPS)	5031.894 (HARPS)
4660.130 (FEROS)	4666.234 (FEROS)	5009.915 (HARPS)	5031.909 (HARPS)
4660.187 (FEROS)	4666.293 (FEROS)	5009.930 (HARPS)	5031.923 (HARPS)
4660.194 (FEROS)	4666.299 (FEROS)	5009.943 (HARPS)	5031.936 (HARPS)
4660.200 (FEROS)	4666.305 (FEROS)	5009.958 (HARPS)	
4660.216 (FEROS)	4666.312 (FEROS)	5010.903 (HARPS)	

Table A.5: Mean Julian date of observations of AC Lep.

4440.940	4543.855	4777.961	4781.127	4818.059	4841.131	4845.049	4849.059
4441.063	4543.871	4777.971	4781.136	4818.067	4841.139	4845.079	4849.088
4441.909	4543.880	4777.998	4781.145	4818.091	4841.915	4845.087	4849.096
4441.995	4543.892	4778.007	4813.912	4818.100	4841.923	4845.117	4849.125
4442.035	4543.902	4778.034	4813.921	4818.109	4841.948	4845.125	4849.133
4442.062	4543.909	4778.044	4813.930	4821.905	4841.957	4845.155	4867.887
4442.087	4543.920	4778.074	4813.939	4821.914	4841.985	4845.163	4867.895
4442.116	4543.933	4778.082	4813.947	4821.946	4841.993	4845.895	4867.931
4442.130	4543.943	4778.112	4813.955	4821.954	4842.021	4845.926	4867.939
4442.908	4545.889	4778.120	4813.965	4821.985	4842.029	4845.932	4867.948
4443.008	4548.822	4778.148	4813.974	4821.993	4842.059	4845.948	4867.957
4443.059	4548.828	4778.156	4813.982	4822.023	4842.066	4845.975	4867.965
4443.088	4548.833	4778.184	4813.990	4822.031	4842.102	4845.984	4867.973
4443.114	4548.838	4780.084	4813.998	4822.061	4842.979	4846.032	4870.896
4443.128	4548.843	4780.092	4814.007	4822.070	4842.988	4846.070	4870.904
4462.956	4548.848	4780.118	4814.015	4822.100	4842.998	4846.078	4870.913
4522.951	4548.853	4780.127	4814.025	4822.112	4843.015	4846.885	4870.947
4539.881	4548.860	4780.154	4814.033	4822.144	4843.023	4846.894	4870.955
4539.900	4548.865	4780.162	4814.044	4822.152	4843.031	4846.923	4870.964
4539.916	4548.870	4780.919	4814.053	4838.961	4843.039	4846.928	4870.976
4540.861	4548.875	4780.927	4814.061	4838.970	4843.060	4847.016	4871.011
4541.867	4548.881	4780.937	4814.069	4838.995	4843.069	4847.025	4871.020
4541.907	4548.886	4780.945	4814.078	4839.004	4843.090	4847.056	4872.909
4541.951	4548.891	4780.959	4814.086	4839.012	4843.099	4848.884	4872.919
4542.864	4548.896	4780.967	4817.913	4839.048	4843.109	4848.893	
4542.890	4548.904	4780.994	4817.921	4840.966	4844.920	4848.922	
4542.916	4548.909	4781.005	4817.951	4840.976	4844.929	4848.945	
4542.923	4548.917	4781.033	4817.960	4840.985	4844.960	4848.974	
4542.949	4548.926	4781.047	4817.986	4840.994	4844.968	4848.982	
4543.968	4548.934	4781.080	4817.994	4841.085	4844.998	4849.013	
4543.841	4548.945	4781.089	4818.023	4841.095	4845.007	4849.021	
4543.849	4548.954	4781.097	4818.031	4841.105	4845.041	4849.051	

Appendix B

Flat fields for HERCULES

This appendix describes the procedure used in this thesis to compile flat field images for the 600 Series Spectral Instruments CCD camera installed on HERCULES.

Why new flat fields are regularly needed? Flat fields are needed in the reduction process of all images to remove artifacts in the data caused by variations in the pixel-to-pixel sensitivity of the CCD camera. Flat fields are also used to detect the position of the orders on the camera. Each time the optical instruments are moved, or after a period of time long enough for the pixel-to-pixel sensitivity to be altered by the aging of the CCD, new flat fields are needed. On November 11^{th} 2008, HERCULES was opened to install a scrambler on the optic fibers. As we want to constantly upgrade our optical instruments in order for HERCULES to remain an extremely competitive facility in world-wide scientific research, new flat fields need to be produced regularly.

How to collect them? Since the "white lamp" used emits strongly in the red compared to the blue, in order to have enough signal in the blue a long exposure is needed. However any exposures longer than 1 second has a high risk of over-exposing the CCD in the red orders (2 seconds seems to be almost exactly at the limit). This is why many white spectra are taken and later combined to obtain one single flat field with good signal in the blue (and thus excellent signal in the red). One hundred images was thought to be enough.

How to combine them? A median filter must be performed on the images in order to remove all cosmic rays from them. A median filter takes, for each pixel in the final

image, the median value of all corresponding pixels in the 100 images. For example, if a pixel value is denoted $X_{i,j,s}$, where i is the number of lines (from 1 to 3924), j the number of columns (from 1 to 4036) and s the image number (from 1 to 100 in our example), then the $X_{i,j}$ in the final flat field image is equal to the median of all $X_{i,j,s}$ with s from 1 to 100 (i, j are fixed).

However, the command "medsky" in Figaro is giving unexpected data points larger or smaller by many orders of magnitude than what was expected. The Bzero and Bscale parameters, stored in the headers, are scaled accordingly and therefore the true data could theoretically be restored. Unfortunately HRSP could not deal with this. It was therefore necessary to write a Matlab program which performs a median filter on the data.

All images were prepared with HRSP, producing "r" files where the data is in 32-bit format and not integer. This makes it easier for mathematical operations, but all files are now double in size. A hundred files with 64 MB makes 6.4 GB and not enough RAM is available for such an operation. This is why the files were grouped by ten, simply adding the data together and producing one array for every 10 files. Then with these 10 arrays (which could be output as .fit files) a "scaled" median filter was performed. Scaling means that all 10 images have been scaled with respect to the first one so that they all have the average same brightness (or photon count). This is done by calculating the average from all data points in a single image, evaluating the difference with the first image, and scale all data points in a given image by a multiplicative factor:

$$X'_{i,j,s} = \frac{X_{i,j,s} * Average_1}{Average_s} \tag{B.1}$$

where

$$Average_s = \frac{\sum_{i=1}^{3924} \sum_{j=1}^{4036} X_{i,j,s}}{3924 * 4036} \tag{B.2}$$

The Size problem with Matlab output of .fit files. A problem was encountered when outputting the data in .fit files. The size of a .fit file must always be an integer number of "records", where one record is equal to 2880 bytes. The headers for a file can be written so that there will always be an integer number of records, no matter how many characters there are in the headers. The program to output .fit files with

Matlab is making sure that this is the case. But the data size is not an integer number of records:

$$\frac{3924 \cdot 4036 \cdot 4}{2880} = 21996.2 \tag{B.3}$$

HRSP produces these r-files which have the exact same numbers of rows and columns, but in that case the size of the file is 22002 records, with headers being equal to 5 records, so the data turns out to be 21997 records. The way I got around that problem was to use the "cat" commend in Linux to append a file to my final flat field. This file, called *extrasize.bin* is exactly 0.8 records (or 2304 bytes). The command used is:

$$catinput.fitextrasize.bin > output.fit \tag{B.4}$$

Back to HRSP! Now this final output file can be used with the command "reduce white" in HRSP, and it correctly produces "flat.fit" and "order.fit". We can finally reduce all our images, until the next upgrade of HERCULES. Et voila!